

Tunable Micro-Cavities In Photonic Band-Gap Yarns And Optical Fibers

by

Gilles Benoit

M.S. Materials Science
Ecole Nationale Supérieure des Mines de Nancy, FR, 2001

Submitted to the Department of Materials Science and Engineering
in Partial Fulfillment of the Requirements for the Degree of

Doctor of Philosophy in Materials Science and Engineering
at the
Massachusetts Institute of Technology

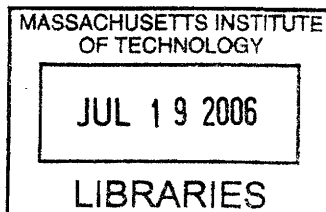
June 2006

©2006 Massachusetts Institute of Technology
All rights reserved

Signature of Author: _____
Department of Materials Science and Engineering
May 18, 2006

Certified by: _____
Yoel Fink
Thomas B. King Associate Professor of Materials Science
Thesis Supervisor

Accepted by: _____
Samuel M. Allen
POSCO Professor of Physical Metallurgy
Chair, Departmental Committee on Graduate Students



ARCHIVES

Tunable Micro-Cavities In Photonic Band-Gap Yarns And Optical Fibers

by
Gilles Benoit

Submitted to the Department of Materials Science and Engineering
on May 18, 2006 in Partial Fulfillment of the Requirements for the Degree of
Doctor of Philosophy in Materials Science and Engineering

ABSTRACT: The vision behind this work is the fabrication of high performance innovative fiber-based optical components over kilometer length-scales. The optical properties of these fibers derive from their multilayer dielectric photonic band-gap structure that exhibits omnidirectional reflectivity. The theoretical tools needed to design, analyze and optimize such structures are introduced. We show that defect layers in these otherwise periodic structures act as optical micro-cavities that enable precise design of the fibers' spectral response. Fabrication of these composite fibers by thermal drawing of a macroscopic preform in the viscous state requires solving material selection challenges in order to identify pairs of materials with high refractive index contrast and similar thermo-mechanical properties. Operational wavelengths ranging from the UV to the IR are demonstrated and made possible by the wavelength scalability of the photonic band-gap structure and accurate knowledge of the materials' dispersion relation afforded by broadband spectroscopic ellipsometry. The fundamentals of this technique, which is used to characterize a number of dielectrics, semi-conductors and metals, are surveyed.

Two fiber structures are then explored: fibers for external reflection and hollow-core transmission fibers. We demonstrate that the resonance wavelength of Fabry-Perot cavities embedded in reflecting fibers can be tuned reversibly under applied elastic strain or external illumination at 514 nm. A simple opto-mechanical model is developed to assess the mechanical tuning efficiency while a review of the photodarkening effect in chalcogenide glasses and accurate measurements of the amplitude and response time associated with its transient component are presented to explain and optimize the optical tuning scheme. Modulation of the fibers' reflectivity near their cavity resonant wavelengths is demonstrated at various frequencies. Based on these results, we show that optical micro-cavities in transmission fibers can induce very high group-velocity dispersion as a result of the interaction between the propagating core modes and the lossy cavity resonant mode(s). Widely tunable dispersion is achieved using a mechanical tuning scheme. Applications for these fibers and future research directions are envisioned.

Thesis Supervisor: Yoel Fink
Title: Thomas B. King Associate Professor of Materials Science

BIOGRAPHY

I was born in St Germain-En-Laye near Paris, FR on September 12, 1978. In 1993, I attended college at the Ecole Saint Martin de France in Pontoise, FR where I received the Diplôme du Baccalauréat Général with honors in 1996. I then enrolled a program at the Lycée Janson de Sailly in Paris, FR to prepare for the written and oral examinations required for admission in France's most prestigious engineering schools. Simultaneously, I joined the Université de Cergy-Pontoise, U.F.R. Sciences et Techniques where I received the Diplôme d'Etudes Universitaires Générales in the field of Mathematics, Computer Science and their Applications to Science with honors in 1998. The same year, I was admitted at the Ecole Nationale Supérieure des Mines de Nancy, FR where I studied Materials Science and Numerical Simulation for two years. In 2000, I also registered at the Université Henri Poincaré, Nancy 1 for a simultaneous Master of Science in Materials Science and Engineering. As part of the program, I characterized Samarium-Neodymium super-lattices by neutron scattering at the Institut Laue Langevin in Grenoble, FR (IN3) under the supervision of Prof. Philippe Mangin and Erbium-Dysprosium super-lattices by magnetic X-ray diffraction at the Argonne National Laboratory, IL (SDS4) under the supervision of Prof. Sunhil Sinha and Dr. George Srajer. In 2001, I received the Diplôme d'Ingénieur Civil des Mines de l'Ecole Nationale Supérieure des Mines de Nancy and a Master of Science called Diplôme d'Etudes Approfondies de l'Institut National Polytechnique de Lorraine in Physics and Chemistry of Matter and Materials. My Master thesis is entitled "Comparative Study Of Coupling Effects In Sm/Nd And Er/Dy Magnetic Super-lattices Characterized By Neutron Scattering And Magnetic X-ray Diffraction".

In the fall of 2001, I joined the Department of Materials Science and Engineering at the Massachusetts Institute of Technology. I worked as a research assistant for Prof. Yet-Ming Chiang for six months on Magnetic Memory-Shape Alloys and joined Prof. Yoel Fink's group in January 2002. The group later that year took the name of Photonic Bandgap Fibers and Devices Group. I published my first article, which made the cover of Advanced Materials, in December 2003. Beyond the four departmental core classes, I took Prof. John D. Joannopoulos' class on Solid State Physics, Prof. Jeff Shapiro's class on Quantum Optical Communication, Prof. Vladimir Bulovic's class on Organic Optoelectronics and finally Prof. Marko Huhtanen's class on Numerical Simulation. In 2005, I was a teaching assistant for Prof. Yoel Fink's graduate class on Electrical, Optical and Magnetic properties of Materials. Shortly before defending my doctoral thesis entitled "Tunable Micro-Cavities In Photonic Band-Gap Yarns And Optical Fibers", I accepted a position of Senior Product Engineer at 3M in their Display and Graphic Business Laboratory.

ACKNOWLEDGEMENTS

I would like first to thank all the people who have helped me during my research at MIT. I have to start with my advisor Prof. Yoel Fink who has been so inspirational to me. By collaborating with him, I have acquired diverse technical skills, developed a deep understanding of the fundamental scientific concepts underlying our discipline and have had the opportunity to contribute to challenging and rewarding projects. As importantly, his charisma, integrity and perseverance have been contagious throughout this journey and helped me grow on a personal level. I would also like to thank Prof. John Joannopoulos and Prof. Francesco Stellacci, my committee members, for their constant support and excitement for my research and Prof. Robert Ogilvie for his encouragements and for reminding the department of the high educational level of French students.

I must of course thank my research group and more particularly: Dr. Burak Temelkuran and Dr. Shandon D. Hart who have been exceptional tutors by involving me in their research and providing valuable guidance for my initial projects; Dr. Ken Kuriki, Jean-Francois Viens and Dursen Hinczewski for their help in drawing the many fiber structures studied in this thesis and for making it a fun experience; Dr. Ayman Abouraddy, Dr. Laurent Vaissie and Ofer Shapira who have been incredibly helpful by dedicating time and effort to help me solve some of the complex technical and theoretical challenges encountered in this work. I also thank all the other group members for their kindness and support: Dr. Mehemet Bayindir, Fabien Sorin, Nicholas Orf, Daosheng Deng, Yuka Kuriki, Chris Saranto, Megan Brewster, Dr. Karlene Maskaly, Jeremy Arnold, Dr. Shunji Egusa, Dr. Sylvain Danto, Dana Shemuli, Zachary Ruff and our wonderful administrative assistants, Cathy Bruce and Jenna Picceri.

During my stay at MIT, I have also collaborated with other researchers outside the group who I owe special thanks: Dr. Mihai Ibanescu and Dr. Steven Johnson for contributing indirectly to this research; Dr. Richard Sun who has taught me all the tricks of ellipsometry; Prof. J. Phillips and his group from The University of Michigan, Dr. Tamar Tepper, Dr. Tymon Barwicz, Natalija Jovanovic and many others for the opportunity to collaborate with them on ellipsometry measurements and learn from their research; and finally Tim McLure for training me on FTIR measurements. I would also like to acknowledge the support of DARPA, the ARO, the ONR and the AFOSR who provided much of my funding, as well as the support of the NSF/MRSEC program through the CMSE shared facilities.

Beyond the research, these five years have been a very fruitful and happy time in my life thanks to the wonderful friends I have made in Boston and the support of my friends back in France. These include Murray Wheeler, John Morgan, Gregory Blaze, Ajit Dash and the MIT LGBT community, Heather Conrad and all the wonderful people I met at Dechert LLP, Celine Thiaville, Yann Gunzburger, Flora Garcia, Benjamin Bruet, Isabelle Letard, Jerome Faure-Vincent, and many more. Finally, I thank my family, in particular my parents and grandparents, for their love and encouragements, and Drew Picciafoco for being such a wonderful and understanding partner.

I dedicate this thesis to all these people who have made it possible. Thank you all!

TABLE OF CONTENTS

I	INTRODUCTION	7
II	BACKGROUND	10
II.1	ONE-DIMENSIONAL PHOTONIC BAND-GAP STRUCTURES	10
II.1.1	OPTIMAL STRUCTURE FOR A BRAGG REFLECTOR	12
II.1.2	THE TRANSFER MATRIX METHOD (TMM)	13
II.1.3	PHOTONIC BAND DIAGRAMS	16
II.2	FABRY-PEROT MICRO-CAVITIES	18
II.2.1	DEFECT STATES IN THE PHOTONIC BAND DIAGRAM	19
II.2.2	THE QUALITY FACTOR OF AN OPTICAL RESONATOR	21
II.2.3	INFLUENCE OF THE CAVITY OPTICAL THICKNESS	22
II.2.4	THE DENSITY OF MODES	23
III	MEASUREMENTS OF OPTICAL CONSTANTS	25
III.1	WHAT IS AN INDEX OF REFRACTION?	25
III.2	PRINCIPLES OF ELLIPSOMETRY	27
III.2.1	DEFINITION OF THE ELLIPSOMETRIC PARAMETERS	27
III.2.2	THE RPE AND RAE CONFIGURATIONS	29
III.3	EQUIPMENT AND MEASUREMENT PARAMETERS	32
III.3.1	BULK SAMPLES	33
III.3.2	THIN FILM SAMPLES	34
III.4	MEASUREMENT ANALYSIS	36
III.4.1	DIELECTRICS	37
III.4.2	SEMICONDUCTORS	40
III.4.3	CONDUCTORS	42
III.4.4	INHOMOGENEOUS LAYERS AND ROUGH INTERFACES	43
III.4.5	FITTING	45
III.4.6	POINT TO POINT N & K CALCULATION	46
III.5	SAMPLE PREPARATION	46
IV	FABRICATION OF PHOTONIC BAND-GAP FIBERS	48
IV.1	PREFORM FABRICATION	50
IV.2	DRAWING TECHNIQUE	52
IV.3	SCANNING ELECTRON MICROSCOPY OF FIBER CROSS-SECTIONS	55

V	REFLECTION FABRY-PEROT FIBERS	57
V.1	REFLECTIVITY MEASUREMENTS	58
V.2	MECHANICAL TUNING	60
V.2.1	OPTO-MECHANICAL BEHAVIOR OF FABRY-PEROT FIBERS	61
V.2.2	MECHANICAL TUNING EXPERIMENT	66
V.2.3	RESULTS AND INTERPRETATION	67
V.2.4	DYNAMIC MECHANICAL TUNING	69
V.3	OPTICAL TUNING	71
V.3.1	INTRODUCTION TO CHALCOGENIDE GLASSES AND THE PHOTODARKENING EFFECT	72
V.3.2	THREE LEADING MODELS TO DESCRIBE THE PHOTODARKENING EFFECT	75
V.3.3	KINETICS OF THE PHOTODARKENING EFFECT	81
V.3.4	PHOTO-INDUCED REFRACTIVE INDEX CHANGE IN As_2Se_3 AND As_2S_3 THIN FILMS	82
V.3.5	STATIC AND DYNAMIC OPTICAL TUNING	87
VI	HOLLOW CORE PHOTONIC BAND-GAP TRANSMISSION FIBERS	94
VI.1	GUIDED MODES IN HOLLOW CORE TRANSMISSION PHOTONIC BAND-GAP FIBERS	97
VI.1.1	SOLUTIONS TO THE WAVE EQUATION IN CYLINDRICAL COORDINATES	97
VI.1.2	IDENTIFYING THE GUIDED MODES: THE LEAKY-MODE TECHNIQUE	99
VI.1.3	MODAL CHARACTERISTICS	100
VI.2	TRANSMISSION MEASUREMENTS	104
VI.2.1	SPECTRAL CHARACTERIZATION	104
VI.2.2	MODAL CHARACTERIZATION	105
VI.2.3	PROPAGATION LOSSES CHARACTERIZATION	107
VI.3	MECHANICAL TUNING OF TRANSMISSION PHOTONIC BAND-GAP FIBERS	110
VI.4	DESIGN OF HIGHLY DISPERSIVE TRANSMISSION FIBERS	112
VI.4.1	GROUP-VELOCITY DISPERSION IN PERFECTLY PERIODIC PHOTONIC BAND-GAP FIBERS	113
VI.4.2	GROUP-VELOCITY DISPERSION IN TRANSMISSION FIBERS CONTAINING MICRO-CAVITIES	114
VI.5	DISPERSION MEASUREMENTS	117
VI.6	MECHANICAL TUNING OF HIGHLY DISPERSIVE HOLLOW CORE FIBERS	130
VI.7	FUTURE DIRECTIONS	131
VII	CONCLUSION	132

I Introduction

Fibers are everywhere. Our clothes are made of synthetic polymer or natural fibers. The most massive of suspension bridges are held by bundles of steel fibers. Conductive copper wires are used to transmit data and power via electrons, while silica-glass fibers deliver voice and data across the globe by guiding light (and may truly be considered the “fabric” that holds together our information society). The fibers in each of these cases are usually comprised of a single material (or two very similar materials in the case of the core-cladding structure of optical fibers) and perform a single function, i.e. clothing, mechanical support, information transfer, etc. We seek to overturn this paradigm by producing ‘hybrid’ fibers that consist of more than one material to enable novel functionalities. These fibers may then be used to construct fabrics that deliver these functionalities on large areas with low cost.

The fabrication and characterization of silica optical fibers has been developed into a precise art under the impetus of the remarkable success of the telecommunications industry. An unintentional side effect of this success has been the focusing of efforts on a small set of materials and structures that provide light guidance in the fiber core through total internal reflection. This situation has changed radically in the last decade. Novel micro-structured fibers have been explored that allow for more freedom in designing the performance of the fibers, although light guidance still relied on total internal reflection. Fibers that contain two-dimensional photonic crystal structures and guide light by a photonic band-gap effect have also been fabricated. The wide range of results obtained with these fibers has been recently reviewed.^{1,2} Nevertheless, the materials used in these novel fibers are the traditional fiber materials (namely silica glasses or polymers) with the addition of air holes.

Our group has pioneered several new material systems and geometries adding them to the repertoire of optical fibers, and the rich interplay between these aspects has led to a number of unique and unconventional fibers. This goal necessitates innovative

fabrication approaches that allows for the use of new materials and geometries that have not been, hitherto, associated with fibers. By combining materials and exploring novel geometries, conventional functionalities can be enhanced and new ones introduced. This vision presents a unique set of challenges. Whatever the processing method, materials with potentially quite different electronic or optical properties must be compatible in such a way that enables the production of kilometers of composite fibers with submicron feature sizes, an aspect ratio on the order of 10^3 !

The mechanism that we rely on for light guidance is omnidirectional reflection from a one-dimensional photonic crystal structure.³ This structure has the form of a concentric thin-film multilayer structure, where two materials having a high refractive-index contrast alternate with prescribed thicknesses, allowing for light guidance in a hollow core. A distinctive feature of this light-guidance mechanism is that it is *wavelength scalable*, i.e. the final scale of the structure determines the wavelength of light that is transmitted along the fiber. An important consequence is that we may use the same overall fabrication strategy to produce fibers that guide ultra-violet (UV) or mid-infrared (mid-IR) light by simply changing the targeted final dimensions. [Fig.1a] shows an example of the fine control over wavelength scalability where a set of fibers with transmission peaks that extend throughout the visible ‘unweaves’ the rainbow spectrum of white light from a light-emitting diode.

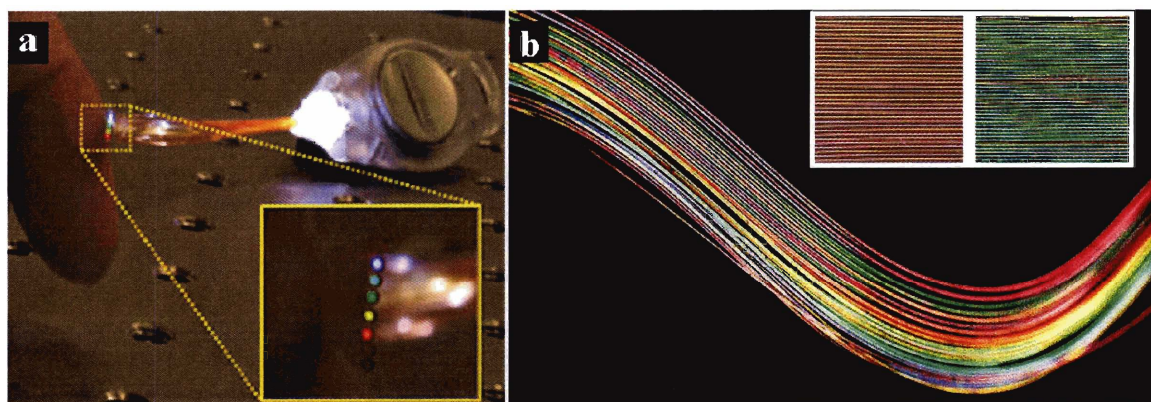


Figure 1: **a** Hollow-core transmission fibers drawn from the same preform to slightly different outer diameters transmit light at different wavelengths in the visible spectrum, **b** reflection fibers with different outer diameters exhibit metallic colors. Such fibers could be used to create large-scale flexible mats for radiation protection as shown in the insert.

A striking application is the placement of the omnidirectional reflector on the external surface of the fiber. Light that impinges on the fiber outer surface is reflected away if it lies within the forbidden band-gaps, which are wavelength scalable as in the case of transmission fibers [Fig.1b]. Our first demonstration of this particular fiber structure, in fact, yielded reflection that surpassed that of gold. Furthermore, so-called ‘defect’ cavities may be placed within the reflecting structure to allow a resonant wavelength within the photonic band-gap to tunnel through the structure instead of being reflected. Such fibers lend themselves to highly efficient mechanical and optical tuning of their optical response, creating opportunities for a new generation of active integrated optical components.

We shall first review in section II the theory behind one-dimensional photonic crystal structures and the conditions necessary to achieve omnidirectional reflectivity. We will also show that defect layers in these otherwise periodic structures act as optical micro-cavities that enable efficient light confinement and precise design of their spectral response. It will be apparent that the materials refractive indices are key performance parameters and section III will detail how they can be measured with high accuracy by broadband spectroscopic ellipsometry. In section IV, we will see that our core fabrication strategy is to use the common technique of thermal drawing of a macroscopic fiber preform in the viscous state and that several challenges, such as material selection, are imposed by the nature of this technique. Then, two fiber structures will be explored: external reflection fibers and hollow-core transmission fibers. In section V, we will demonstrate that the resonance wavelength of Fabry-Perot cavities embedded in reflecting fibers can be tuned reversibly under applied elastic strain or external illumination at 514 nm. A simple opto-mechanical model will be developed to assess the mechanical tuning efficiency while a review of the photodarkening effect in chalcogenide glasses and accurate measurements of the amplitude and response time associated with its transient component will be presented to explain and optimize the optical tuning scheme. Modulation of the fibers’ reflectivity near their cavity resonant wavelengths will also be demonstrated at various frequencies. Based on these results, we will show in section VI

that optical micro-cavities in transmission fibers can induce very high group-velocity dispersion as a result of the interaction between the propagating core modes and the lossy cavity resonant mode(s). A mechanical tuning scheme will be implemented to induce widely tunable dispersion. Applications for these fibers and future research directions will be discussed all along.

II Background

II.1 One-dimensional photonic band-gap structures

Photonic crystals can be classified according to their dimensionality. The simplest photonic crystal consists of a one-dimensional stack of planar layers with alternating high and low refractive indices, also called a *Bragg reflector*. Because this multilayer structure possesses two mirror symmetries perpendicular to the plane of the layers, the solutions to Maxwell's equations can be decomposed on the basis of two orthogonal polarizations:⁴ the transverse electric (TE) polarization, for which the electric field is perpendicular to the plane of incidence, and the transverse magnetic (TM) polarization, for which the magnetic field is perpendicular to the plane of incidence [Fig.2a].

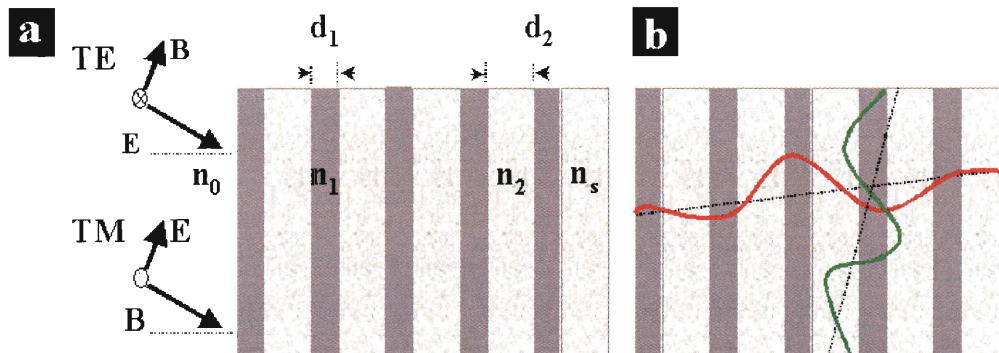


Figure 2: **a** Schematic of the structure and orientation of the electric and magnetic fields for the TE and TM polarizations, **b** light with wavelength $\lambda_1=2(n_1d_1+n_2d_2)$ is diffracted when propagating near normal incidence (red), while it is eventually index guided along a high-index layer when propagating near grazing incidence (green).

At normal incidence, the TE and TM polarizations are indistinguishable and therefore degenerate. Such a multilayer structure can be designed to exhibit TE and TM *photonic band-gaps* i.e. energy states that are forbidden to propagate in the photonic crystal in certain directions,⁴ in analogy with electronic band-gaps in semiconductors that result from Bragg diffraction of electrons by the periodic atomic lattice. More precisely, the direction of light is entirely defined by its wave-vector k whose projection onto the plane of the multilayer structure is called the parallel wave-vector, noted β . While the conservation of energy leads to the Huygen's principle and the conservation of the frequency ω , the conservation of momentum in the plane of the homogeneous layers leads to Snell's law and the conservation of β . For small values of β (i.e. close to normal incidence), light is strongly diffracted by the periodic index profile and cannot propagate in the structure if its wavelength satisfies the Bragg diffraction condition:

$$\lambda_m = 2 \frac{n_1 d_1 + n_2 d_2}{m} \quad (\text{at normal incidence}) \quad (1)$$

where n_1, n_2 are the refractive indices and d_1, d_2 the thicknesses of the high index and low-index layers, respectively and m is the diffraction-order integer, also called the *band number* [Fig.2b]. For large values of β (i.e. close to grazing incidence), light is much less affected by the periodicity of the structure and is index-guided in the high refractive index layers. Therefore, a one (two, three)-dimensional photonic crystal imposes a diffraction condition for light in one (two, three) directions of space.

Even though a complete photonic band-gap that would reflect light of frequency ω propagating in any direction of space (i.e. any possible β) and for any polarization cannot be achieved in a one-dimensional photonic crystal, it is possible to observe external *omnidirectional reflectivity* for light incident from the semi-infinite space that does not contain the photonic crystal, typically air, because β is then naturally limited by the group velocity of light in air ($\beta \leq \omega/c$).⁵

II.1.1 Optimal structure for a Bragg reflector

If one was to design an efficient reflector at a specific wavelength λ with a single dielectric layer, a natural choice would be to use a *quarter-wave layer* with high refractive index. Indeed, the high refractive index (n_{layer}) leads to a high reflectance at the air/layer interface:

$$R = \left| \frac{n_{layer} - 1}{n_{layer} + 1} \right|^2 \quad (\text{at normal incidence}) \quad (2)$$

and the quarter-wave condition, which imposes that the optical thickness of the layer $n_{layer}d_{layer}$ be equal to $\lambda/4$, ensures that the light reflected at the air/layer interface interferes constructively with the light reflected after multiple reflections in the layer. This is due to the π (0)-phase shift experienced upon reflection by light traveling from a low (high) index to a high (low) index material.⁶ Taking into account this interference effect, the total reflectance of a quarter-wave layer is given by:

$$R^{Total} = R \frac{4}{\left| 1 + \left(\frac{n_{layer} - 1}{n_{layer} + 1} \right)^2 \right|^2} \geq R \quad (\text{at normal incidence}) \quad (3)$$

By stacking multiple quarter-wave dielectric layers with alternating high and low refractive indices, one creates a succession of highly reflective interfaces that reflect light constructively with one another and can yield much higher total reflectivity around λ than a metallic mirror due to the absence of absorption loss in the dielectric materials. The corresponding ratio of high to low refractive index material d_1/d_2 , also called the *filling fraction*, is given by:^{6,7}

$$\frac{d_1}{d_2} = \frac{n_2}{n_1} \quad (\text{at normal incidence}) \quad (4)$$

$$\frac{d_1}{d_2} = \frac{\sqrt{n_2^2 - 1}}{\sqrt{n_1^2 - 1}} \quad (\text{at grazing incidence}) \quad (5).$$

More fundamentally, the reason why a quarter-wave stack is the optimal Bragg reflector derives from an energy argument. Let's consider the electric field profile

associated with light of wavelength $\lambda_1=2(n_1d_1+n_2d_2)$ incident on the structure at normal incidence. Because such a wave satisfies the Bragg diffraction condition, its electric field profile in the structure must correspond to a standing wave. In addition, it must satisfy the symmetry constraints of the structure, which leaves only two possible solutions: a low energy solution ω_1 where the electric field reaches its extrema in the high-index layers and a high energy solution ω_2 where the electric field reaches its extrema in the low-index layers. The difference in energy between these two solutions is a direct result of the *electro-magnetic variational theorem*, which predicts that low-frequency modes concentrate their energy in high-index regions while high-frequency modes concentrate their energy in low-index regions.⁴ It follows that any state with frequency between ω_1 and ω_2 is forbidden. It also becomes intuitive that the larger the refractive-index contrast between the Bragg layers, the wider the forbidden band. This is the physical origin of the *band-gaps* and the reason for the high reflectivity of these structures.

II.1.2 The Transfer Matrix Method (TMM)

For an in-depth analysis of the optical response of an arbitrary multilayer reflector, we need to solve the four macroscopic Maxwell equations (in cgs units):

$$\nabla \cdot B = 0 \quad (6)$$

$$\nabla \times E + \frac{1}{c} \frac{\partial B}{\partial t} = 0 \quad (7)$$

$$\nabla \cdot D = 4\pi\rho \quad (8)$$

$$\nabla \times H - \frac{1}{c} \frac{\partial D}{\partial t} = \frac{4\pi}{c} J \quad (9)$$

where E and H are the macroscopic electric and magnetic fields, D and B are the displacement and magnetic induction, ρ and J are the free charges and currents. Assuming no external charges and currents and a non-magnetic system, we can derive the master equations for E :

$$\frac{1}{\varepsilon} \nabla \times \nabla \times E = \left(\frac{\omega}{c} \right)^2 E \quad (10)$$

$$\nabla D = 0 \quad (11)$$

Due to the continuous translational symmetry in the plane of the layers (assumed to be homogeneous and isotropic), the solutions to Maxwell equations are of the form:⁴

$$E_{m,\beta}(r,t) = e^{i\omega t} e^{i\beta\rho} u_{m,\beta}(z) \quad (12)$$

where m is the band number, β is the conserved parallel wave-vector and ρ is a vector in the plane of the layers ($r = \rho + z$). At fixed ρ , the one dimensional master equation reduces to:

$$-\frac{d^2}{dz^2} E + \frac{\omega^2}{c^2} (1 - \varepsilon) E = \frac{\omega^2}{c^2} E \quad (13)$$

This equation has the form of a Schroödinger equation with potential $\omega^2(1-\varepsilon)^2/c^2$ and eigenvalue ω^2/c^2 . Therefore in each layer (region of constant “potential”), its solution is simply a linear combination of plane waves propagating in the $+z$ and $-z$ directions:

$$E = (E_{+z} e^{-ik_z z} + E_{-z} e^{ik_z z}) \cdot e^{i(\omega t - \beta\rho)} \quad (14)$$

where k_z is the perpendicular component of the wave-vector ($k^2 = (n\omega/c)^2 = \beta^2 + k_z^2$). There are two unknowns for each layer (the coefficients E_{+z} and E_{-z}) and two boundary conditions at each interface corresponding to the continuity of the tangential component of E and H . By imposing the initial condition that the source lies on one side of the finite multilayer structure (air) and that there is no incoming light from the other side (referred to as the substrate), the system is entirely determined and has a unique exact solution. Note that since the boundary conditions depend on the polarization of light, solutions for the TE and TM polarizations differ. They can be obtained separately if and only if the two polarizations are truly independent, which is the case under the assumption that the layers are homogeneous and isotropic. To do so, it is convenient to use a matrix formalism often referred to as the *Transfer Matrix Method* (TMM)^{8,9}: one can write the TE (TM) solution in each layer as a vector with components E_{+z} and E_{-z} , the TE (TM) boundary conditions at each interface as a 2x2 “transfer” matrix T and the phase shift induced by propagating through each layer as a 2x2 “propagation” matrix P . Then in layer q , we have:⁶

$$\begin{bmatrix} E_{+z}^q \\ E_{-z}^q \end{bmatrix} = [P^q] \cdot [T^{q/q+1}] \cdot [P^{q+1}] \dots [T^{N-1/N}] \cdot [P^N] \cdot [T^{N/Substrate}] \cdot \begin{bmatrix} 1 \\ 0 \end{bmatrix} \quad (15)$$

where N is the total number of layers, E_{+z}^q and E_{-z}^q are the components of the electric field in layer q at the $q-1/q$ interface and the electric field in the substrate is normalized. The coefficients of the P and T matrices are given explicitly in ⁶. Note that if the layers were instead anisotropic, the TE and TM polarizations would be coupled and a general solution would have to be calculated using a 4x4 matrix formalism.

Using this formalism, it is possible to find an exact solution to Maxwell's equations for any arbitrary one dimensional index profile, not just a perfectly periodic Bragg reflector. The reflection coefficient r , reflectance R , transmission coefficient t and transmittance T of the multilayer structure at a certain incident angle θ_0 , frequency ω are then given by:

$$r(\omega) = \left(\frac{E_{-z}^0}{E_{+z}^0} \right)_{E_{-z}^s=0} \quad (16)$$

$$R(\omega) = |r(\omega)|^2 \quad (17)$$

$$t(\omega) = \left(\frac{E_{+z}^s}{E_{+z}^0} \right)_{E_{-z}^s=0} \quad (18)$$

$$T(\omega) = \frac{n_s \cos \theta_s}{n_0 \cos \theta_0} |t(\omega)|^2 \quad (19)$$

where the superscripts 0 and s refer to the air and substrate layers, respectively. Since any incident polarization state can be decomposed on the basis of the TE and TM polarizations, its reflectance and transmittance are simply a weighted average of the ones calculated for the pure TE and TM polarizations.

In the case of a Bragg reflector as described in II.1.1, the reflectance at normal incidence is typically higher than 99.9% for frequencies in the band-gap [Fig.3a].

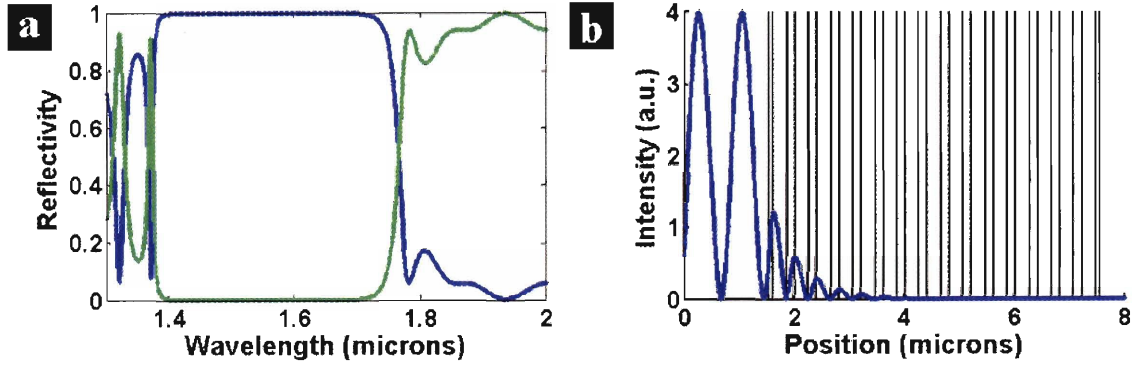


Figure 3: **a** Reflectance (blue) and transmittance (green) for a 15 bilayer Bragg reflector made of poly(ether-imide) (PEI - $n=1.65$ at $\lambda=1.55 \mu\text{m}$) and As_2S_3 ($n=2.4$ at $\lambda=1.55 \mu\text{m}$), **b** intensity profile in the structure at $\lambda=1.55 \mu\text{m}$.

The intensity profile in the multilayer structure at these frequencies exhibits a steep exponential decay [Fig.3b] similar to the decay experienced by an electro-magnetic wave upon reflection on a metallic mirror within the skin depth of the metal.

II.1.3 Photonic band diagrams

To synthesize the performance of a Bragg reflector over all incident angles and all polarizations, it is common to map evanescent and propagating states (corresponding to regions of high and low reflectivity, respectively) in the (ω, β) plane, resulting in what is called a *photonic band diagram*. One elegant way to do so is by assuming an infinite periodic stack. The solutions to Maxwell equations then become Bloch waves due to the discrete translational symmetry perpendicular to the plane of the layers:⁴

$$E_{m,\beta,k_z}(r,t) = e^{i\omega t} e^{i\beta\rho} e^{ik_z z} u_{m,\beta,k_z}(z) \quad (20)$$

where k_z is now the conserved Bloch wave-vector and $u_{m,\beta,k_z}(z+\Lambda) = u_{m,\beta,k_z}(z)$ with $\Lambda = d_1 + d_2$. Writing Bloch's theorem with the matrix formalism, it follows that:⁶

$$\begin{bmatrix} E_{+z}^{q+1} \\ E_{-z}^{q+1} \end{bmatrix} = e^{-ik_z \Lambda} \cdot \begin{bmatrix} E_{+z}^{q-1} \\ E_{-z}^{q-1} \end{bmatrix} = e^{-ik_z \Lambda} \cdot [P^{q-1}] \cdot [T^{q-1/q}] \cdot [P^q] \cdot [T^{q/q+1}] \cdot \begin{bmatrix} E_{+z}^{q+1} \\ E_{-z}^{q+1} \end{bmatrix} \quad (21)$$

This implies that the matrix $[P^{q-1}] \cdot [T^{q-1/q}] \cdot [P^q] \cdot [T^{q/q+1}]$ is a translation operator whose eigenvalues are $e^{\pm ik_z \Lambda}$. This condition leads to the dispersion relation between the two conserved quantities ω and β and the Bloch wave-vector k_z . Regimes where k_z is real

correspond to propagating waves while regimes where k_z is complex correspond to evanescent waves: these are the *photonic band-gaps*. The imaginary component of k_z is equal to zero at the band-edges and reaches a maximum at the center of the band-gaps. The width of the fundamental band-gap $\Delta\omega$ for a quarter-wave stack at normal incidence can be approximated from the dispersion relation as:⁶

$$\Delta\omega = \omega_c \frac{4}{\pi} \frac{|n_1 - n_2|}{n_1 + n_2} \quad (22)$$

where ω_c is the frequency at the center of the photonic band-gap. It depends therefore linearly on the refractive index contrast between the layers, which is consistent with the energy argument presented in section II.1.1.

As discussed earlier, the boundary conditions for the TE and TM polarizations are different and so are their photonic band diagrams. They are often plotted on the same graph for convenience using the positive β axis for the TE polarization and the negative β axis for the TM polarization [Fig.4].¹⁰

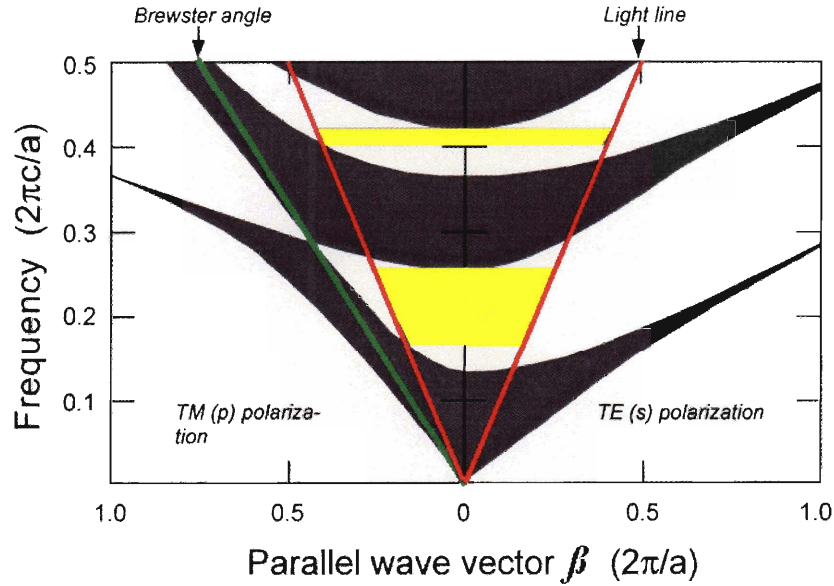


Figure 4: Photonic band diagram. Dark grey regions correspond to propagating states and light grey regions to evanescent states. Regimes where omnidirectional reflectivity is observed are highlighted in yellow. $a=d_1+d_2$ is the multilayer period. (Courtesy of B. Temelkuran)

For the TM polarization in particular, there exists an angle of incidence, called the *Brewster angle*, for which no evanescent state is sustained by the structure [green line in Fig.4]. This may seem to render omnidirectional reflectivity impossible but it isn't so because in practice we are dealing at best with semi-infinite structures on which light is incident from an ambient medium, typically air. As a result, the *group velocity* of the incident light, which by definition is given by:

$$v_g = \frac{\partial \omega}{\partial \beta} \quad (23)$$

is limited to c (or c/n if the medium isn't air). This means that the only states in the photonic band diagram accessible to external light are confined in a cone defined by $\beta \leq \omega/c$ and called the *light cone* [delimited by the two red lines in Fig.4]. It follows that a necessary condition for external omnidirectional reflectivity is that the Brewster angle of the structure be outside of the light cone. This can be achieved by using materials with a large refractive index contrast resulting in wide band-gaps, as demonstrated in ⁵.

II.2 Fabry-Perot micro-cavities

The incorporation and optimization of intentional deviations from periodicity, so called “*defects*”, in a Bragg reflector allow for the creation of localized electro-magnetic modes in the vicinity of these defects. We will refer to such defect layers as the *cavity layers* and to the surrounding layers as the *mirror layers* in analogy with Fabry-Perot interferometers. In particular, it is possible to create a single-mode Fabry-Perot cavity by replacing a quarter-wave layer in the middle of the stack by a half-wave latent layer [Fig.5].

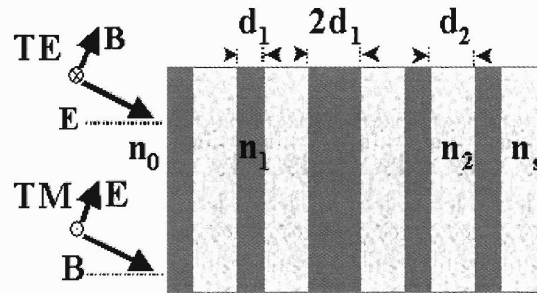


Figure 5: Schematic of the structure of a Bragg reflector with an embedded Fabry-Perot micro-cavity.

II.2.1 Defect states in the photonic band diagram

The photonic band diagram that corresponds to a planar multilayer stack containing a Fabry-Perot cavity is given in Fig.6a.

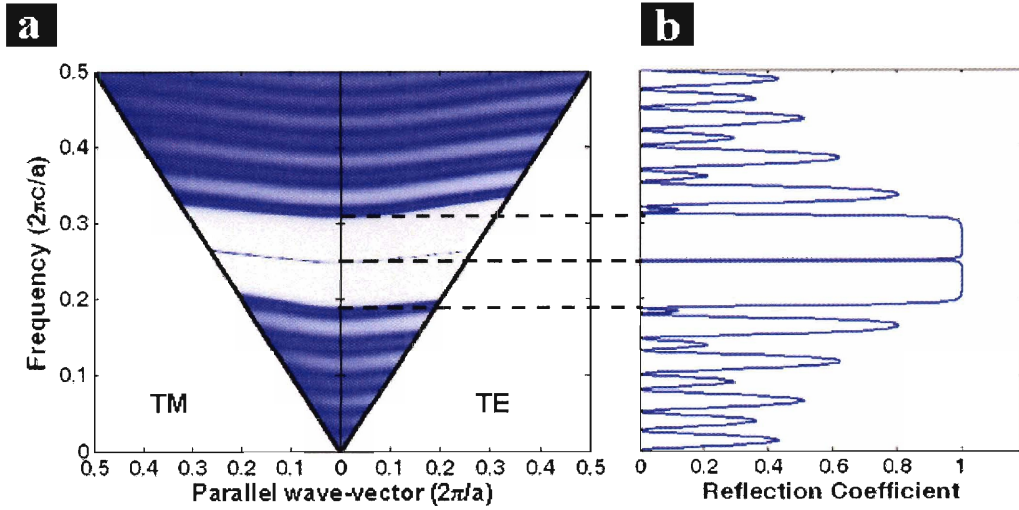


Figure 6: **a** Photonic band diagram of a Bragg reflector with an embedded Fabry-Perot micro-cavity, **b** corresponding reflectivity at normal incidence.

It was calculated with the transfer matrix method (TMM) for a finite structure consisting of 16 alternating layers of indices 2.82 and 1.62, thicknesses $0.365a$ and $0.635a$, with a defect in the middle having an index of 2.82 and thickness of $0.73a$, where a is the multilayer period. The photonic band structure is essentially similar to that of an infinite one dimensional photonic crystal except for the appearance of a cavity mode (thin blue line) inside the photonic band-gap region where photonic states are normally not allowed. Note that this cavity mode exhibits some group-velocity dispersion, which significantly reduces its *field of view* in practice.⁶ The corresponding reflectivity at normal incidence is shown in Fig.6b and reveals that a frequency near the center of the band-gap has zero reflectivity, and thus tunnels through the multilayer structure. This of course does not mean that every single incident photon at this resonant frequency is transmitted through the structure: a large fraction of them are actually reflected at the first few interfaces, as intended by the structure.

To better understand this tunneling mechanism, let's look at the electric field profile in the structure at the resonant frequency. For a Fabry-Perot structure, the middle plane of the cavity layer is a plane of symmetry, which imposes the mode profile to be symmetric or antisymmetric with respect to that plane. Furthermore, a low-index cavity layer can only sustain a symmetric mode due to the π -phase shift at the interface between the cavity layer and the surrounding mirror layers [Fig.7a] while a high-index cavity layer can only sustain an antisymmetric mode due to the 0-phase shift at the interface between the cavity layer and the surrounding mirror layers [Fig.7b].

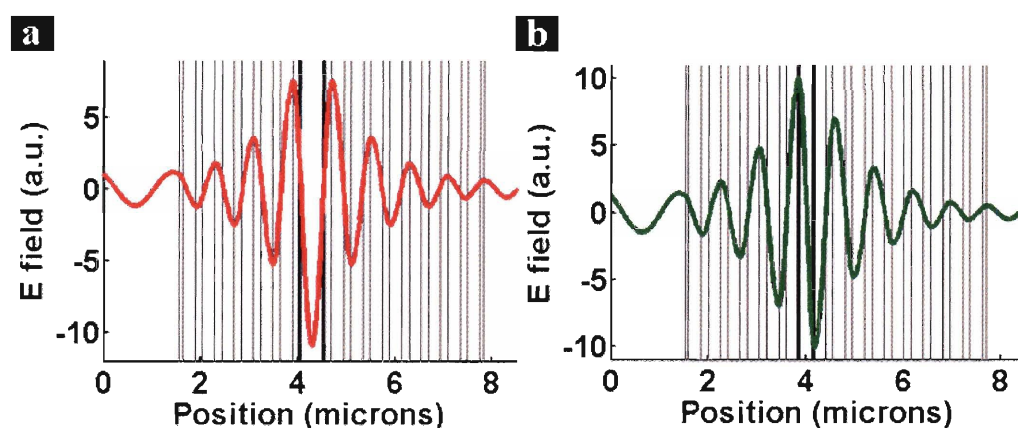


Figure 7: Electric field profile at the resonant frequency for a low index (a) or a high index (b) Fabry-Perot cavity. Note that the first and last layers are half thick to eliminate surface modes.

In both cases, the mode profile exhibits a strong confinement of light in the cavity layer. These trapped photons act as a mirror source that interferes destructively with the photons reflected by the structure. At the resonance frequency, the two contributions cancel each other exactly and the reflectivity of the structure is equal to zero. Off resonance, the confinement of light in the cavity is weaker and there are not enough photons to cancel all the reflected ones: the reflectivity goes up.

Note that the first layer of a Bragg reflector can sustain another type of localized modes called *surface modes*.⁴ These can be eliminated by decreasing the thickness of this first layer by half, which was done systematically in this work.

II.2.2 The quality factor of an optical resonator

The degree of localization of the resonant mode is quantified through the *quality factor* Q of the cavity, which is proportional to the ratio of the energy stored in the resonator U to the power dissipated by the resonator P_d :¹¹

$$Q = \frac{\omega_0 U}{P_d} \quad (24)$$

The energy stored in the resonator is equal to the integral of the electro-magnetic energy density over the volume V of the multilayer structure:

$$U = \frac{1}{2} \text{Re} \left[\int_V \left(\frac{\epsilon}{2} |E|^2 + \frac{\mu}{2} |H|^2 \right) dV \right] \quad (25)$$

where ϵ and μ are the electric and magnetic permeability profiles of the structure. The power dissipated by the resonator is equal to the sum of the radiation losses calculated as the integral of the Poynting vector over the outer surface of the structure S and the absorption losses integrated over the volume V of the structure:

$$P_d = \frac{c}{4\pi} \int_S (E \times B) \cdot da + \frac{\omega}{4\pi} \text{Im} \left[\int_V \left(\frac{\epsilon}{2} |E|^2 + \frac{\mu}{2} |H|^2 \right) dV \right] \quad (26)$$

The E and H profiles can easily be obtained with a TMM calculation.

In practice however, the quality factor is often estimated directly from the spectral response of the Fabry-Perot resonator because the resonant nature of the confined mode makes it very sensitive to loss mechanisms in the cavity layer such as material absorption or scattering, which can be difficult to account for in the TMM calculations. Let's note α_c the attenuation coefficient associated with absorption and scattering in the cavity layer and R_1 and R_2 the reflectance of the two surrounding Bragg reflectors. Then, the overall intensity attenuation factor for a round trip in the cavity of length d is equal to:¹²

$$r^2 = R_1 R_2 \exp(-2\alpha_c d) = \exp(-2\alpha_e d) \quad (27)$$

where $\alpha_e = \alpha_c + \frac{1}{2d} \ln \frac{1}{R_1 R_2}$ is the effective attenuation coefficient per unit length (cm⁻¹

¹). It follows that the photon life time in the cavity is equal to $n/\alpha_e c$ (s) and that the

effective attenuation coefficient per cycle, or $1/Q$, is equal to $\alpha_e c/n\omega_0$. On the other hand, the intensity transmitted through the resonator is given by:¹²

$$I = \frac{\frac{I_0}{(1+r)^2}}{1 + \left(\frac{2F}{\pi}\right)^2 \sin^2\left(\frac{\pi\nu}{\nu_F}\right)} \quad (28)$$

where I_0 is the intensity of the initial wave, $F = \frac{\pi \exp\left(-\alpha_e \frac{d}{2}\right)}{1 - \exp(-\alpha_e d)}$ (29) is defined as the

finesse of the resonator and $\nu_F = \frac{2c}{dn}$ is the frequency spacing of adjacent resonant modes. Then it appears that for $F \gg 1$, the width of the resonance is approximately equal to:

$$\Delta\nu = \frac{\nu_F}{F} = \frac{2c}{dn} \cdot \frac{\pi}{\alpha_e d} = \left(\frac{c}{nd}\right) \cdot \left(\frac{2\pi c}{nd} \cdot \frac{n}{c\alpha_e}\right) = \nu_0 Q \quad (30)$$

In other words, the quality factor can be approximated as the ratio of the full width at half maximum (FWHM) of the resonance ($\Delta\nu$) and the resonant frequency (ν_0).

While this simple analysis provides a lot of insight into the parameters that govern the quality factor, it strictly applies to a cavity surrounded by two metallic mirrors with negligible skin depth. In our case, keep in mind that a significant proportion of the resonant mode is not localized in the cavity layer but in the adjacent mirror layers [Fig.7].

II.2.3 Influence of the cavity optical thickness

The cavity resonant wavelength is directly related to the optical thickness of the cavity layer. Using the Fabry-Perot approximation, we have:

$$\lambda_m = \frac{2\pi n_{cavity} d_{cavity} \cos\theta}{m} \quad (31)$$

where m is an integer, λ_m is the m^{th} resonant mode and θ is the incident angle. Therefore, the resonance wavelength can be shifted by tuning either the thickness or the refractive index of the cavity layer. The actual relation $\lambda_m(d_{cavity})$ calculated with the TMM is plotted in Fig.8a.

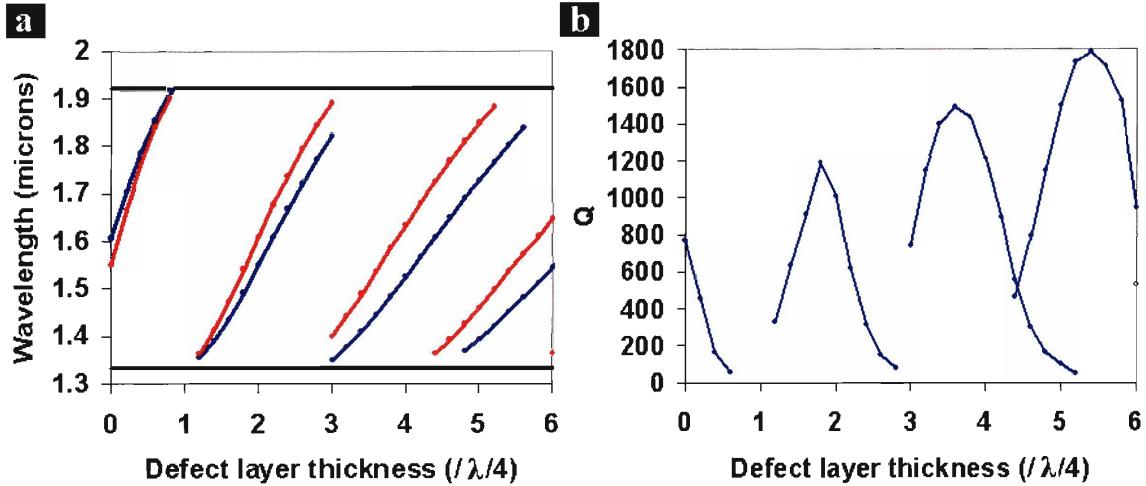


Figure 8: **a** Evolution of the cavity resonant wavelength as a function of the cavity layer thickness. The red lines correspond to a high-index cavity and the blue lines to a low-index cavity while the black lines represent the band-gap edges. **b** Evolution of the quality factor Q as a function of the cavity layer thickness. In all cases, the structure consisted of a 16-bilayer Fabry-Perot structure and calculations were done at normal incidence.

Since the spacing between the resonant frequencies varies as $(n_{cavity}d_{cavity})^{-1}$, there exists a critical cavity thickness above which it becomes smaller than the width of the band-gap, allowing for multiple resonant modes within the band-gap (e.g. $d_{cavity} > 5\lambda/4$ in Fig.9a). Note also that for $d_{cavity} > \lambda/4$, the resonant wavelength associated with a high-index cavity is larger than the one associated with a low-index cavity of identical physical thickness, which is consistent with the electro-magnetic variational theorem.

The quality factor Q depends also strongly on the cavity optical thickness [Fig.9b] and is maximum when the resonant mode is positioned in the middle of the photonic band-gap where confinement is maximum and α_e is minimum. Wider cavities exhibit higher Q factors due to a larger amount of energy stored U (assuming α_e is small).

II.2.4 The density of modes

Because of the induced strong localization of the electro-magnetic field at resonance, Fabry-Perot micro-cavities create opportunities for very interesting applications including optical delay lines, near resonance lasing, bistability and non-

linear switching. In order to study such applications, it is often useful to calculate the *density of modes* (DOM) of the corresponding structures.

The DOM represents the density of allowed wave numbers, or modes, in frequency space and is defined as:¹³

$$\rho = \frac{\partial k_z}{\partial \omega} \quad (32)$$

It has been shown that the DOM of a multilayer stack can simply be calculated from its complex transmission coefficient $t=x+iy$ as follows:¹³

$$\rho = \frac{1}{d} \frac{y'x - x'y}{x^2 + y^2} \quad (33)$$

where d is the physical thickness of the stack. The transmission coefficient t can be calculated with the TMM as described in section II.1.2. In the case of a Fabry-Perot resonator, we find as expected that the DOM is maximum at the cavity resonant frequency and at the band-gap edges [Fig.9].

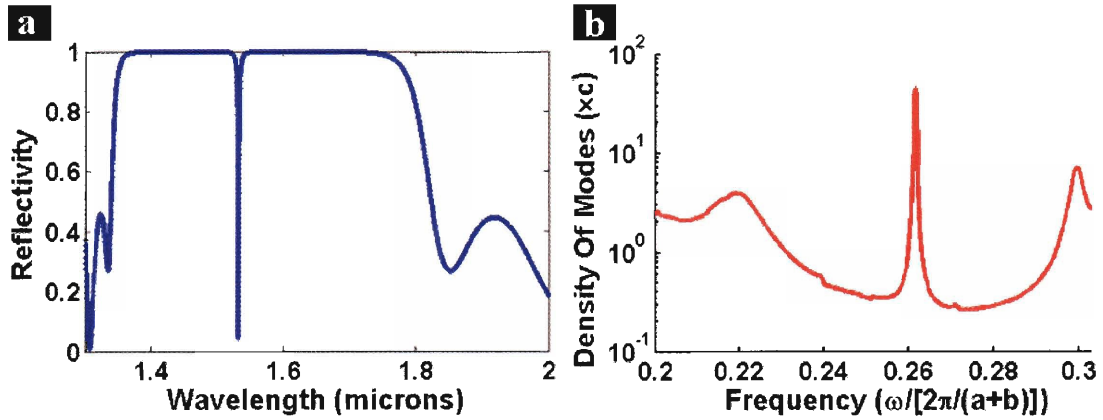


Figure 9: **a** Reflectivity spectrum of a 16 bilayer Bragg reflector made of PEI ($n=1.65$ at $\lambda=1.55 \mu\text{m}$) and As_2S_3 ($n=2.4$ at $\lambda=1.55 \mu\text{m}$) with a low-index Fabry-Perot cavity layer, **b** corresponding density of modes. Here $a+b$ refers to the multilayer period d_1+d_2 .

To illustrate why the DOM can be a critical design parameter, let's consider the case of near-resonance lasing in a Fabry-Perot micro-cavity containing a fluorescent material (e.g. organic dyes). In regions where the density of modes vanishes (typically within the band-gap), there are no states available. As a result, population inversion is very likely but spontaneous emission is impossible and no lasing can be observed. In

regions where the density of modes is high, many states are available. In this case, spontaneous emission is extremely likely but the excited state of the fluorescent material is associated with a very short life time, making population inversion and therefore lasing impossible. For such applications, the combined knowledge of the DOM of the structure and of the absorption and emission characteristics of the active material enable the prediction and optimization of the lasing efficiency. Note that in hollow core transmission fibers, the core itself forms an optical cavity which can be used as a laser cavity if a gain medium is inserted into it. We have demonstrated that the optical pump can then be guided in the fiber while lasing occurs in the transverse direction over an extended length.¹⁴

III Measurements of optical constants

In order to predict the spectral response of a Bragg reflector, a careful characterization of the dispersion relation of the materials composing its multilayer structure is necessary. As shown in sections II.1 and II.2, the real and imaginary parts of the materials refractive indices, n and k , determine the photonic band structure of the Bragg reflector as well as the performance of embedded micro-cavities.

III.1 What is an index of refraction?

The optical properties of materials are determined to a large extent by the electrons and their ability to interact with the electro-magnetic field. The most widely used metric for quantifying the optical behavior of materials is the *index of refraction* \check{N} , or equivalently the *dielectric constant* $\epsilon = \check{N}^2$, which captures the extent to which electro-magnetic waves interact with the material. When an electro-magnetic wave arrives at an interface between air and another material, it can be reflected, transmitted or absorbed and its speed, direction and amplitude are modified. The index of refraction of the material allows us to predict and quantify the relative strength of these different behaviors. In general, \check{N} is a complex number, written $\check{N} = n - ik$, where n is also called the *index of refraction* and k the *absorption or extinction coefficient*.

Let's first consider light propagating in a dielectric material (no absorption, $k=0$). Its electric field sets the electric charges of the material in motion. These moving charges behave as dipoles that act as a new source to re-emit light: the light is said to be *scattered*. The scattered light mixes with the transmitted incident beam with a time delay characteristic of the response time of the material. This produces a phase shift that apparently slows the light down. The ratio of the speed of light in vacuum, c , and the phase velocity in the medium, v_m , is by definition the index of refraction of the medium $n=c/v_m$.^{15,16} It follows from Huygen's principle that the wavelength of light in the medium is given by: $\lambda_m=\lambda_{vac}/n$. Beware of preconceived ideas: most metals, even ITO, can reemit light so efficiently at certain frequencies that their corresponding index of refraction falls well below 1¹⁷ while some exotic materials even exhibit a negative index of refraction.

If however the material is not a dielectric ($k\neq 0$) and the energy of the incident light is sufficient to induce bond vibrations or electronic transitions in the material, the light is strongly absorbed and most of its energy is dissipated into heat (except in fluorescent materials where some of it is re-emitted at a lower frequency). To see how k is related to the absorption of light, let's consider the plane-wave equation:

$$\vec{\nabla}^2 E = \frac{\mu\epsilon}{c^2} \frac{\partial^2 E}{\partial t^2} \quad (34)$$

whose solutions are of the form:

$$E = E_0 e^{i(\omega t - Kr)} = E_0 e^{i(\omega t - 2\pi r / \lambda + i 2\pi k r / \lambda)} = E_0 e^{i(\omega t - 2\pi r / \lambda)} e^{-2\pi k r / \lambda} \quad (35)$$

where K is the complex wave-vector, which is related to the material complex refractive index through the dispersion relation $K=\tilde{N}\omega/c$, λ is the wavelength in free space and r is the distance of propagation in the material. It follows that:

$$I/I_0 = e^{-4\pi k z / \lambda} = e^{-\alpha z} \quad (36)$$

where $\alpha = 4\pi k / \lambda$ (cm^{-1}) is called the *attenuation coefficient*. Therefore, k is a measure of how rapidly the intensity decreases as the light propagates in the material. The penetration depth, also called *skin depth*, of the material is then defined as $D_p = 1/\alpha$.

Note that in the field of fiber optics, the attenuation coefficient α is usually reported in dB/m, which is calculated from the following conversion formula:

$$\alpha_{dB}L = 10 \log_{10}(P_{out} / P_{in}) = 10 \frac{\ln(P_{out} / P_{in})}{\ln(10)} = \frac{10}{\ln(10)} \alpha_{m^{-1}}L \quad (37)$$

where L is the length of the fiber and P_{in} and P_{out} are the input and output power, respectively.

In general, the complex index of refraction is a tensor quantity and one can define coordinate axes (called *principal axes*) such that the corresponding tensor is diagonal:

$$\check{N} = \begin{bmatrix} \check{N}_1 & 0 & 0 \\ 0 & \check{N}_2 & 0 \\ 0 & 0 & \check{N}_3 \end{bmatrix} \quad (38)$$

Cubic crystals and amorphous materials are isotropic ($\check{N}_1 = \check{N}_2 = \check{N}_3$), trigonal, tetragonal, and hexagonal crystals are uniaxial ($\check{N}_1 \neq \check{N}_2 = \check{N}_3$) and triclinic, monoclinic and orthorhombic crystals are biaxial ($\check{N}_1 \neq \check{N}_2 \neq \check{N}_3$). In the rest of this thesis, the expressions ‘refractive index’ and ‘index of refraction’ refer to the complex quantity \check{N} and all materials are assumed to be isotropic, unless stated otherwise.

III.2 Principles of ellipsometry

Ellipsometry is a non-contact, non-destructive optical technique that determines the index of refraction of materials by measuring the change in polarization of a probing light beam upon reflection on a flat sample. It is said to be *self-referencing* because it does not require a reference sample and is largely insensitive to variations in the beam intensity and ambient environment, making this technique highly accurate and reproducible. We’ve characterized various materials of great importance in optics and electronics using this technique and reported our results at <http://mit-photonic-band-gap.mit.edu/Pages/DataBase.html>.

III.2.1 Definition of the ellipsometric parameters

Using Huygen’s principle, Snell’s law and the boundary conditions for an electromagnetic field at an interface, it is easy to derive the reflection coefficients for the TE and

TM polarizations, also referred to as the s and p waves, upon reflection on a sample.⁶ For a homogeneous, isotropic, optically thick sample, which we'll refer to as a bulk sample, we have:

$$r_s = \frac{n_1 \cos \theta_1 - n_2 \cos \theta_2}{n_1 \cos \theta_1 + n_2 \cos \theta_2} \quad (39)$$

$$r_p = \frac{n_1 \cos \theta_2 - n_2 \cos \theta_1}{n_1 \cos \theta_2 + n_2 \cos \theta_1} \quad (40)$$

where subscripts 1 and 2 refer to the ambient medium and the bulk material, respectively. Note that $r_s \geq r_p \geq 0$ for any angle of incidence and that r_p is equal to zero at a unique incidence angle called the *Brewster angle* and given by $\theta_B = \tan^{-1}(n_2)$ [Fig.10a].

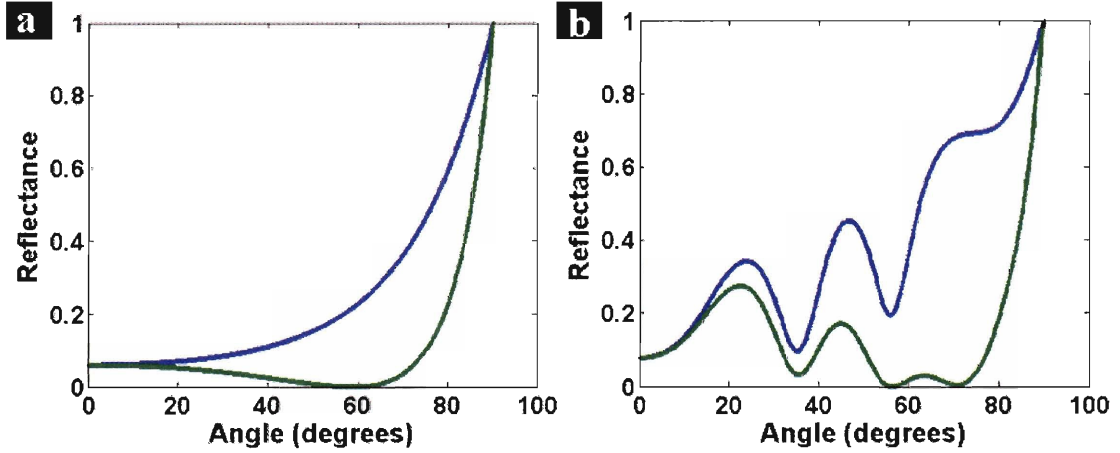


Figure 10: Reflectance calculated (a) for bulk PEI and (b) for a 10 μm As_2S_3 thin film on a PEI substrate, at 1.55 μm . The blue (green) curves correspond to the s (p) polarization.

For a sample consisting of a single layer on a substrate, we have:

$$r_s = \frac{r_{12}^s + r_{23}^s e^{-2i\Phi}}{1 + r_{12}^s r_{23}^s e^{-2i\Phi}} \quad (41)$$

$$r_p = \frac{r_{12}^p + r_{23}^p e^{-2i\Phi}}{1 + r_{12}^p r_{23}^p e^{-2i\Phi}} \quad (42)$$

where $\Phi = 2\pi n_2 \cdot d \cdot \cos \theta_2 / \lambda$ and subscripts 1, 2 and 3 refer to the ambient, the layer and the substrate medium, respectively [Fig.10b]. For samples composed of multiple layers, the TMM is used to compute r_s and r_p .

Clearly the s and p waves have different complex reflection coefficients and therefore experience different amplitude reduction factors and phase shifts upon reflection on a sample. The ratio of r_p and r_s is a complex number that can be written as the product of an amplitude and a phase term:¹⁸

$$\rho = r_p/r_s = \tan \Psi \cdot e^{i\Delta} \quad (43)$$

The ellipsometric parameter Δ is equal to the difference between the phase shifts induced upon reflection for the p and s waves ($\delta_p - \delta_s$) and the ellipsometric parameter $\tan \Psi$ is equal to the ratio of the amplitude of the reflection coefficient of the p and s waves ($|r_p|/|r_s|$). These two parameters, which are the quantities actually measured in an ellipsometry measurement, contain all the information about the thickness and refractive index of each layer composing the sample. While the intensity of the reflected light is not much affected by the presence of a thin dielectric layer, the phase difference between the s and p waves is significant and measurable, making ellipsometry highly sensitive to even very thin layers.

III.2.2 The RPE and RAE configurations

The two most common ellipsometry configurations are the rotating polarizer (RPE) and rotating analyzer (RAE) ellipsometry.¹⁸ Our (Sopra GES5) spectroscopic ellipsometer uses the RPE configuration in the UV-Visible-NIR and the RAE configuration in the IR. Both are based on the same principles so we will only describe the RPE configuration [Fig.11].

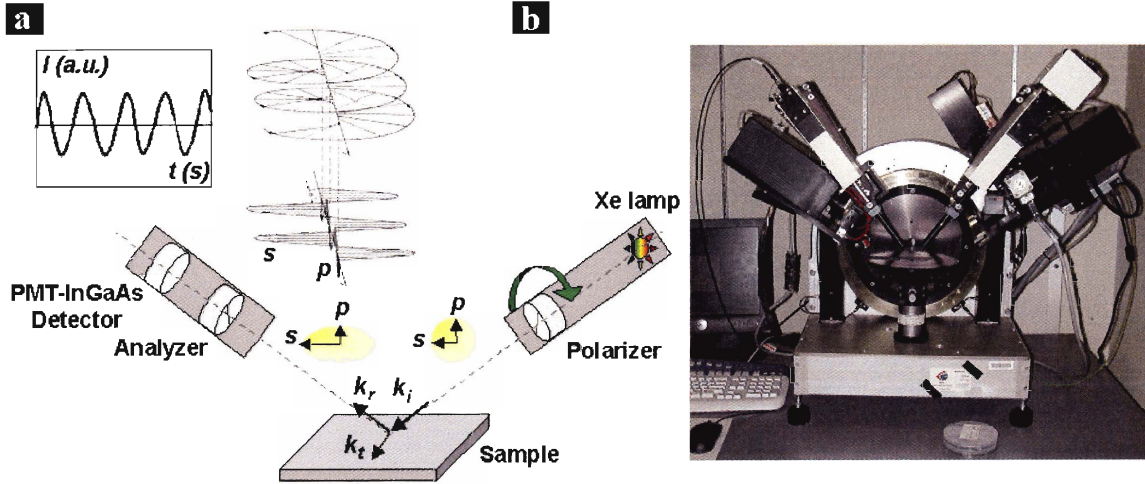


Figure 11: **a** Schematic of the RPE configuration, **b** picture of the Sopra GES5 spectroscopic ellipsometer.

The source, in our case a Xenon lamp, emits light with random polarization. Circularly polarized light is generated by passing the light through a rotating linear polarizer. Upon reflection on the sample, the circularly polarized probing light becomes elliptically polarized with the amount of induced ellipticity depending on $\tan\Psi$ and Δ . The elliptically polarized reflected light then passes through a fixed linear analyzer to generate linearly polarized light with a time dependent intensity. The intensity is measured over time with the appropriate detector and Fourier transformed to yield:¹⁹

$$I(P) = I_0 [1 + \alpha \cos(2P) + \beta \sin(2P)] \quad (44)$$

where α and β are the first Fourier coefficients and P is the polarizer angle. On our ellipsometer, the polarizer rotates at a frequency of 9 Hz, thus allowing for the detection of a large number of periods in a short time. The ellipsometric parameters $\cos\Delta$ and $\tan\psi$ are then derived using the following relations:

$$\tan(\psi) = \tan(A) \sqrt{\frac{1-\alpha}{1+\alpha}} \quad (45)$$

$$\cos(\Delta) = \pm \frac{\beta}{\sqrt{1-\alpha^2}} \quad (46)$$

where A is the fixed analyzer angle. Note that to obtain accurate $\tan\Psi$ and $\cos\Delta$ values, precise alignment of the sample, which ultimately defines the plane of incidence from

which angles and polarizations are defined, and precise calibration of the azimuthal position of the polarizer and the analyzer (typical error below a thousandth of a degree) is critical.

To maximize the amplitude of the detected periodic signal, the analyzer angle is chosen so that its transmission axis is nearly aligned with the long axis of the elliptical polarization of the reflected light. A good approximation consists in setting the analyzer angle to a value close to the measured Ψ value [Fig.12].

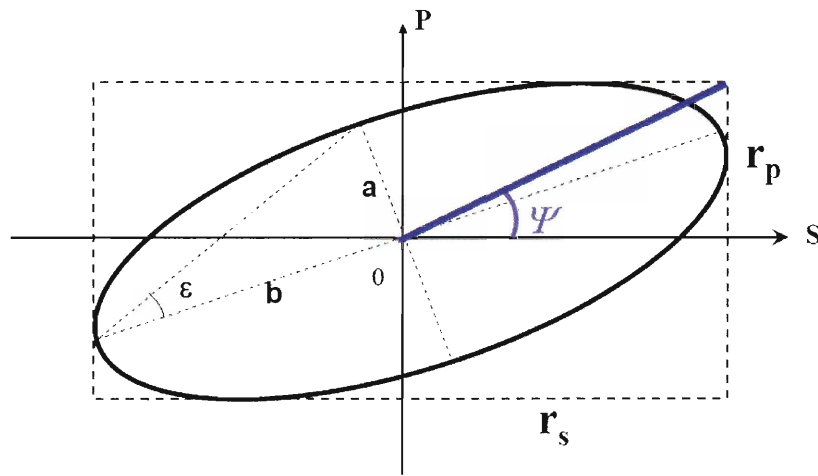


Figure 12: Elliptical polarization represented in the (s, p) plane. (Courtesy of Dr. Richard Sun)

In spectroscopic ellipsometry, the analyzer angle is set at each wavelength to the Ψ value measured at the previous wavelength to avoid taking two measurements for each data point, a method known as *previous tracking*. As a result, $\tan \Psi$ and $\cos \Delta$ can be measured with an average accuracy of $\sim 5 \cdot 10^{-3}$. Note however that when $\tan \Psi$ is close to zero, the reflected light is almost entirely s -polarized and the detected intensity can be very low if the axis of the analyzer is not perfectly aligned with the s -polarization.

In the RAE configuration used on our system, the Fourier coefficients α and β are determined from the measurement of the intensity at only four different analyzer angles ($\theta = 0^\circ, 45^\circ, 90^\circ$ and 135°) using the following relations:

$$\alpha = \frac{I(0) - I(90)}{I(0) + I(90)} \quad (47)$$

$$\beta = \frac{I(45) - I(135)}{I(45) + I(135)} \quad (48)$$

The advantage of the RPE configuration is that the measurement is not affected by the polarization sensitivity of the detectors since at each wavelength the detected light has a fixed linear polarization but it requires the light source to be perfectly randomly polarized to generate a perfectly circularly polarized incident beam.

III.3 Equipment and measurement parameters

The (Sopra GES5) ellipsometer allows for variable-angle spectroscopic ellipsometry and covers a spectral range from 230 nm to 20 microns with three different detectors: a photomultiplier (PMT) detector from 230 nm to 880 nm, an InGaAs detector from 880 nm to 2050 nm and a MCT-A (HgCdTe) detector from 1900 nm to 20 microns. Because these detectors can be non-linear and polarization sensitive (particularly the PMT detector), the system uses attenuators to maintain the detected intensity in a linear regime during the measurements as well as calibrated corrections for all detectors.

The beam size can be adjusted with an aperture and is typically $\sim 2 \times 5 \text{ mm}^2$. It can be further reduced in the visible/NIR region using a set of lenses called *microspots* to $\sim 200 \times 500 \text{ }\mu\text{m}^2$. However, the use of these lenses leads to two potential sources of systematic error: first, the incident beam hits the sample with a range of incident angles ($\sim 3^\circ$), which must be taken into account in the regression analysis to avoid significant over-estimation of k , then the focusing lenses themselves induce a small change in the polarization of the probing light due to their curvature [Fig.10a] and this effect cannot be separated from the polarization change induced by the sample.

Before performing a measurement, it is necessary to precise the appropriate spectral and angular range and step. These four measurement parameters must be chosen carefully because they have a strong influence on the accuracy of the regression analysis that ultimately provides the thickness and the refractive index of the different layers composing the sample. To see why, let's review the important features of the $\cos\Delta$ and $\tan\psi$ spectra for typical samples.

III.3.1 Bulk samples

In the case of a bulk sample, the shape of the $\tan \Psi$ and $\cos \Delta$ spectra depends only on the dispersion relation of the material $\check{N}(\lambda)$.¹⁸ Since $r_s \geq r_p \geq 0$ (see part II.3.1), ψ lies between 0° (near the Brewster angle of the material) and 45° (near normal and grazing incidence) at any wavelength [Fig.13a].

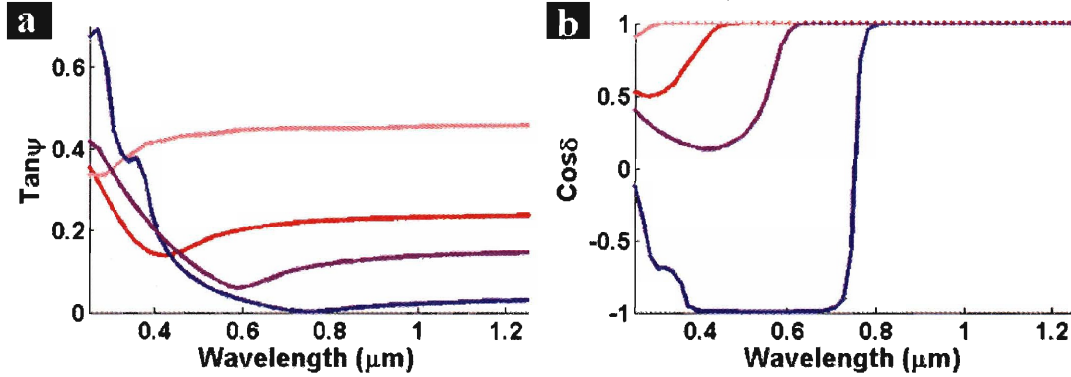


Figure 13: $\tan \psi$ (a) and $\cos \delta$ (b) spectra measured for bulk PEI (pink), As₂S₃ (red), As₂Se₃ (purple) and Si (blue) at 75° . Note the Brewster angle of Si is equal to 75° at $0.75 \mu\text{m}$, while it is below 75° for the other materials in the measured spectral range.

Δ is either equal to 0° or 180° for a dielectric sample depending on whether the angle of incidence is below or above the Brewster angle of the material, respectively, and it lies between 0° and 180° for absorbing materials (the larger the k value, the further from these two values) [Fig.13b]. Δ is always equal to 90° at the Brewster angle. For such samples, the spectral range of the measurement can be limited to the range of interest while the spectral step size must be chosen small enough to appropriately describe the features of the dispersion relation $\check{N}(\lambda)$. Because of the simplicity of the sample's structure, no more than one incident angle is necessary. To improve the accuracy of the Fourier transformation used to calculate $\tan \Psi$ and $\cos \Delta$ (see part II.3.1), the angle of incidence is chosen to maximize the amount of ellipticity while maintaining a decent signal to noise ratio, typically at ± 5 degrees off the Brewster angle of the material.

III.3.2 Thin film samples

In the case of a sample that consists of a single layer on a substrate, the shape of the $\tan\Psi$ and $\cos\Delta$ spectra versus frequency depends on the film thickness and the dispersion relation of both the substrate and the layer. Let's first consider the trajectory that a single-wavelength measurement traces in the (Δ, ψ) plan as a function of the layer thickness d [Fig.14].¹⁸

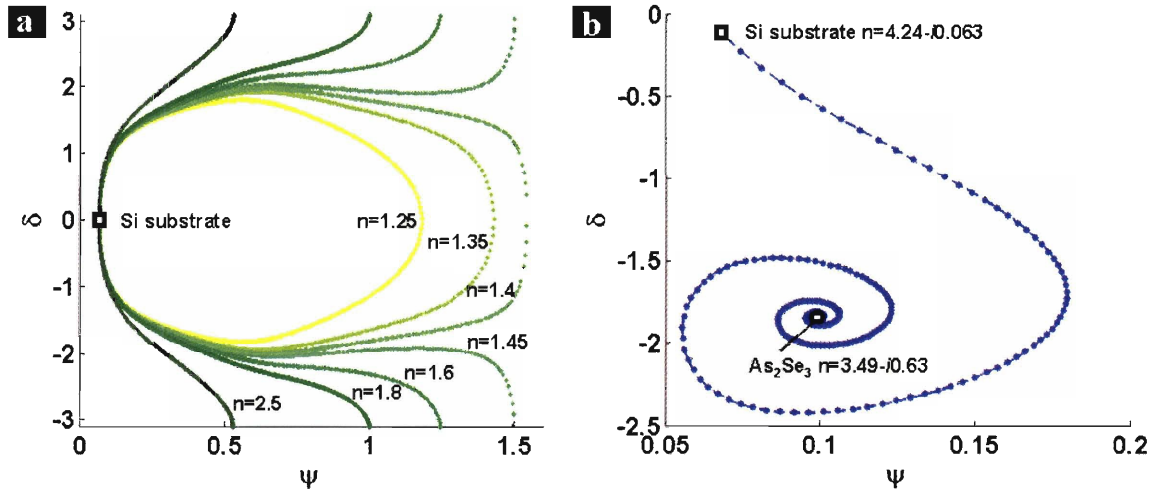


Figure 14: (Δ, ψ) trajectory that a sample consisting of a single layer on a Si substrate traces in the plan (Δ, ψ) as a function of the layer thickness d (a) for a dielectric layer with different n values, (b) for a layer of As_2Se_3 with refractive index at 514 nm $n=3.49-i0.63$.

The trajectory starts at the substrate position (Δ_s, ψ_s) for $d=0$. It then draws a loop that closes on itself before repeating itself as d increases. This is a consequence of the periodicity of $r_{s/p}$ (part II.3.1): each time $\Phi=m\pi$ or equivalently $d_m=m\lambda/(2n_2\cos\theta_2)$, where m is an integer, $r_{12}^{s/p} = r_{13}^{s/p}$ and $t_{12}^{s/p} = -t_{13}^{s/p}$, where r_{12} (r_{13}) and t_{12} (t_{13}) are the reflection and transmission coefficient, respectively, at the interface between layer 1 and 2 (1 and 3).⁶ In other words, the presence of a layer of thickness d_m , so-called *half-wave latent layer*, does not affect the reflection and the transmission of light except for a possible π phase shift. It follows that accurate determination of the refractive index of a half-wave dielectric layer is impossible by a single-angle and single-wavelength ellipsometry measurement. In addition, for very thin layers (<10 nm), it is very difficult to distinguish

one material from another unless they have significantly different refractive indices because their trajectories in the Δ/ψ plan are very close [Fig.14a]. For an absorbing layer, the Δ/ψ trajectory goes from the substrate material position (Δ_s, ψ_s) to the layer material position (Δ_l, ψ_l) as d increases [Fig.14b]. It follows, as expected, that accurate determination of the thickness of a thick absorbing layer is impossible because it effectively behaves as a substrate.

Now it is easy to see that for a sample consisting of an optically thin layer on a substrate, the $\tan\Psi$ and $\cos\Delta$ spectra versus frequency are periodic with period $\omega=c\pi/(d_1n_2\cos\theta_2)$ that is independent of the substrate [Fig.15].¹⁸

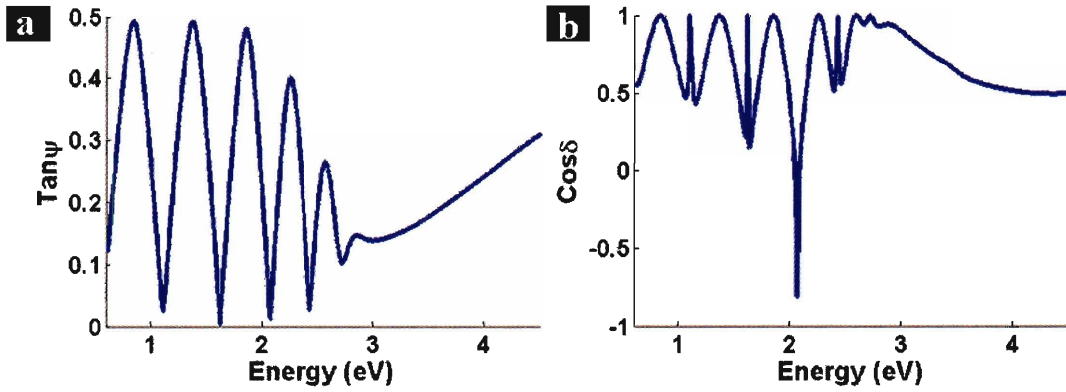


Figure 15: $\tan\Psi$ (a) and $\cos\Delta$ (b) spectra measured at 75° for a 500 nm thick As_2S_3 film on a Si substrate. The film is transparent below $\sim 2\text{eV}$ and bulk above $\sim 3\text{eV}$.

The amplitude of the $\tan\Psi$ oscillations depends solely on the refractive index contrast between the substrate and the layer ($\check{N}_2 - \check{N}_3$). The minimum $\tan\Psi$ value is reached when the half-wave layer condition is met (i.e. $\omega_m = mc\pi/(n_2d\cos\theta_2)$) and therefore depends only on the optical constants of the substrate. $\cos\Delta$ on the other hand is very sensitive to k_2 . In general, the measurement spectral range must be taken significantly larger than the range of interest due to poor accuracy of the regression analysis at the edge of the measurement range and the step size must be chosen small enough to not only appropriately describe the dispersion relations of the different materials but also the $\tan\Psi$ and $\cos\Delta$ oscillations (periodicity and amplitude). The angle of incidence is set to the Brewster angle of the substrate ($\theta_B = \tan^{-1}(n_{\text{substrate}})$) to minimize reflection from the substrate and maximize the

amplitude of the $\tan \Psi$ oscillations (minimal $\tan \Psi$ value close to 0). For samples with thick layers ($>5 \mu\text{m}$) and samples of high structural complexity (multi-layers, inhomogeneous or anisotropic layers, rough interfaces...), two or three incident angles (e.g. $\theta_B - 2^\circ$, θ_B , $\theta_B + 2^\circ$) are necessary to improve the accuracy of the regression analysis due to the large number of unknown parameters. Note that single-wavelength multiple-angle ellipsometry is not recommended because the alignment of the sample is typically angle-sensitive.

III.4 Measurement analysis

The refractive index and thickness of the different layers composing a sample are determined by fitting the measured ellipsometric parameters with a model. The reason for this is that a single layer on a well-characterized substrate corresponds to a minimum set of $2N+1$ unknowns: its thickness and the n and k values at N distinct wavelengths, while the measurement provides only $2N$ independent equations that are the $\tan \Psi$ and $\cos \Delta$ values at all N wavelengths. Note that additional angles do not provide additional independent equations. There is an obvious exception to this which is a uniform, isotropic, optically thick (bulk) sample. In this case, the (n, k) values can be calculated directly from the measured $(\tan \Psi, \cos \Delta)$ as follow:

$$\tilde{N}_{bulk} = \tilde{N}_{ambient} \tan \theta \sqrt{1 - \frac{4\rho \sin^2 \theta}{(\rho + 1)^2}} \quad (49)$$

where θ is the incident angle and $\rho = \tan \Psi \cdot e^{i\Delta}$. In all other cases, the dispersion relation of a certain layer in the sample is obtained by fitting the parameters of standard models to the measured ellipsometric data. Of course one model is usually not sufficient to reproduce all the features of the actual dispersion relation, but the additive character of the *polarizability* allows us to combine several models together. Indeed, the effective polarizability of a material can be written as a term summation of different contributions:^{20,21}

$$\alpha_r = \sum_q \frac{(\epsilon_{r,q} + 2)(\epsilon_{r,q} - 1) + \epsilon_{i,q}^2}{(\epsilon_{r,q} + 2)^2 + \epsilon_{i,q}^2} \quad (50)$$

$$\alpha_i = \sum_q \frac{3\varepsilon_{i,q}}{(\varepsilon_{r,q} + 2)^2 + \varepsilon_{i,q}^2} \quad (51)$$

where $\varepsilon_{r,q} - i\varepsilon_{i,q} = \varepsilon_q = (n_q - ik_q)^2$ is the dielectric constant corresponding to the q^{th} contribution. The final (n, k) values are obtained by using the inverse expression and the following relations:

$$n = \sqrt{1/2 \left[(\varepsilon_r^2 + \varepsilon_i^2)^{1/2} + \varepsilon_r \right]} \quad (52)$$

$$k = \sqrt{1/2 \left[(\varepsilon_r^2 + \varepsilon_i^2)^{1/2} - \varepsilon_r \right]} \quad (53)$$

Because the dispersion relation of dielectrics, semi-conductors or metals have very similar features, most of the models have been developed specifically for one of these categories of materials. We will now review the most common ones.

III.4.1 Dielectrics

Dielectrics are characterized by a large electronic band-gap (>3eV) corresponding to an optical absorption band that lies mostly in the UV range (<413 nm). In the visible-near IR range, the dispersion relation is dominated by an exponentially decaying absorption tail called *Urbach tail*, which is characteristic of absorption resulting from interactions other than band-to-band transitions, such as electron-hole, electron-phonon and electron-impurity interactions [Fig.16].

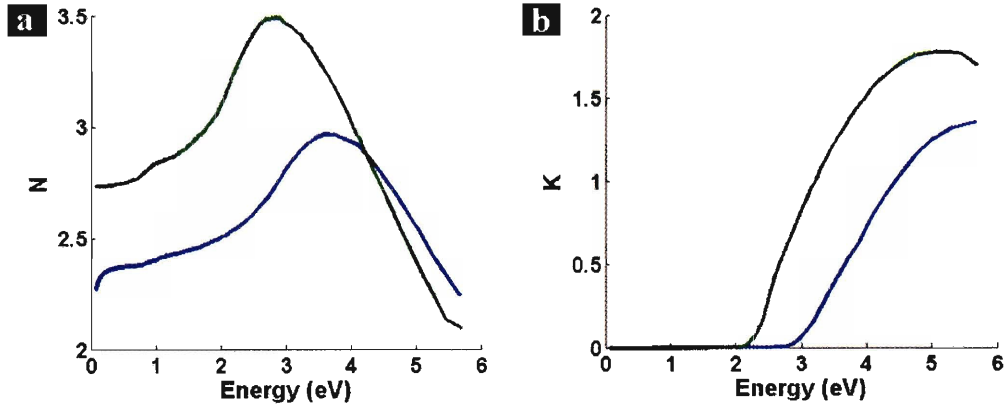


Figure 16: n (a) and k (b) spectra measured for As₂Se₃ (green) and As₂S₃ (blue). The dispersion relations were obtained by fitting the measured data with a Cauchy law below 2.5 eV and 3.2 eV, respectively and using a bulk calculation at higher energies.

The simplest model to describe the spectral dispersion of n in the Urbach tail was proposed by Cauchy in 1830 from empirical observations. It consists of a polynomial with even powers of $1/\lambda$:

$$n(\lambda) = A + \frac{B}{\lambda^2} + \frac{C}{\lambda^4} \quad (54)$$

where A , B and C are constants. An alternative to this law is the Sellmeir law, which is based on the idea that for dielectrics, the dispersion of the real part of the dielectric constants $\varepsilon_1(E)$ can be described using zero-broadened oscillators outside the measured spectrum:

$$\varepsilon_1 = \text{Offset} + \frac{A_1}{E_1^2 - E^2} + \frac{A_2}{E_2^2 - E^2} + \dots \quad (55)$$

where E is the energy (eV) and *Offset*, A_1 , E_1 , A_2 and E_2 are constants. Later, the Urbach equation was introduced to model the spectral dispersion of k .²²

$$k(\lambda) = C_1 e^{C_2 \cdot 12400(1/\lambda - 1/\lambda_0)} \quad (56)$$

where C_1 , C_2 and λ_0 are constants. However, this equation is ill-fitted for a regression analysis because these three parameters are highly correlated, resulting in an infinite number of solutions. A better choice was inspired by the Cauchy law for n and consists in a polynomial with odd powers of $1/\lambda$:

$$k(\lambda) = D + \frac{E}{\lambda} + \frac{F}{\lambda^3} \quad (57)$$

$$\text{or } k(\lambda) = \frac{D}{\lambda} + \frac{E}{\lambda^3} + \frac{F}{\lambda^5} \quad (58)$$

where D , E and F are constants. It is easy to see that the parameters A , B , C (for n) and D , E , F (for k) are not highly correlated since they correspond to different powers of $1/\lambda$ and therefore contribute to different spectral regions. The complete n & k Cauchy law was the most employed model throughout this work.

When the Urbach tail exhibits localized absorption peaks, typically due to band-to-band transitions, these can be taken into account by adding Lorentzian or Gaussian

oscillators to the model. A Lorentzian oscillator is equivalent to the classical mass on a spring with a damping coefficient γ and an external driving force $E(t)$:²¹

$$m \underbrace{\frac{d^2 X}{dt^2}}_{\text{acceleration}} + m\gamma \underbrace{\frac{dX}{dt}}_{\text{dissipation}} + \underbrace{m\omega_0^2 X}_{\text{harmonic restoring force}} = \underbrace{qE(t)}_{\text{time dependent electric field}} \quad (59)$$

$$X = \frac{qE_0}{m(\omega_0^2 - \omega^2 + i\gamma\omega)} e^{i\omega t}$$

where X is the displacement and m the mass of the charge q . From this classical damped harmonic oscillator model it is possible to calculate the induced atomic dipole moment P and the atomic polarizability $\alpha(\omega)$ of the material:

$$P = qX = \frac{q^2}{m(\omega_0^2 - \omega^2 + i\gamma\omega)} E = \alpha(\omega)E \quad (60)$$

Assuming N dipole moments, the dielectric constant of the material is then related to the atomic polarizability by $\epsilon(\omega) = 1 + 4\pi N\alpha(\omega)$, which leads to:

$$\epsilon(\omega) = 1 + 4\pi \frac{Ne^2(\omega_0^2 - \omega^2)}{m((\omega_0^2 - \omega^2) + \gamma^2 \omega^2)} - i4\pi \frac{Ne^2 \gamma \omega}{m((\omega_0^2 - \omega^2) + \gamma^2 \omega^2)} \quad (61)$$

The Lorentzian oscillator works particularly well to describe electronic transitions in amorphous materials. The Gaussian oscillator features a Gaussian line shape for ϵ_i , which means that the absorption goes to zero much faster than with a Lorentzian oscillator:

$$\epsilon_r = A \cdot \text{real}(\exp(-z^2) \text{erfc}(-iz)) \quad (62)$$

$$\epsilon_i = A \cdot \text{imag}(\exp(-z^2) \text{erfc}(-iz)) \quad (63)$$

where $z = 1/\gamma(1/\lambda_0 - 1/\lambda)$. This oscillator is often ideal for describing local molecular bond resonances [Fig.17].

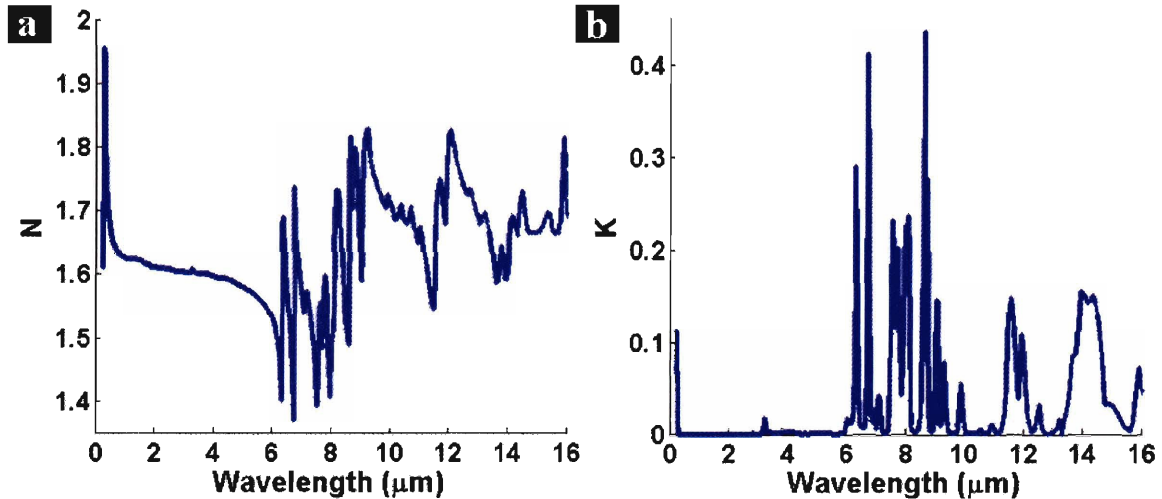


Figure 17: n (a) and k (b) spectra measured for poly(ether-sulfone) (PES). The dispersion in the UV region was fitted with a $n&k$ Cauchy law while absorption from bond resonances above 6 μm was fitted with multiple Gaussian peaks.

III.4.2 Semiconductors

For semiconductors (electronic band-gap below 3 eV), the optical absorption band spans the visible and/or near-IR spectral ranges [Fig.18].

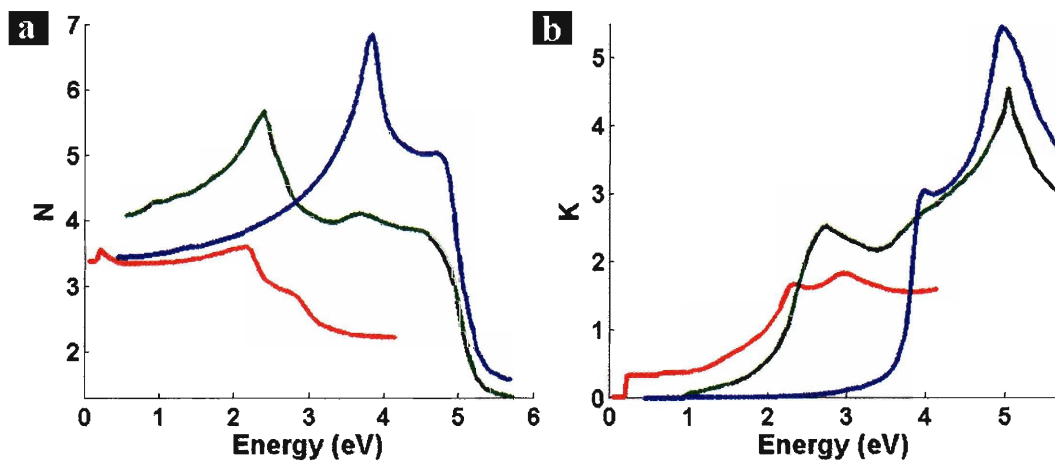


Figure 18: n (a) and k (b) spectra measured for Si (blue), Ge (green) and HgCdTe^{23} (red). The dispersion relations were obtained by direct bulk calculation in the regions of high absorption and by fitting with a $n&k$ Cauchy law elsewhere.

Some large band-gap semiconductors can be modeled with the Cauchy law and additional Lorentzian oscillators but in general such a simple model does not provide an accurate dispersion relation and more specific models must be used.

The *Forouhi Interband Model* is one of the most common models to fit semiconductors and is based on the quantum theory of absorption. k is determined by associating a finite life time with each of the excited states to which an electron can transfer due to photon absorption²⁴ and n is then calculated from the *Kramers-Kronig relations*:²⁵

$$n(E) - 1 = \frac{2}{\pi} P \int_0^{\infty} \frac{E' k(E')}{E'^2 - E^2} dE' \quad (64)$$

where P is the Cauchy principal value (it simply means that the integral should exclude the singularity for $E'=E$). This leads to the following expressions for n and k :

$$n(E) = N_0 + \sum_q \frac{B_q E + C_q}{(E - B_q)E + C_q} \quad (65)$$

$$k(E) = \sum_q \frac{A(E - E_g)^2}{(E - B_q)E + C_q} \quad (66)$$

where N_0 is the value of n at high energy (theoretically 1 but N_0 usually takes larger values due to the finite measurement range), E_g corresponds the optical band-gap energy defined as the energy for which $k(E)$ has its absolute minimum, and A , B_q , C_q are three parameters that characterize each electronic transition q . B_q is called the first intermediate parameter and is equal to $A/Q(-B^2/2 + E_g B - E_g^2 + C)$ and C_q is called the second intermediate parameter and is equal to $A/Q((E_g^2 + C)B/2 - 2E_g C)$, where $Q = 1/2(4C - B^2)^{0.5}$ and A , B and C are three independent parameters. Note that in this model the summation of the different contributions to the dispersion relation is made directly on the optical constants and not on the polarizability.

The *Model Dielectric Function* is a more complex model that is used when the topography of the band structure is already well known, from theoretical calculations for instance.^{26,27} The imaginary part of the dielectric constant ε_i is given by:

$$\varepsilon_i(\omega) = \frac{4\hbar e^2}{\pi m^2 \omega^2} \left| \langle c | p | v \rangle \right|^2 J_{cv}(\omega) \quad (67)$$

where \hbar is the reduced Planck's constant, e is the charge of an electron, $\langle c|p|v\rangle$ are the momentum matrix elements for valence (v) to conduction (c) transitions, $J_{cv}(\omega)$ is the corresponding probability of transition and n is the dimension of the corresponding critical point (1,2 or 3). The real part of the dielectric constant ϵ_r is then calculated using the Kramers-Kronig relations.

III.4.3 Conductors

The optical constants of conductors can usually be well modeled by the *Drude law*. The Drude law is based on a modified Lorentz model with no restoring force, which is appropriate to describe free electrons. The damping force γ is still present and represents the ordinary scattering of electrons associated with electrical resistivity. Using the equations from section III.4.1, we find that the dielectric constant is given by:²¹

$$\epsilon(\omega) = 1 - 4\pi \frac{Ne^2}{m(\omega^2 - i\gamma\omega)} \quad (68)$$

$$\text{or } \epsilon_r(\omega) = \epsilon_\infty - \frac{\omega_p^2}{\omega^2 - \omega_\tau^2} \quad (69)$$

$$\text{and } \epsilon_i(\omega) = \frac{\omega_p^2 \omega_\tau}{\omega(\omega^2 - \omega_\tau^2)} \quad (70)$$

where ϵ_∞ is the dielectric constant at high frequency, $\omega_p = (4\pi Ne^2/m)^{1/2}$ is the plasma frequency and $\omega_\tau = \gamma$ is the scattering frequency.

Assuming that $\omega_\tau \ll \omega$, the optical response of conductors can be approximated as follow: at high frequencies, the index of refraction is real and waves propagate freely (UV transparency) while for frequencies lower than the plasma frequency, ϵ is purely imaginary and the field decays exponentially with distance from the surface [Fig.19].

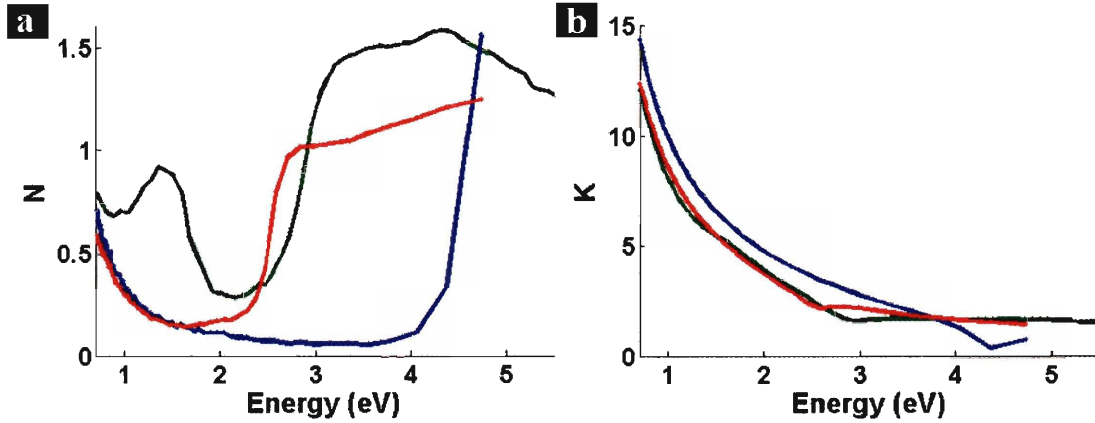


Figure 19: n (a) and k (b) spectra measured for Cu (blue), Au (green) and Ag (red). The dispersion relations were obtained by direct bulk calculation.

When fitting the ellipsometric parameters measured for a thin conductive layer using a Drude type dispersion law, not only can the optical properties of the layer be inferred but also most of its electrical properties. Indeed, given the Drude's parameters, the conductivity of the layer can be calculated as follows:

$$\sigma(S/m) = \epsilon_0 \frac{\omega_p^2}{\omega_\tau} \quad (71)$$

where ϵ_0 is the permittivity in free space. Since the fit also provides the thickness of the layer, the resistivity can then be deduced. The same parameters can be used to calculate the free carrier density and mobility as follow:

$$N(at/cm^3) = \frac{\epsilon_0 \omega_p^2 m^*}{e^2} \quad (72)$$

$$\mu(cm^2/V/s) = \frac{e^2}{\omega_\tau m^*} \quad (73)$$

where m^* is the effective mass of the free carriers.

III.4.4 Inhomogeneous layers and rough interfaces

If a layer is made of an alloy or a mixture of different materials, its dispersion relation can be determined using *mixed materials models*, which are all based on the *Clausius-Mossotti formula*. For a mixture of two materials with dielectric constants ϵ_1 and ϵ_2 , the effective dielectric constant of the medium $\langle \epsilon \rangle$ is given by:²¹

$$\frac{\langle \varepsilon \rangle - \varepsilon_m}{\langle \varepsilon \rangle + 2\varepsilon_m} = (1-f) \frac{\varepsilon_1 - \varepsilon_m}{\varepsilon_1 + 2\varepsilon_m} + f \frac{\varepsilon_2 - \varepsilon_m}{\varepsilon_2 + 2\varepsilon_m} \quad (74)$$

where ε_m is the dielectric constant of the medium with inclusions and f is the volume fraction of material 2. When the two materials play exactly the same role, $\langle \varepsilon \rangle = \varepsilon_m = (\varepsilon_1 + \varepsilon_2)/2$: this is the *Bruggeman approximation*, also called the *Effective Medium Approximation* (EMA).²⁸ When one material, let's say material 2, is an inclusion in the other material (material 1), then $\varepsilon_m = \varepsilon_1$. More accurate expressions have been derived when material 2 is assumed to be in the form of spherical inclusions^{29,30} or ellipsoidal inclusions.³¹ Keep in mind that grain size, grain boundary composition... can also influence the n and k values of the layer.

These approximations can be used for example to determine the change in density of a layer grown using different techniques or under different conditions compare to a reference layer. Such a layer can be modeled as a mixture of the reference layer material (ε_1) and air or *void* ($\varepsilon_2=1$). Positive or negative volume concentration of void f signifies that the layer is less or more dense than the reference layer, respectively. Another example are oxynitrides which can be modeled as a mixture of silicone dioxide and silicon nitride. Finally, the EMA is typically used to model rough interfaces as additional layers made of a mixture of the two adjacent layer materials and whose thickness depends on the interface RMS roughness. The main effect of rough interfaces is to scatter the probing light, thus reducing the detected intensity, and to smooth the $\tan \Psi$ and $\cos \Delta$ spectra. For typical interface RMS roughness, these effects are dominant at shorter wavelengths (UV-visible range). Scattering does not affect much the accuracy of ellipsometry measurements since only the ratio of the s and p reflection coefficients matters, not their absolute values. Problems can occur, however, when the sample roughness is high enough to couple the s and p polarizations and induce energy transfer between the two. As a general rule, samples with RMS roughness larger than $1/10^{\text{th}}$ the the probe wavelength are not appropriate for ellipsometry measurements.

III.4.5 Fitting

The regression analysis used to fit the generated model to the measured ellipsometric parameters is based on the *Levenberg-Marquardt algorithm*,³² one of the standard algorithms for the least-square approximation of non-linear models. Because $\tan \Psi$ can take very high values compare to $\cos \Delta$, a direct regression on these two parameters tends to put a larger weight on $\tan \Psi$ than $\cos \Delta$ and the fit is not optimized. Therefore, it is often better to run the regression on $\cos(2\Psi)$ (also called α) and $\sin(2\Psi)\cos(\Delta)$ (also called β) instead since both quantities are bonded between -1 and 1.

The quality of the fit is estimated through a merit function, the most common one being the Mean-Squared Error (MSE):

$$MSE = \frac{1}{2N - M} \sum_1^N \left[\left(\frac{\tan \psi_i - \tan \psi(\bar{u}, \bar{a})}{\sigma_{\psi,i}} \right)^2 + \left(\frac{\cos \Delta_i - \cos \Delta(\bar{u}, \bar{a})}{\sigma_{\Delta,i}} \right)^2 \right] \quad (75)$$

where ψ_i and Δ_i denote the measured values, $\psi(\bar{u}, \bar{a})$ and $\Delta(\bar{u}, \bar{a})$ the calculated values and $\sigma_{\psi/\Delta,i}$ is the standard deviation of ψ/Δ at the i^{th} data point. The vector \bar{u} contains the known (fixed) parameters while the vector \bar{a} contains the unknown (variable) model parameters that are varied in order to fit the experimental data. N is the total number of (ψ, Δ) points and M the total number of variable parameters. Since the contribution of each data points is divided by the square of the standard deviation of that data point, the contribution of noisy data points tends to be much smaller. The error associated with each fitting parameter is typically below 0.25% for a good fit. The uniqueness of the solution depends strongly on the degree of correlation between the different fitting parameters and therefore a correlation matrix is provided with the result of the fit. If the correlation matrix exhibits elements larger than 0.997, then the corresponding two entry parameters are considered strongly correlated. This typically happens when too many parameters are used for the fit and can usually be reduced by increasing the number of angles used for the measurement.

To confirm the correctness of the calculated n and k values, one can investigate their Kramers-Kronig consistency or compare the measured n and k values with tabulated values. In the latter case, it is critical to keep in mind that not all materials can be

fabricated and/or deposited in a very reproducible manner. Single-crystal materials (e.g. Si) have extremely reproducible optical constants and are often used as the substrate material for this reason. Other materials such as silicon thermal oxide and silicon nitride deposited by low-pressure chemical vapor deposition (LPCVD) also have fairly reproducible optical constants. But polycrystalline metals, nitrides deposited by plasma enhanced chemical vapor deposition (PECVD), oxides (e.g. indium-tin-oxide ITO) and many other materials exhibit strong variations in their refractive index.

III.4.6 Point to point n & k calculation

For samples that consist of a single layer on a substrate, the (n, k) values can theoretically be calculated from the measured $(\tan \Psi, \cos \Delta)$ values at each wavelength if the layer thickness is known with high accuracy (typically determined after fitting). This technique is called *point to point n & k calculation*. The difficulty however is that very often the data does not provide a unique answer due to the uncertainty on the $\tan \Psi$ and $\cos \Delta$ values, which leads to *branch cuts* in the solution. To eliminate this problem, the n and k values at each wavelength are determined using a regression algorithm that searches for the best solution around the value calculated at the previous wavelength or around an input value. It is possible for example to input the n and k values previously determined by fitting the measurement with a dispersion relation. The advantage of this technique is that complex optical features that would require fitting a very large number of parameters can be resolved. The drawback is that the regression output at each wavelength is very sensitive to the starting value and that experimental noise in the measurement is systematically translated into noise in the calculated dispersion relation.

III.5 **Sample preparation**

The most common substrate for ellipsometry measurements is a thick single-side polished Si wafer ($>500 \mu\text{m}$). It is an ideal substrate because its refractive index is well-known and exhibits high absorption in the UV, visible and near-IR and because its rough backside scatters light, which limits coherent reflection at this interface. In the IR, backside reflection increases because the absorption coefficient of Si decreases and

because these wavelengths are not scattered as efficiently. To limit this effect, heavily doped Si wafers are preferred. When double-side polished or transparent substrates are used (e.g. glass slides), backside reflection can be avoided by using a small beam size (microspots) and placing a piece of tape on the back side of the sample.

Our chalcogenide glass films were deposited by thermal evaporation (pressure $<2.10^{-5}$ Torr, deposition rate ~ 100 Å/s) and were annealed for 2 h at 180°C under vacuum. Some of these glasses exhibit very robust stoichiometry of bonding (e.g. As_2Se_3 , As_2S_3) and therefore have fairly reproducible optical constants when evaporated directly from the glass compound while other doped compositions (e.g. GeAsSeTe alloys) require co-evaporation of the different elements. The observed differences between the measured refractive indices and literature values were attributed to variations in the glass stoichiometry and/or in the density of the films. No absorption due to traces of H_2O , H_2Se and other oxide impurities³³ was measured in our samples within the resolution of the ellipsometer.

Polymer films were prepared by spin coating (Laurell Tech. Corp. WS-400A-6NPP/LITE) of a polymer solution at 1500 rpm (in air) and were kept for 1 h under vacuum at 100°C to ensure complete evaporation of the solvent. The polymer solutions were obtained by dissolving purchased polymer films in the appropriate solvent, for example:

- 25-micron PES film in N,N-Dimethylformamide (DMF)
- 13-micron PEI film in 1-methyl-2-pyrrolidinone.

Using the measured n and k values [Fig.17] and the TMM, we calculated the transmission spectra corresponding to the purchased polymer films and obtained a good agreement in the position and the shape of the different absorption peaks with experimental spectra (from our own measurement as well as from literature^{34,35}) [Fig.20].

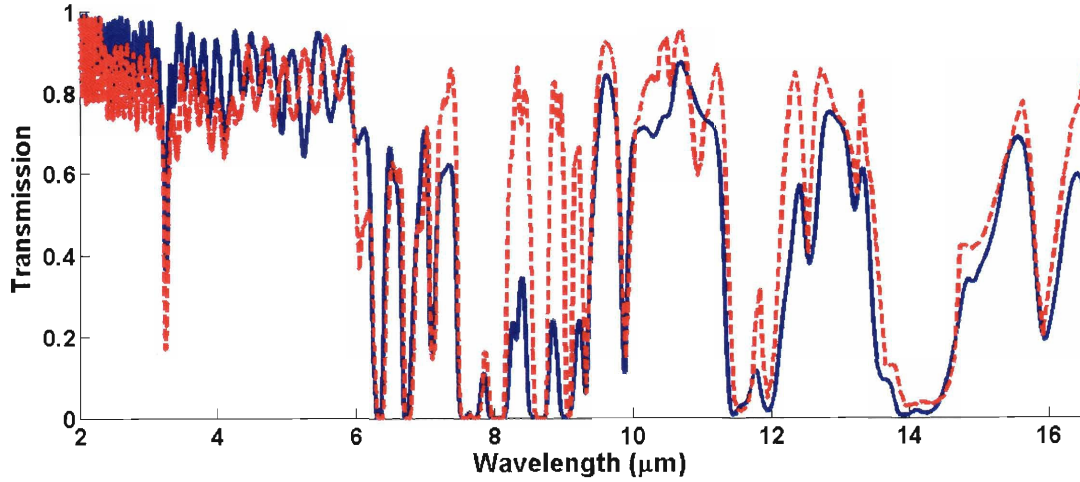


Figure 20: Transmission spectra measured by FTIR (blue) and calculated with the TMM (red) for a 25 μm thick PES film.

IV Fabrication of photonic band-gap fibers

As described in section II, one-dimensional photonic band-gap structures can be designed to reflect and confine light with very high efficiency. This opens opportunities to create high-performance waveguides or reflecting yarns with innovative integrated capabilities. The fiber fabrication is based on an *optical fiber drawing process* that consists in thermo-mechanically drawing down a macroscopic preform into hundreds of meters of multilayer fiber with precisely controlled sub-micrometer layer thickness. While this process is widely used in the silica fiber industry and guarantees the production of kilometers of fibers at low cost and high uniformity, applying it to the fabrication of photonic band-gap fibers is challenging. Indeed, in order to draw such a composite structure while maintaining structural order through the induced rough thermal and stress cycles, it is critical to find two amorphous materials whose glass transition temperatures T_g , coefficients of thermal expansion CTE , and viscosities $\eta(T)$ are similar. Unfortunately, similar thermo-mechanical properties generally come at the cost of similar refractive indices, making such materials pairing inadequate to fabricate high performance Bragg reflectors. We have selected different chalcogenide glasses as possible high-index materials, including arsenic triselenide (As_2Se_3), arsenic trisulfide

(As₂S₃), and Ge, As, S, Se, Te compounds (GAST) which were purchased from Alfa Aesar/Strem Chemicals (purity 99.999%) or synthesized in our own laboratory [Fig.21], and two high T_g polymers as possible low-index materials: poly(ether-sulfone) (PES) and poly(ether-imide) (PEI) purchased from Goodfellow Corporation, GE, Honeywell or other.

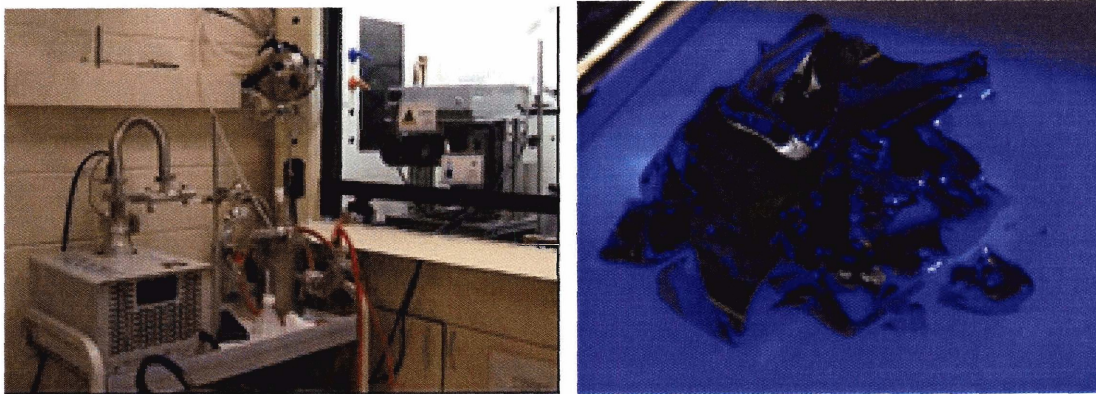


Figure 21: Chalcogenide glass synthesis line. Pure elements are placed in a silica glass ampoule that is seal under vacuum and then placed in a rocking furnace (left) to create the glass compound (right). (Courtesy of Dr. M. Bayindir)

The table below summarizes the important optical and thermo-mechanical properties of the materials most used in this thesis:

Materials	$n @ 1.55 \mu\text{m}^{17}$	$T_g^{36,37} (^{\circ}\text{C})$	$T_m^{36,37} (^{\circ}\text{C})$	$CTE^{36,37} (\text{K}^{-1})$
As ₂ Se ₃	2.82	175	260	$25 \cdot 10^{-6}$
As ₂ S ₃	2.4	180	300	$21.4 \cdot 10^{-6}$
PES	1.62	190-220	210	$55 \cdot 10^{-6}$
PEI	1.65	215	219	$31-56 \cdot 10^{-6}$

More refractive index values are available at <http://mit-photonic-band-gap.mit.edu/Pages/DataBase.html>.

IV.1 Preform fabrication

The first step in the fiber fabrication process is the construction of a macroscopic preform. The high-index chalcogenide glass is first deposited on one or both sides of a free standing low-index polymer film by thermal evaporation [Fig.22a,d].

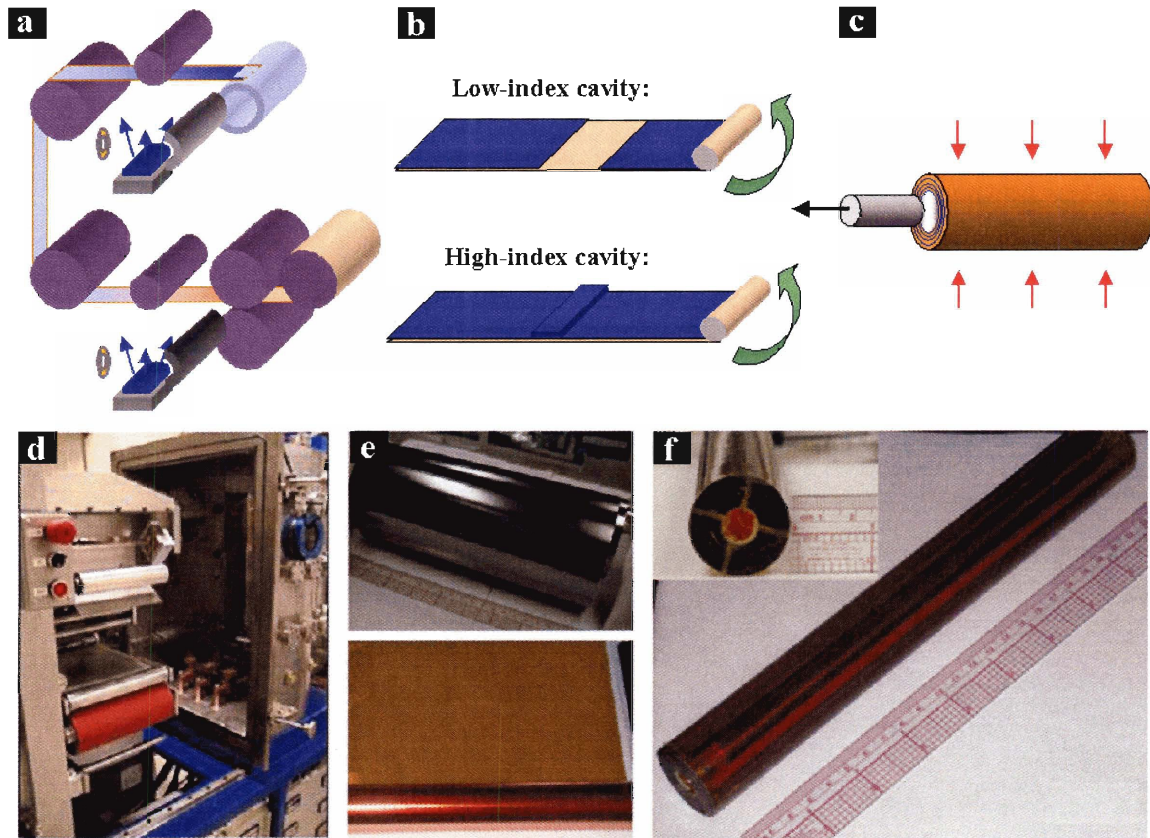


Figure 22: **a d**, Roll to roll thermal evaporator, **b e**, coated polymer films, rolling of the preform and cavity layer incorporation **c** consolidation of the preform, **f**, final preform.

We use a made-to-order roll-to-roll thermal evaporator that can coat meters of film using four tungsten boats (two for each side of the film). The thickness of the deposited film is determined by the speed of the film and the evaporation rate which is measured in-situ with a thickness crystal monitor. Variations along the width of the film are of the order of 5%. The coated film is then wrapped around a borosilicate glass tube (Corning Pyrex) or a Teflon covered metallic rod to create the dielectric mirror layers of a transmission fiber preform [Fig.22b,e]. Additional polymer layers are added to provide mechanical

strength to the fiber until the diameter of the preform is ~ 32 mm. The inner diameter of the preform, typically between 5 and 15 mm, is chosen according to the targeted fiber core dimension. Alternatively, the dielectric mirror layers can be wrapped around a thick polymer cladding to create a reflection fiber preform. One or two additional polymer layers are then added to protect the mirror layers.

The rolling of the mirror layers and the cladding is the most critical step in making a good preform and ultimately good fibers so here are a few tips to do it well. The most important is to ensure that the films are tightly rolled at all times. Therefore, the preform must be held very firmly with at least one hand at all times. When rolling, pressure should be applied downward and forward with both hands spread over the full width of the preform, including the edges which are the most likely to get loose. For the cladding, the thickness of the polymer films should be increased gradually (e.g. 25, 50, 75 then 125 μm) to minimize the amount of air trapped at the interface and the risk of delamination during or after the draw. It is also helpful to insert the first cladding layer in the last mirror layer to ensure better cohesion. Finally, for small core transmission fibers, rolling the preform on a 5 mm tube is quite difficult but it can be made easier by loosely rolling the first few layers and baking them at 150°C for 1 h to induce a tight curvature at the beginning of the film.

Micro-cavities can be incorporated in different ways. A single-mode low-index cavity can be introduced by inserting two back to back pieces of single-side coated films during the rolling of a double-side coated film [Fig.22b]. The width of the two additional films must correspond precisely to the preform circumference. Additional uncoated polymer films can be inserted in between them to create thicker multi-mode cavities. The same process can be used to incorporate high-index cavities using an asymmetric double-side coated film. For a single-mode cavity, one side must be three times thicker than the other. Alternatively, high-index cavities can be obtained by first rolling and consolidating the inner mirror layers and then depositing the cavity layer directly on the consolidated preform by thermal evaporation. The consolidation of the inner mirror layers must be done carefully to minimize the evaporation of the glass, typically at 257°C

for 15 minutes. The outer mirror layers and the cladding can then be rolled on the preform.

Once the rolling process is completed, the preform is tightly wrapped with Teflon and placed in a vacuum oven at 150°C overnight to anneal the stress in the layers and reduce the amount of air trapped in the preform. It is then placed in the *consolidator*, a three-zone horizontal tube vacuum furnace, where it is attached to a rotating motor that continuously rotates the preform around its axis. The preform is preheated for 2h at 170 °C to ensure that its temperature is homogeneous and then consolidated at ~268°C for 60-70 min with a small temperature gradient along its length (+/- 2°C). The actual consolidation time typically depends on the polymer(s) and chalcogenide glass(es) used to make the preform but should be long enough for the cladding to appear completely transparent. If a Teflon covered metallic rod was used to make the preform, it can be easily removed soon after consolidation thanks to the large coefficient of thermal expansion of Teflon [Fig.22c,f] and the preform is then cooled slowly in a vacuum oven at 150°C, then at 80°C and finally at room temperature. If a silica tube was used, it must be etched by placing the cold preform in a bath of hydrofluoric acid (HF) overnight. Because of the fairly large water absorption coefficient of PES and PEI (>0.25 volume % in 24h), the preform must be baked in a vacuum oven at 150°C at least overnight before drawing. To prepare the preform for the draw, both ends are cut flat and the tightest one is attached to the preform holder while the other is kept for the bait-off.

IV.2 Drawing technique

The next step in the fabrication process is the thermo-mechanical drawing of the preform into hundreds of meters of multilayer fiber with precisely controlled sub-micrometer layer thickness. Our fiber draw tower is composed of a (Thermcraft) three-zone vertical tube furnace, a tension-meter, a (Heathway) motorized capstan that controls the speed of the drawing and (Beta LaserMike) laser-micrometers that monitor the outer diameter of the fiber during the draw [Fig.23].

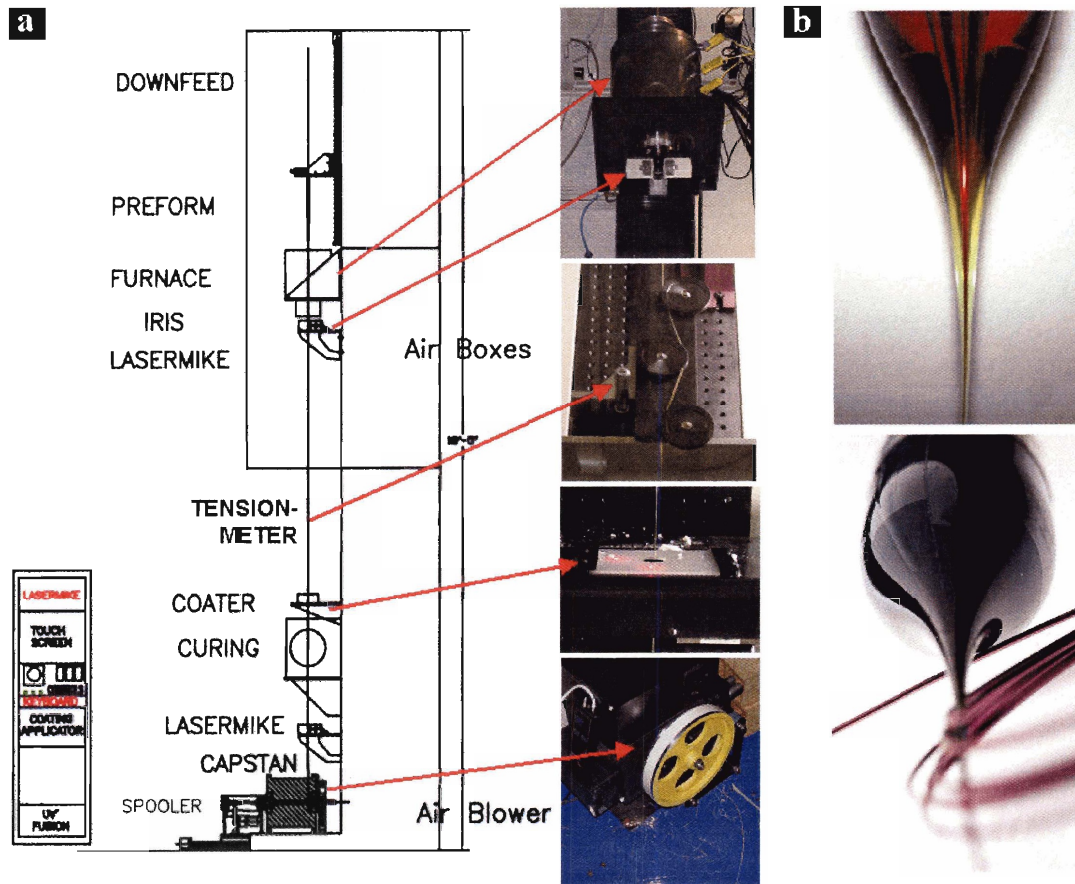


Figure 23: **a** Schematic and pictures of the different parts of the draw tower including the three-zone furnace, the tension meter, the laser micrometer and the capstan, **b** pictures of the reduction cone.

Before each draw, it is critical to verify that the tower is aligned, i.e. that the preform holder, the center of the furnace and the tension-meter are all aligned on the same vertical line. This is done by hanging a weight from the preform holder with a short nylon wire to align the preform holder with respect to the center of the furnace and with a long wire to align the tension-meter. The preform is then mounted to the preform holder and its position is adjusted so that the bait-off appears to be at the center of the furnace. This is critical to ensure a uniform temperature distribution and therefore viscosity distribution across the reduction cone. The temperature of the upper (lower) zone of the oven is kept constant around 190°C (180°C) during the draw. The temperature of the middle zone is first set to 310-315°C to initiate the draw and then reduced between 295 and 305°C during the draw [Fig.24a].

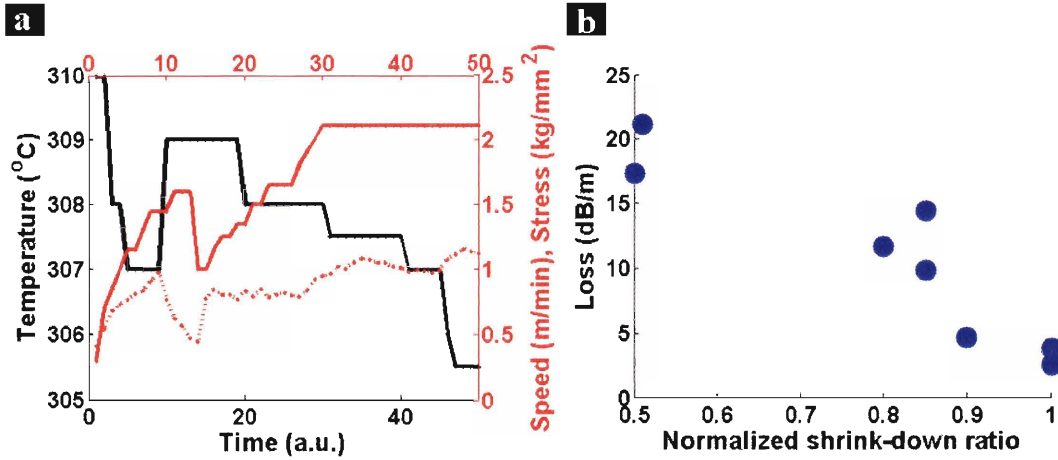


Figure 24: **a** Temperature (black line), capstan speed (solid red line) and stress (dashed red line) profiles recorded over time during an actual draw, **b** influence of the normalized shrink-down ratio on the propagation losses of transmission fibers designed to transmit around 1.55 μm .

The temperature of the middle zone and the capstan speed must be adjusted simultaneously in order to achieve the desired outer diameter while maintaining a high stress [Fig.24a]: high capstan speeds lead to small outer diameters while low temperatures and high stress lead to a good ordering of the mirror layers and minimize deviations from the preform symmetry. At the same time, the stress must be kept below 1200 KPa when the fiber is likely to break. It is also critical to maintain a *normalized shrink-down ratio* (NSD), defined as the ratio of the inner to the outer diameter in the drawn fiber normalized by the ratio of the inner to the outer diameter in the preform - $(D_{inner}/D_{outer})^{Fiber}/(D_{inner}/D_{outer})^{Preform}$ - close to 1 to avoid chirping of the mirror layers due to volume conservation. Deviations from 1 lead to poor fiber quality (high propagation losses, low Q micro-cavities...) as shown in Fig.24b. In general, the NSD improves as the stress level increases. It can be further modified by adjusting the nitrogen pressure flowing through the core of the preform and the fiber, thus modifying the stress state at the inner surface of the reduction cone. Finally, the spectral position of the fundamental photonic band-gap is controlled during the draw by the optical monitoring of the outer diameter of the fiber and by in line reflectivity measurements. Fig.25 shows that the two are strongly correlated, as expected from Eq.1.

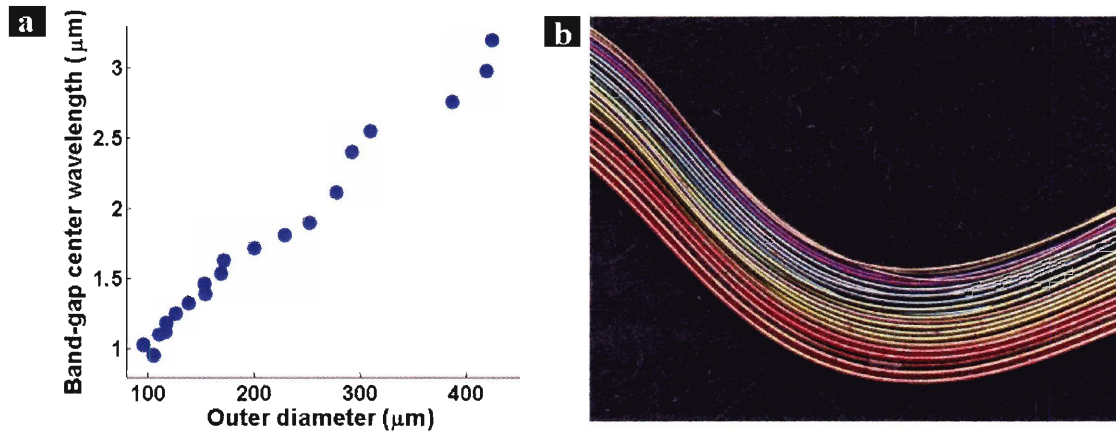


Figure 25: **a** Correlation between the fiber outer diameter and the center wavelength of the fundamental photonic band-gap during an actual draw, **b** shift of high order band-gaps across the visible with decreasing diameters (bottom to top) in reflection fibers.

In stable regimes, the standard deviation on the outer diameter is typically below 3%.

In order to go down to very small diameters, it is useful to increase the capstan speed to 2 m/min or more while still at high temperature ($>305^{\circ}\text{C}$) until the outer diameter is close to the targeted value. This allows the reduction cone to evolve quickly towards its optimal shape and leads to lower middle zone temperature later in the draw. If however the middle zone temperature is lowered too fast, the shape of the reduction cone freezes before reaching its equilibrium shape and increasing the capstan speed does not lead to a significant decrease in diameter. When using this technique for transmission fibers, keep in mind that the core is likely to collapse in the high temperature regime and that moderate nitrogen pressure is therefore necessary.

IV.3 Scanning Electron Microscopy of fiber cross-sections

Fiber cross-sections are observed by Scanning Electron Microscopy (SEM) to gain information on the fiber structure after the draw. The samples are prepared by cutting short fiber sections and dipping half of their length in epoxy resin [Fig.26].

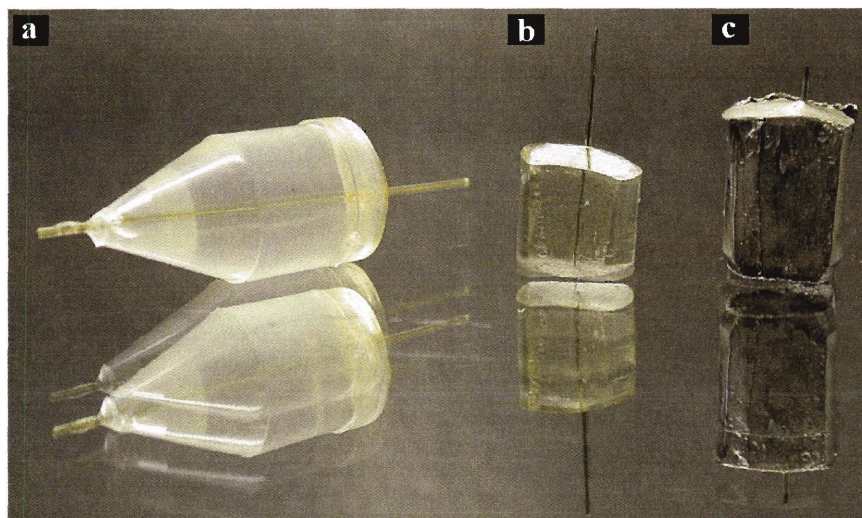


Figure 26: Different steps in the sample preparation: **a** a piece of fiber is half dipped in epoxy, **b** the epoxy is shaped to fit the sample holder of the microtome and the free fiber end is polished, **c** the sample is sputtered with gold to avoid charging during SEM.

The free end of the fiber is polished with a (Ultracut E, Reichert-Jung) microtome. The sample is cooled down to -90°C and covered with ice to provide mechanical support. The fiber end is first shaved off with a glass knife cooled down to -120°C until the fiber cross section is perfectly flat. Decreasingly thin slabs of the fiber, down to a couple nanometer thick, are then removed to obtain a very smooth surface and eliminate as much as possible cracks induced by the initial cut. Finally, the fiber end is polished with a diamond knife. Once removed from the microtome, the sample is rinsed with ethanol to melt the ice water and placed in a vacuum oven at 60°C for an hour to evaporate the residual water and solvent. The polished sample is covered with a ~ 10 nm thick gold coating using a (Denton Vacuum) sputter-coater to prevent surface charging during SEM imaging.

SEM micrographs are taken with a (JEOL) scanning electron microscope using either a secondary electron detector or a backscattered detector when high contrast between the PES and As_2Se_3 layers is desired. They usually demonstrate very good layer uniformity and ordering all around the fiber circumference as well as good adhesion between the polymer and chalcogenide glass layers even after the rigorous thermal and stress cycles associated with fiber drawing [see Fig.29]. But they can also reveal potential defects such as layer delamination (Fig.27a - indicating poor preform

consolidation or very high stress during the draw), layer chirping and ellipticity (Fig.27c - indicating that the preform was not well centered in the furnace and/or low stress during the draw), holes in the cladding (indicating that the initial polymer films and/or the preform were not backed long enough to remove all absorbed gas and water) or the unavoidable inner seam corresponding to the beginning of the roll (Fig.27b,d).

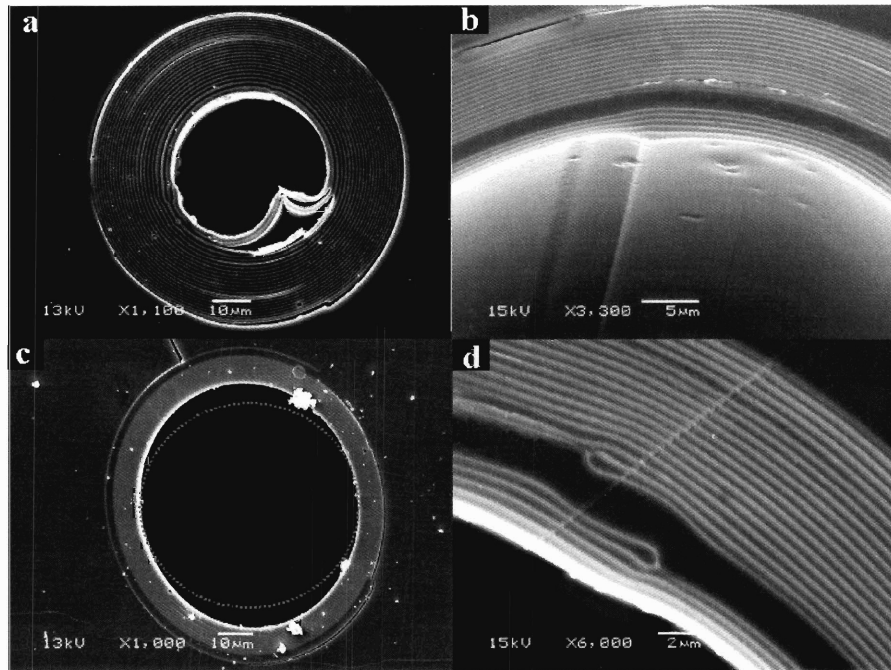


Figure 27: **a** Layer delamination, **b** inner seam, **c** elliptical deformation and **d** layer overlap in the micro-cavity. All these fibers are hollow core transmission fibers.

In addition, these SEM micrographs are useful to obtain the exact thickness of each individual layer, which is used as input parameter in TMM calculations.

V Reflection Fabry-Perot fibers

Polymer fibers are ubiquitous in applications such as textile fabrics because of their excellent mechanical properties and the availability of low-cost, high-volume processing techniques; however, control over their optical properties has so far remained relatively limited. Conversely, dielectric mirrors are used to precisely control and manipulate light in high-performance optical applications, but the fabrication of these

typically fragile mirrors has been mostly restricted to planar geometries and remains costly. Weber and coworkers³⁸, for example, reported the fabrication of freestanding, graded-thickness polymeric dielectric mirrors with relatively low refractive-index contrast between adjacent birefringent layers. In this section we show that it is possible to combine some of the advantages of each of these seemingly dissimilar products in the fabrication of polymeric fibers with an exterior multilayer dielectric mirror to create the potential for new conformal reflector functionalities and flexible radiation barriers. In addition, we show that by incorporating Fabry-Perot micro-cavities in their multilayer structure, the spectral response of these mirror fibers can be uniquely tailored. Such fibers, which we will refer to as Fabry-Perot fibers, could be used as optical filters and optical switches in telecommunications or incorporated into woven fabrics for precise spectral identity verification.

V.1 Reflectivity measurements

Reflection from single fibers or parallel fiber arrays is measured with a (Bruker Optics Hyperion Infrared Micro-spectrometer) Fourier Transform Interferometer (FTIR) coupled to an infrared microscope [Fig.28].

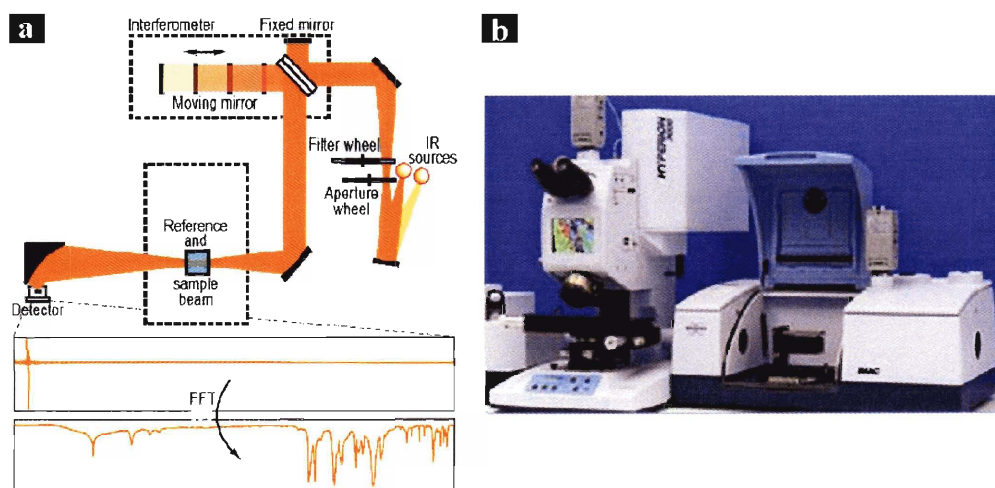


Figure 28: **a** Schematic of a Fourier Transform Interferometer (FTIR), **b** picture of the Bruker Optics Hyperion Infrared Micro-spectrometer. (Courtesy of Bruker Optics)

The microscope has two available detectors: a silicon detector (400 nm to 1.1 μm) and a MCT detector (900 nm to 24 microns) while the FTIR offers two sources: a tungsten halogen lamp (250 nm to 2.5 μm) and a silicon carbide globar lamp (1.5 to 40 μm) and two beam-splitters: a Quartz beam-splitter (400 nm to 1.1 μm) and a KBr beam-splitter (1 to 25 μm). This allows for reflectivity measurements to be performed anywhere from 640 nm to 20 microns. All reflectivity spectra are normalized by a background reference measured with a flat silver mirror.

The microscope objective lens has a numerical aperture (NA) of 0.58 resulting in a detection cone half-apex angle of 35° . Because of this angular averaging, theoretically sharp features in the band-gap such as high Q cavity resonant modes are smeared out in the measured spectra. For example, we have observed single-mode Fabry-Perot resonances at 1.74 μm [Fig.29a] and 3.2 μm [Fig.29b] in 240- μm and 460- μm diameter reflection fibers, respectively, and measured an experimental Q factor of 31, well below the theoretical value at normal incidence of 85.

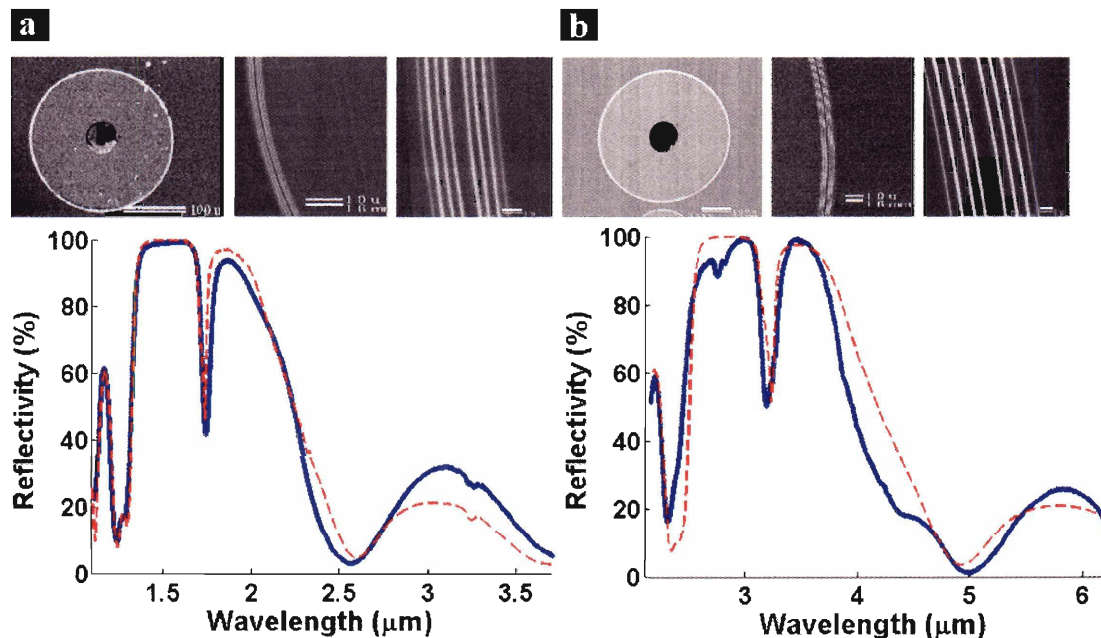


Figure 29: SEM micrographs (top) and reflectivity spectra (bottom) measured (solid blue lines) and calculated (dashed red lines) for a 240- μm (a) and a 460- μm (b) diameter reflection fiber. The fibers were made of As_2Se_3 and PES and contained a single-mode low-index Fabry-Perot cavity surrounded by 6 bilayers.

To account for this effect in TMM calculations, a weighted average of the electric field must be performed over the experimental range of incident angles for both polarization modes, where weights are a cosine function of the corresponding incident angle. Very good agreement can then be obtained between computed and measured spectra despite the one dimensional planar stack approximation when the exact layer parameters determined by SEM imaging and spectroscopic ellipsometry are used as inputs in the calculation [Fig.29]. This is a further confirmation of uniform layer thickness control, good interlayer adhesion, and low inter-diffusion.

In order to characterize the resonance of micro-cavities with high quality factor and very small field of view,⁶ we perform narrow-band reflectivity (NBR) measurements using a (Photonics Tunics plus) tunable laser emitting from 1.49 to 1.62 μm [Fig.30].

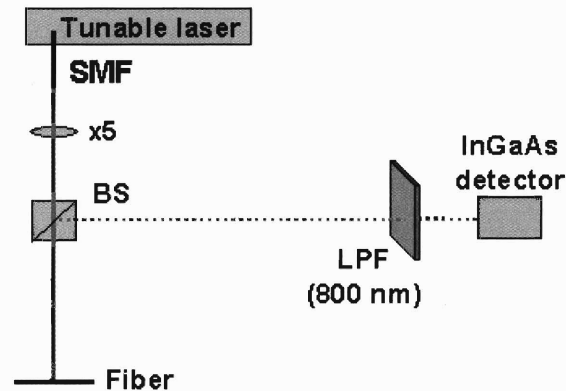


Figure 30: Experimental set-up for narrow-band reflectivity (NBR) measurements. The source is ~ 25 cm away from the fiber and the detector ~ 1.5 m away from the beam-splitter (BS). We sometimes use a low-pass filter (LPF) that cuts all wavelengths below 800 nm.

The collimated beam is sent on the fiber at normal incidence and a beam-splitter is used to direct half of the reflected beam to a (Newport 818IG) InGaAs detector placed 1.5 m away from the fiber, corresponding to an effective collection angular range $< 0.01^\circ$.

V.2 Mechanical tuning

As seen in Fig.29, we have successfully fabricated and characterized Fabry-Perot fibers and observed a significant decrease of their reflectivity in the vicinity of their

cavity resonant wavelength.³⁹ This sharp decrease in reflectivity over a narrow bandwidth opens the possibility of widely tuning the reflection coefficient of these fibers at a fixed wavelength by inducing even a small spectral shift of the Fabry-Perot resonant mode. In particular, applying an axial strain to the fiber ends should result in a displacement of the interfaces within the multilayer structure, and therefore a change in the resonance condition (section II.2.3). This appears to be a promising strategy since our fibers are made of amorphous materials, more than 98% of which is polymer (by volume). Surrounding a fiber with such a structure yields cost-effective tunable optical filters that could lead to applications such as optical switches for wavelength-division-multiplexing (WDM) systems and sensors.

The opto-mechanical tuning of dielectric Bragg reflectors has been widely studied and it is convenient for comparison to express these results in terms of the *normalized shift* defined as the ratio of the induced spectral shift $\Delta\lambda$ and the operating wavelength λ or $\Delta\lambda/\lambda$. Kimura et. al. reported a normalized reversible shift of 3.4% under a load of 18 kg/mm² applied perpendicularly to an all-polymer multilayer reflector made of alternating layers of polystyrene and polyvinyl alcohol.⁴⁰ Fiber Bragg Gratings (FBGs) have been tuned mechanically using piezoelectric transducers (PZTs) to generate strains perpendicular to the grating leading to normalized shifts as high as 2.9% under 1,000 V.⁴¹ A normalized shift of 0.64% under 50 V is stated to be the highest tuning efficiency reported to date for tunable FBG filters using PZTs.⁴² In the next section, we develop a simple model to assess the performance of our Fabry-Perot fibers by calculating the theoretical relation between the applied axial strain and the normalized shift of their Fabry-Perot resonant mode in the limit of the elastic regime.

V.2.1 Opto-mechanical behavior of Fabry-Perot fibers

Neglecting possible strain-induced refractive index variations, it can be derived from Eq.1 that the normalized shift of the center wavelength of the fundamental photonic band-gap is in a first approximation proportional to the radial strains:

$$\frac{\Delta\lambda}{\lambda} = \frac{n_1 d_1^0 \varepsilon_r^{(1)} + n_2 d_2^0 \varepsilon_r^{(2)}}{n_1 d_1^0 + n_2 d_2^0} \quad (76)$$

where $\varepsilon_{rr}^{(1)}$, $\varepsilon_{rr}^{(2)}$ are the radial strains, n_1 , n_2 the refractive indices and d_1^0 , d_2^0 the thicknesses of the unstrained high and low refractive index layers, respectively. This derivation implicitly assumes that all the layers made of the same material undergo the same deformation, their radial strain being uniquely related to the applied axial stress by the Poisson ratio of the material, as for a free annulus. However, the difference between the Poisson ratio of the high and low refractive index materials and the adhesion condition at each layer interface result in non-uniform radial stress and radial strain distributions, making this approach very approximate. In order to accurately relate the normalized shift of the cavity resonant mode to the applied axial strain, we need to calculate the radial displacement profile in the fiber cross-section $u_r(r)$ in order to determine the displacement of the cavity layer interfaces.

We model our fibers as a perfectly concentric multilayer structure consisting of N layers ($N+1$ interfaces) surrounded by two supporting media (air, 0 and the polymer core, $N+1$), as shown in Fig.31.

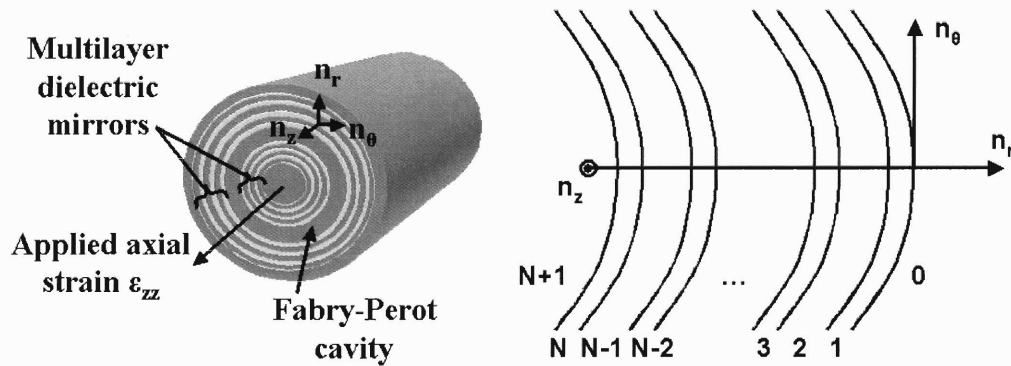


Figure 31: Schematic of the fiber structure.

Starting from Newton's Law for the stress components expressed in a cylindrical coordinate system:

$$\frac{\partial \sigma_{rr}}{\partial r} + \frac{\sigma_{rr} - \sigma_{\varphi\varphi}}{r} + \frac{1}{r} \frac{\partial \sigma_{r\varphi}}{\partial \varphi} + \frac{\partial \sigma_{rz}}{\partial z} = \rho \ddot{u}_r \quad (77)$$

$$\frac{\partial \sigma_{r\varphi}}{\partial r} + 2 \frac{\sigma_{r\varphi}}{r} + \frac{1}{r} \frac{\partial \sigma_{\varphi\varphi}}{\partial \varphi} + \frac{\partial \sigma_{z\varphi}}{\partial z} = \rho \ddot{u}_\varphi \quad (78)$$

$$\frac{\partial \sigma_{rz}}{\partial r} + \frac{\sigma_{rz}}{r} + \frac{1}{r} \frac{\partial \sigma_{\varphi z}}{\partial \varphi} + \frac{\partial \sigma_{zz}}{\partial z} = \rho \ddot{u}_z \quad (79)$$

where ρ is the density of the material, and assuming that:

- the principal axes of the system coincide with those of this coordinate system:

$$\sigma_{r\varphi} = \sigma_{rz} = \sigma_{\varphi z} = 0 \quad (80)$$

- the stress is circular symmetric and axially uniform (no φ or z dependence)

- the system is at equilibrium

we obtain the following non-trivial equation:

$$\frac{\partial \sigma_{rr}}{\partial r} + \frac{\sigma_{rr} - \sigma_{\varphi\varphi}}{r} = 0. \quad (81)$$

We now need to transform the variables in this equation into the radial displacement variable u_r . We first substitute the strain components for the stress components using Lamé's equations:

$$\sigma_{rr} = \eta[\varepsilon_{rr} + \varepsilon_{\varphi\varphi} + \varepsilon_{zz}] + 2G\varepsilon_{rr} \quad (82)$$

$$\sigma_{\varphi\varphi} = \eta[\varepsilon_{rr} + \varepsilon_{\varphi\varphi} + \varepsilon_{zz}] + 2G\varepsilon_{\varphi\varphi} \quad (83)$$

where G is the shear modulus and η the Lamé modulus (usually denoted λ), so that the equilibrium condition becomes:

$$(\eta + 2G) \frac{\partial \varepsilon_{rr}}{\partial r} + \eta \frac{\partial \varepsilon_{rr}}{\partial r} + \eta \frac{\partial \varepsilon_{rr}}{\partial r} + \frac{2G}{r} (\varepsilon_{rr} - \varepsilon_{\varphi\varphi}) = 0 \quad (84)$$

Next, using the definition of the principle strain components in terms of the radial displacement, $\varepsilon_{rr} = \frac{\partial u_r}{\partial r} = \frac{du_r}{dr}$, $\varepsilon_{\varphi\varphi} = \frac{u_r}{r}$, $\varepsilon_{zz} = \frac{\partial u_z}{\partial z} = \frac{du_z}{dz}$, we reach the following equation for the equilibrium condition:

$$\frac{d^2 u_r}{dr^2} + \frac{1}{r} \frac{du_r}{dr} - \frac{u_r}{r^2} = 0 \quad (85)$$

whose solutions are of the form:

$$u_r = \frac{A}{r} + Br \quad (86).$$

The j^{th} layer is characterized by two known material parameters G_j and η_j , and the displacement in this layer by two unknown constants A_j and B_j , leading to a total of $2N+4$ unknown constants for the whole structure. These constants are determined through imposing the continuity of u_r and σ_{rr} at the interfaces. These continuity conditions imply the following inhomogeneous linear transformation between the A_j and B_j coefficients in any two adjacent layers:

$$\begin{pmatrix} A_j \\ B_j \end{pmatrix} = \mathbf{M}^j \begin{pmatrix} A_{j-1} \\ B_{j-1} \end{pmatrix} + \varepsilon_{zz} \begin{pmatrix} H_1^j \\ H_2^j \end{pmatrix} \quad (87).$$

where the linear transformation $\mathbf{M}^j = \begin{pmatrix} M_{11}^j & M_{12}^j \\ M_{21}^j & M_{22}^j \end{pmatrix}$ for the j^{th} interface has the components:

$$M_{11}^j = \frac{\eta_j + G_j + G_{j-1}}{\eta_j + 2G_j} \quad (88)$$

$$M_{12}^j = \frac{\eta_j + G_j - \eta_{j-1} - G_{j-1}}{\eta_j + 2G_j} \quad (89)$$

$$M_{21}^j = \frac{1 - M_{11}^j}{d_j^2} \quad (90)$$

$$M_{22}^j = 1 - \frac{M_{12}^j}{d_j^2} \quad (91)$$

$$H_1^j = \frac{\eta^j - \eta^{j-1}}{2} d_j^2 \quad (92)$$

$$H_2^j = -\frac{H_1^j}{d_j^2} = \frac{\eta^j - \eta^{j-1}}{2} \quad (93).$$

This results in $2N+2$ linearly independent equations relating the unknown constants, and two more conditions are obtained by requiring that σ_{rr} vanishes at the inner and outer free surfaces (d_0 and d_{N+1}). We therefore obtain a unique solution for this system where all the unknown constants are obtained in terms of the material parameters and the axial

strain ε_{zz} . The resulting radial stress and radial displacement profiles in the multilayer structure are shown in Fig.32 for an applied axial strain $\varepsilon_{zz}=1\%$.

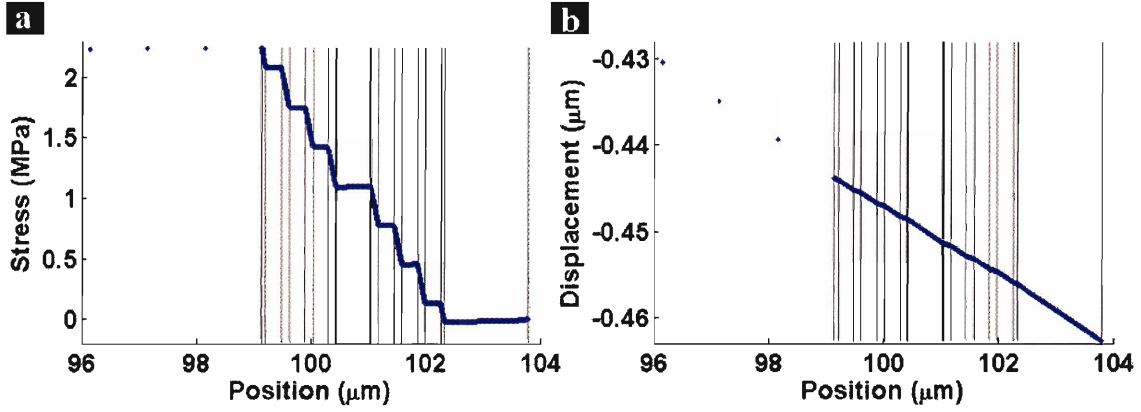


Figure 32: Calculation of the radial stress (a) and radial displacement (b) distributions as a function of position in the radial direction for an applied axial strain $\varepsilon_{zz}=1\%$. The outer most layer (right) is the thick protective polymer layer while the left side of the structure corresponds to the polymer core.

The non-uniform radial displacement of the bilayer interfaces leads to a shift in the band-gap of the multilayer structure, while the difference in the displacement of the cavity layer interfaces leads to a shift in its resonance wavelength. Because of the linearity of the system, within the assumed approximations, one can obtain the following relationship between the normalized shift of the resonance wavelength and ε_{zz} in the elastic regime:

$$\frac{\Delta\lambda}{\lambda} = -0.373\varepsilon_{zz} \quad (94)$$

where the proportionality constant is related to the detailed structure of the fiber. When comparing our results with the values reported previously for the mechanical tuning of Bragg reflectors and FBGs, it must be kept in mind that here the stress is applied in the plane of the layers (and not perpendicularly to them), which greatly penalizes the amplitude of the radial displacement.

The fibers' Young's modulus (E_{fiber}) can be approximated by modeling their multilayer structure as N independent parallel springs and assuming that the applied axial strain is equal for all the layers. Since the fibers are typically made of only two distinct

materials, let's denote by E_1 , E_2 the Young's modulus and N_1 , N_2 the total the number of high and low refractive index layers, respectively. Then, we have:

$$E_{\text{fiber}} = \left(E_1 \cdot \sum_{i=1}^{N_1} A_i^1 + E_2 \cdot \sum_{j=1}^{N_2} A_j^2 \right) / A \quad (95)$$

where A_i^1 , A_j^2 are the cross sectional-areas of the i^{th} high and j^{th} low refractive index layers, respectively and A is the total cross-sectional area of the fiber. This calculation leads to a Young's modulus of 2.64 GPa for a Fabry-Perot fibers made of PES and As_2Se_3 containing a half-wavelength low refractive index optical cavity (using $E_{\text{PES}} = 2.4$ GPa for the bulk and $E_{\text{As}_2\text{Se}_3} = 15$ GPa reported for 1.5- μm thick films).^{37,43}

V.2.2 Mechanical tuning experiment

The fibers described in this section are composed of a hollow-core polymer rod surrounded by 6 bilayers of As_2Se_3 and PES, separated in the middle by an extra PES layer, which forms a low-index Fabry-Perot cavity. An extra polymer layer protects the fiber surface. SEM imaging of fiber cross sections reveals a glass layer thickness of ~ 135 nm (250 m), except for the first and the last layers that are half as thick, a polymer layer thickness of ~ 270 nm (540 nm), and a defect layer thickness of ~ 610 nm (1,170 nm) for 240- μm (460- μm) diameter fibers. The SEM micrographs and reflectivity spectra of these fibers are shown in Fig.29.

Two different band-gap positions have been studied with a (Nicolet Magna 860) FTIR spectrometer coupled to a (Nicolet SpectraTech NicPlan) infrared microscope: 1.7 microns and 3.2 microns corresponding to the 240-micron and 460-micron diameter fiber respectively. Measurements were performed on 30-cm long fiber samples fixed at one end with epoxy to a (Transducer Techniques MDB-2.5) load cell and at the other end with strong tape to a pole mounted on a (Newport PR50) stepper rotational stage. This end was also wrapped around a screw mounted on the pole to further secure it in place [Fig.33].

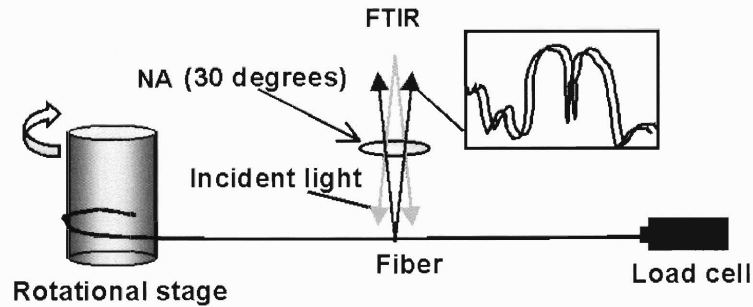


Figure 33: Experimental set-up for the mechanical tuning demonstration.

The diameter of the pole was equal to 2.1 cm and the rotational stage had a precision of 0.1° , leading to a theoretical strain precision far below the experimental one. The precision of the load cell was equal to 1 mg, corresponding to an uncertainty lower than 30 MPa on the Young's modulus. The whole setup was placed on the motorized stage of the FTIR microscope, which had a $1\text{-}\mu\text{m}$ resolution. All reflectivity measurements were normalized to a background taken with a flat gold mirror and were performed at a fixed position on the tested fiber to avoid measuring variations in the cavity resonant wavelength arising from its angular dependence and/or from outer diameter fluctuations. The actual induced axial strain near the reference position was measured using a second reference point, both chosen far from the fixed ends of the fiber where edge-effects induce non-uniform stress and strain distributions.

V.2.3 Results and interpretation

The FTIR reflectivity spectra exhibit a clear resonant mode in the fundamental band-gap of both the 240-micron and the 460-micron diameter fiber with a quality factor $Q \sim 31$ [Fig.29]. Fig.34 shows the results of tuning the corresponding Fabry-Perot resonant modes under increasing axial strain.

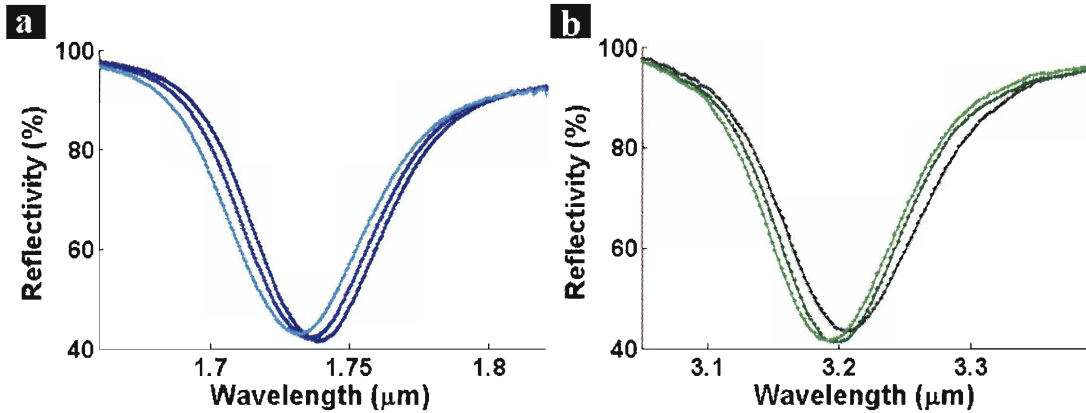


Figure 34: Mechanical tuning of the cavity resonant wavelength of the 240- μm (a) and 460- μm (b) diameter fibers under three applied axial strains: $\varepsilon_{zz}=0.23\%$ (right), $\varepsilon_{zz}=0.61\%$ (middle) and $\varepsilon_{zz}=1.22\%$ (left).

When the axial strain applied to the 240- μm -diameter fiber is increased from 0.23% to 1.07%, the reflectivity at 1.71 μm drops by 13%. The experimental normalized-shift versus axial strain curves are reported in Fig.35a and appear to be linear for both fibers up to approximately 1.2%, which is the limit of the reversible elastic regime and corresponds to small applied loads: 76 g and 300 g for the 240-micron and 460-micron diameter fiber, respectively.

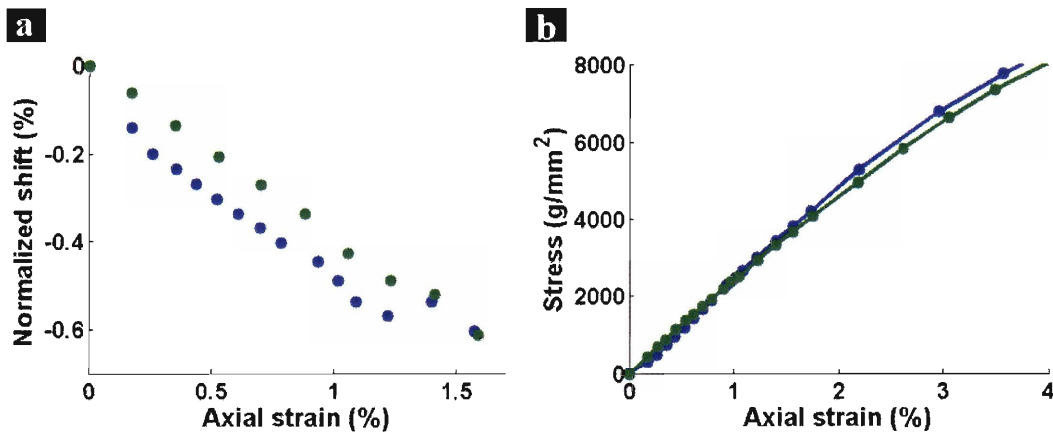


Figure 35: Normalized shift of the cavity resonant wavelength (a) and axial stress (b) versus axial strain for the 240-micron (blue) and 460-micron (green) diameter fiber.

Under higher applied strains, the normalized-shift becomes non-linear, indicating possible plastic deformation, relaxation and/or layer delamination. Indeed, our opto-

mechanical model predicts that all the layers except the outer protective polymer layer are under tensile radial stress whose maximum is located at the interface between the layers and the polymer core where delamination is most likely to occur [Fig.32]. In the linear regime, the normalized-shift versus axial strain curves exhibit a slope equal to -0.385 and -0.384 for the 240-micron and the 460-micron diameter fiber, respectively, in close correspondence to the predicted value (-0.373). This corresponds to a maximum reversible normalized shift $\Delta\lambda/\lambda$ equal to -0.462%, which compares well with other systems mentioned earlier. The stress-strain curves shown in Fig.35b also exhibit an elastic regime up to 1.2% axial strain with a corresponding Young's modulus equal to 2.59 GPa and to 2.39 GPa for the 240-micron and the 460-micron diameter fiber, respectively. These values are slightly lower than the predicted value of 2.64 GPa, due to expected relaxation effects in these fairly low T_g materials.

The tuning efficiency demonstrated here is limited primarily by the low Q factor measured in these Fabry-Perot fibers while the amplitude of the reversible shift is limited by the elastic regime of the materials and by possible layer delamination. The Q factor can be systematically increased by reducing the range of collection angles (e.g. using NBR measurements) and by increasing the number of bilayers surrounding the cavity layer: a similar structure with only 4 additional bilayers would achieve a computed reversible reflectivity drop from 99% to less than 1% at normal incidence. This dramatic increase in sensitivity would make these fibers very useful as sensors and optical switches.

V.2.4 Dynamic mechanical tuning

Based on these promising results, we have studied the dynamic response of higher Q factor Fabry-Perot fibers under low frequency modulation of the applied axial strain. We used a 17-cm long fiber surrounded by a Bragg mirror consisting of 8 bilayers of As_2S_3 and PEI separated in the middle by low-index Fabry-Perot cavity. Reflectivity measurements were performed with the NBR measurement set-up to eliminate the angular averaging induced by the FTIR microscope lens. The fiber was attached at one

end to a (Newport PR50) stepper rotational stage while the other end was fixed with epoxy [Fig.36].

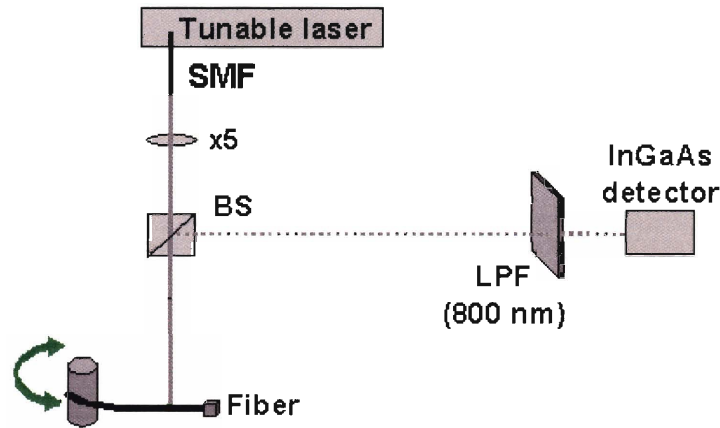


Figure 36: Experimental set-up for the demonstration of dynamic mechanical tuning.

The measured cavity resonant mode is shown in Fig.37a and exhibits a quality factor equal to 105.

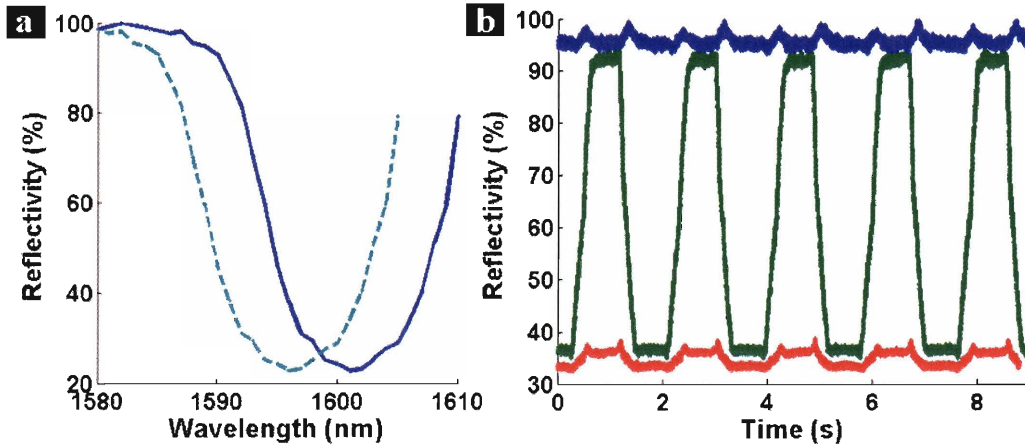


Figure 37: **a** Measured cavity resonant mode under 0% (continuous line) and 0.8% (dashed line) applied strain, **b** modulation of the reflected power at three different probe wavelengths: 1560 nm (blue), 1592 nm (green) and 1600 nm (red), normalized by the maximum reflected power at 1560 nm.

To study the dynamic response of the fiber, we have modulated the applied axial strain from 0.2% to 1%, corresponding to a maximum shift of -5 nm. The minimum applied axial strain was chosen to be non-zero to minimize vibrations of the fiber during

the measurements. The power reflected by the fiber was measured at three different probe wavelengths and is shown in Fig.37b. It appears that off resonance (1560 nm), the reflected power is high and fairly constant, which indicates that the fiber did not move significantly with respect to the probe beam during the measurement. In contrast, we observe a strong modulation of the reflected power at the edge of the cavity resonance (1592 nm), which is a clear indication that the induced shift was fully reversible and that the range of applied axial strains was within the elastic regime of the materials. The reflectivity, calculated as the reflected power normalized by the maximum reflected power at 1560 nm, varied from 93% to 37%, which is consistent with a -5 -nm shift of the cavity resonant mode [Fig.37a]. The measured average rise or fall time was equal to 270 ms and was limited only by the acceleration of the stepper rotational motor. Similarly, the shape of the modulation was primarily dictated by the characteristics of the stepper rotational stage, the flat regions corresponding to the time necessary for the motor to decelerate and reverse its motion.

These results confirm that a fully reversible -5 nm shift of the Fabry-Perot resonant mode can be induced in our reflection fibers using the proposed mechanical tuning scheme, corresponding to a decrease of the fiber reflectivity at fixed wavelength by more than 50%. The optical response of such fibers under high-frequency strain modulations could be studied using piezoelectric crystals and acoustic waves. However, because the amplitude of the induced strain modulation would be much lower than 1%, high tuning efficiency would require to increase the Q factor of the fibers, at least by an order of magnitude.

V.3 Optical tuning

Mechanical tuning provides a low energy mechanism to tune the response of Fabry-Perot fibers over a large spectral range. However, it requires to sacrifice the flexibility of the fibers and its implementation in certain applications such as light sensing, low form-factor optical switches... can be unpractical or irrelevant. An alternative approach to tuning the optical resonance of the Fabry-Perot multilayer structure enveloping the fibers is through optical modulation of its cavity material

refractive index.⁴⁴ The fibers in this section contain micro-cavities made of a chalcogenide glass (As_2Se_3) that exhibits a reversible *photodarkening effect*. This effect, induced under illumination with near band-gap laser radiation, consists in a transient increase of the glass absorption coefficient (k) consistent with an increase in its refractive index (n) as predicted by the Kramers-Kronig relations. We first review the theoretical models proposed to describe the photodarkening effect, then characterize this effect in thin film samples before proceeding to examine the properties of fiber-based resonators incorporating such films.

V.3.1 Introduction to chalcogenide glasses and the photodarkening effect

It was first reported nearly 30 years ago that photostructural changes in chalcogenide glasses are induced by illumination with near band-gap light⁴⁵ and can be observed in well-annealed amorphous thin films.⁴⁶ This effect has been shown to be accompanied by changes in the structural properties (volume expansion⁴⁶ -thickness increase by $\sim 5\%$ -⁴⁷ photo-amorphization,⁴⁸ decrease of the glass transition temperature⁴⁹ and decrease of the microhardness⁵⁰), in the optical properties (increase -photodarkening-⁵¹ or decrease -photobleaching-⁵² of the refractive index, birefringence⁵³) and in the transport properties (conductivity⁵⁴, diffusivity⁵⁵). There are two distinct contributions to these changes: a *metastable part* and a *transient part*. The metastable effect is often described as a *reversible* effect because the initial state can be completely recovered after illumination by annealing near the glass transition temperature⁵² or, in some glasses, partially by exposure to sub-band-gap light (e.g. in As_2S_3 : photodarkening at 488 nm and photobleaching at 647.1 nm⁵²), while the transient effect completely disappears after illumination even at room temperature. Since the two chalcogenide glasses that we have used in this work, As_2S_3 and As_2Se_3 , both exhibit photodarkening, we will focus on this effect in the rest of this section.

Before jumping into a description of the physical phenomena underlying the photodarkening effect and its characteristics, let's first review the atomic and electronic structure of As_2Se_3 as a case example of chalcogenide glasses. The network structure of

As_2Se_3 consists of a linkage of pyramidal units formed by the twofold coordinated Se chalcogen atoms and the threefold coordinated As pnictogen atoms [Fig.38].

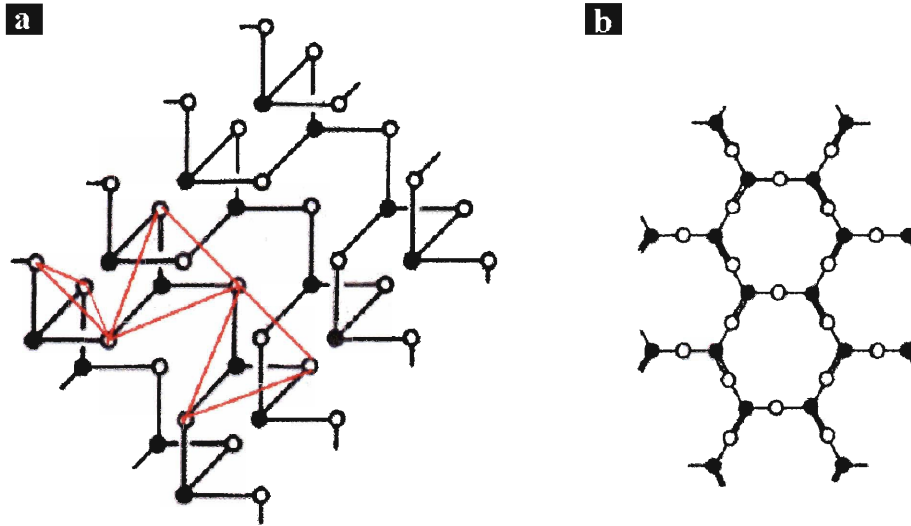


Figure 38: Atomic structure of an As_2Se_3 layer, solid circles are As, open circles are Se. **a** shows the AsSe_3 pyramidal units, **b** shows the σ bonds in the plane of the layer. (Courtesy of Prof. J. Joannopoulos)

These chains of AsSe_3 pyramids are bonded by Van Der Waals type intermolecular interactions.⁵⁶ The twofold coordination of the Se atoms introduces a high degree of flexibility in the network structure and leaves lone-pair electrons in non-bonding orbitals, which are responsible for structural correlations through intermediate range interactions ($\sim 7 \text{ \AA}$).^{52,56} While this contributes to some structural ordering, the amorphous phase is nevertheless characterized by a substantial degree of disorder (broad bond angle and bond length distributions), resulting from the presence of homopolar (e.g. As-As) and dangling bonds.

The electronic structure of As_2Se_3 is characteristic of amorphous semiconductors [Fig.39a].

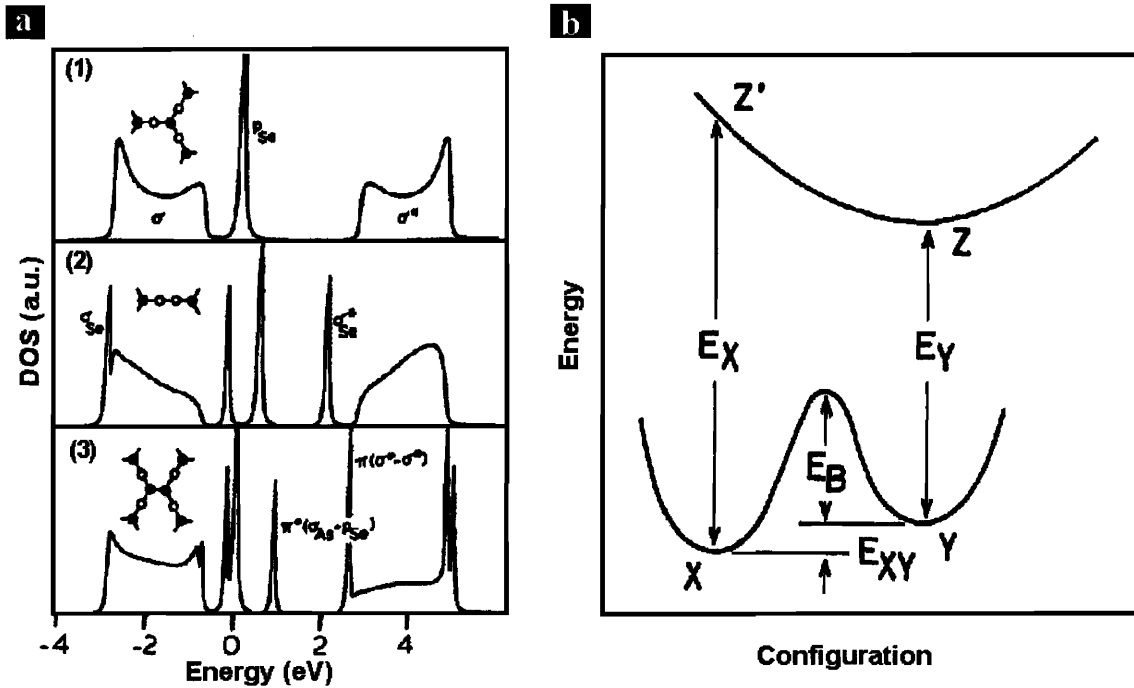


Figure 39: **a** Electronic band structure of As_2Se_3 for the defect free glass (top) and when homopolar bonds are present (middle Se-Se, bottom As-As), **b** relative energies of the annealed, excited and photodarkened states. (Courtesy of Prof. J. Joannopoulos)

The lower lying states in the valence band are σ bonding states associated with covalent bonds in the network while the anti-bonding σ^* states form the conduction band.⁵⁷ The top of the valence band is comprised of π lone-pair states associated with the interacting non-bonding chalcogen orbitals P_{Se} . In addition, the presence of Se-Se and As-As homopolar bonds leads to σ_{Se-Se} and σ^*_{Se-Se} orbitals while the σ_{As-As} orbitals interact with neighboring π -orbitals from chalcogen atoms to form $\pi^*(\sigma_{As}-P_{Se})$ states that lay just above the π band as shown in Fig.39a.⁵⁸

It is widely accepted that photodarkening results primarily from an increase in the interaction of chalcogen lone-pair electrons, resulting in a broadening of the valence band and consequently in a reduction of the band-gap energy,⁵⁹ even though photo-induced creation and/or modification of localized defect states may also play a role. It follows that photodarkening is strongly determined by the type of the chalcogen atom more than a particular structure of the glass.⁴⁶ In a very simplistic picture, the annealed ground state of the glass can be described as an asymmetric double well adiabatic potential and the

excited state as a single well [Fig.39b].⁶⁰ Under band-gap illumination, sites in the annealed sample efficiently transition from the ground state X to the excited state Z and relax either to the metastable photodarkened state Y or to the ground state. The number of photodarkened sites increases until photo- and thermo-induced transitions from the metastable photodarkened state Y to the ground state X (bleaching) become as important as photodarkening itself and a steady-state is reached. When the illumination is turned off, thermo-bleaching leads to a decrease of the photodarkening in time (transient effect) until the probability of relaxing from Y to X vanishes (metastable effect). It has been reported that the amplitude of the metastable photodarkening at saturation has a strong temperature dependence and increases steeply down to about 80 K,⁶¹ indicating a quenching of the thermo-bleaching effect and/or an increase in the barrier energy E_B . At room temperature, it appears to be independent of the intensity of the excitation light but higher photon flux induce faster photodarkening.⁶² Values as high as 1.6%,⁵², 2%,⁵¹ 3.4%,⁶³ or 3.7%⁴⁵ refractive index change have been reported in As_2S_3 and As_2Se_3 amorphous thin films at room temperature, more than one order of magnitude larger than the index change typically achieved in silica fibers.

To this day, several models have been proposed and developed to describe the physical mechanisms behind the photodarkening effect but there exists no unified theory that would provide a complete and coherent description of all the photo-induced effects in chalcogenide glasses. Let's now review three of the most promising models to gain insight into the macroscopic and microscopic mechanisms responsible for the photodarkening effect.

V.3.2 Three leading models to describe the photodarkening effect

One of the first models describing the physics of the photodarkening effect was proposed by Tanaka and is called the **bond-twisting model**.⁶⁰ In this model, photodarkening results from the formation of structural defects in the well-annealed glass structure. The local structure in the well-annealed ground state is assumed to be similar to the low energy crystal structure. Under near band-gap illumination, lone-pair electrons

from the chalcogen atoms are excited to the conduction band resulting in excitons consisting of a delocalized electron and a positively charged defect center [Fig.40a-b].

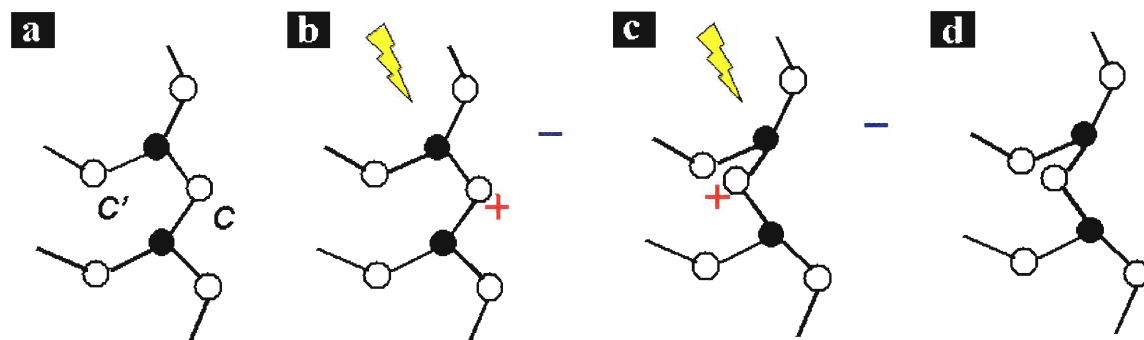


Figure 40: **a** Atomic structure in the ground state, **b** formation of an exciton under illumination, **c** bond twisting induced by Coulombic interactions, **d** photodarkened structure.

As a result, the intermolecular interaction between the positively charged chalcogen atom C and its nearest atom C' changes from Van Der Waals to stronger Coulombic type. It is estimated that the corresponding Coulomb energy (~ 0.25 to 1 eV) is sufficient to overcome the distortion energy of intramolecular covalent bonding (~ 0.05 eV).⁶⁰ Therefore the twisting motion of the positively charged chalcogen atom C to its lower energy conjugated position becomes possible [Fig.40c]. These structural defects in turn result in an increase of the interaction between lone-pair electrons, leading to a broadening of the valence band to higher energy compare to the ground state and to the photodarkening effect. It is estimated that photodarkening at saturation corresponds to a change in only 1% of the available sites.⁶⁴ One explanation could be that the creation of new photodarkened sites in the vicinity of already existing photodarkened sites is inhibited by changes in the network structure. When the illumination is turned off, the excited free charge carriers recombine with the positively charged chalcogen atoms and the twisted structure becomes frozen-in [Fig.40d]. Relaxation to the ground state is possible by thermal annealing.

The bond-twisting model provides explanations to various experimental observations:

- The amplitude of the photodarkening increases when the sample is under low applied pressure but decreases under high applied pressure.⁵² The low pressure enhancement could result from stronger intermolecular interactions and therefore higher Coulomb energy values while high pressure could quench the photodarkening effect by reducing the amount of free space required for the bond-twisting mechanism to occur.
- The amplitude of the photodarkening increases when the size of the chalcogen atoms decreases (Te, Se, S in that order).⁴⁶ This dependence could indicate a strong correlation between the size of the chalcogen atoms and the amount of intermolecular space available for the bond-twisting motions.

The bond-twisting model however does not provide an explanation for other photo-induced structural changes typically associated with photodarkening, such as volume expansion. In addition, it is entirely based on local atomic relaxations occurring around particular chalcogen atoms while photodarkening and photo-expansion are clearly non-local effects. Shimakawa⁶⁵ suggested that rather macroscopic or mesoscopic interactions are the dominant mechanism in both the photodarkening and the volume expansion effects. In other words, the entire π -band at the top of the valence band should be regarded as being responsible for photodarkening or volume expansion, and not individual atoms. This is the motivation behind **the slip and repulsion model**.

The slip and repulsion model is based on the assumptions that the structure of chalcogenide glasses consists of an assembly of layered clusters and that holes have a higher mobility than electrons in these glasses, which is generally true.⁶⁵ Under illumination, excitons form and dissociate generating electrons in the conduction band tail and holes in the π -band. The photoexcited electrons remain mostly trapped in localized states, while the photoexcited holes are nearly free and diffuse to the unilluminated region. As a result, the layers in the illuminated region become negatively charged giving rise to repulsive Coulomb interactions that lead to an increase in the average interlayer distance [Fig.41a].

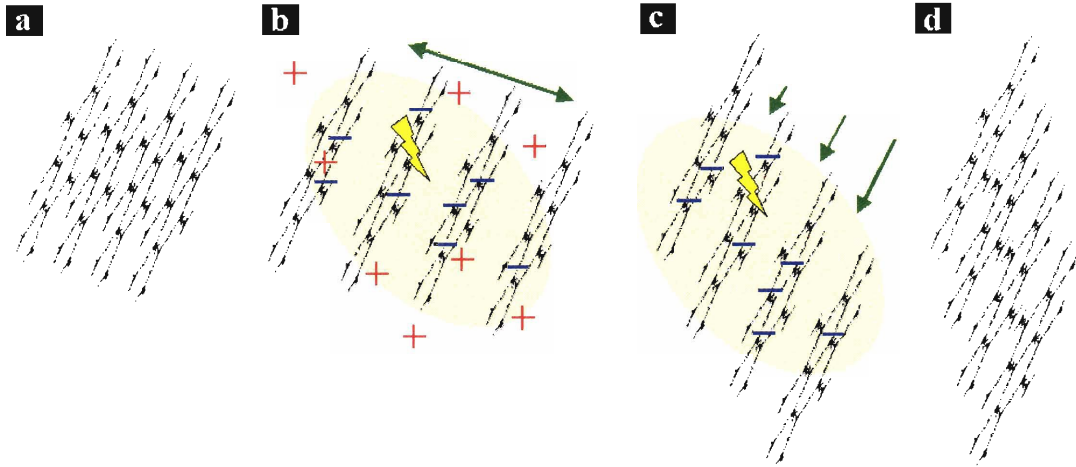


Figure 41: **a** Atomic structure of a layer cluster in the annealed state, **b** formation and dissociation of excitons under illumination resulting in a Coulombic repulsive force between the layers, **c** slip motion of the layers with respect to each others under the force distribution generated by the photo-expansion of neighboring clusters, **d** atomic structure of the layer cluster in the photodarkened state.

This manifests itself as the photo-expansion effect. The repulsive interactions act as a compressive force on the layers that induces slight modifications of the interaction between lone-pair electrons, but not significantly enough to account for the photodarkening effect. In this model, the photodarkening effect is actually a consequence of the photo-expansion effect. Indeed, since the layers are organized in adjacent clusters of different orientations, a slip motion along the plane of the layers should also take place with the occurrence of volume expansion in neighboring clusters [Fig.41b]. This slip motion of neighboring layers away from their ground state leads to an increase in the lone-pair electron interactions and a broadening of the π -band while the σ^* states of the conduction band remain mostly unchanged. Note that this model, as the bond-twisting model, relies on the fundamental assumption that, although the glass is not in thermal equilibrium, its total free energy in well-annealed samples is minimal and hence the corresponding atomic configurations can be taken to represent the minimum of lone-pair electrons interactions. When the illumination is turned off, the photo-induced charged defects act as recombination centers for the photoexcited free charge carriers. The consequent reduction of the amount of negative charges in the layered clusters leads to a weakening of the repulsive interactions, allowing the layers to slip back toward their

initial position. The layers eventually reach a new metastable position corresponding to the metastable photodarkened state.

While this model does not provide any detailed explanation of the microscopic mechanisms responsible for the modifications of the electronic band structure that ultimately lead to the photodarkening effect, it is nevertheless very insightful and consistent with various experimental observations:

- The characteristic time associated with the decay of the transient photodarkening is relatively long, on the order of seconds.^{47,65} This could be a direct consequence of the invoked relaxation of the layered clusters on a mesoscopic scale, which is expected to require much longer times than the recombination of the photoexcited charges.
- The rate of photodarkening is lower than the rate of photoexpansion.⁴⁶ This could result from the facts that photo-expansion precedes photodarkening in this model and that the energy required for the in-plane slip motion of neighboring layers is expected to be larger than for their repulsion in the normal direction.
- Both photo-expansion and photodarkening are enhanced when the illuminated surface is positively biased.⁴⁶ This could indicate that more electrons accumulate in, and more holes diffuse away from the illuminated region. Conversely, no photo-expansion or photodarkening should occur in very thin films if their full surface area is illuminated since the photoexcited holes would not be able to diffuse away from the illuminated region.⁶⁶
- 0.5 at % of metal impurity (e.g. Sn, Dy) significantly reduces the photodarkening effect.⁶⁷ This could be explained in the light of this model by assuming that these impurities act as bridging atoms between the layers, thus preventing their relative motion.

One model goes deeper in understanding the microscopic mechanisms responsible for the photodarkening effect. It is based on the observations made by Anderson in amorphous materials that phonon coupling can give rise to a negative Hubbard energy U_H ⁶⁸ making the effective interaction between two electrons in the same energy state attractive.⁶⁹ In chalcogenide glasses, Street and Mott⁷⁰ argued that if the atomic motion of the numerous neutral dangling bonds (paramagnetic defect centers) initially present in the

glass is sufficient to induce a negative U_H , then these dangling bonds act as acceptors and donors for the formation of more stable charged dangling bonds with entirely paired spins (diamagnetic defect centers), thus lowering the total energy of the glass. This results in an increase of the glass polarizability and therefore of its refractive index. Kastener et al.⁷¹ further suggested that specific interactions between non-bonding lone-pair orbitals of the chalcogen atoms also provide a mean for decreasing the energy of diamagnetic defects relative to the energy of paramagnetic defects and can give rise to unusual bonding configurations called **Valence Alternation Pairs (VAPs)**. These configurations result for example when a twofold coordinated Se atom and a threefold coordinated As atom in their ground state form one positively charged fourfold coordinated As atom (noted As_4^+ or D^+ in general) and one negatively charged single coordinated Se atom (noted Se_1^- or D^- in general), which is more stable than the neutral $As_4^0Se_1^0$ defect configuration [Fig.42].⁷²

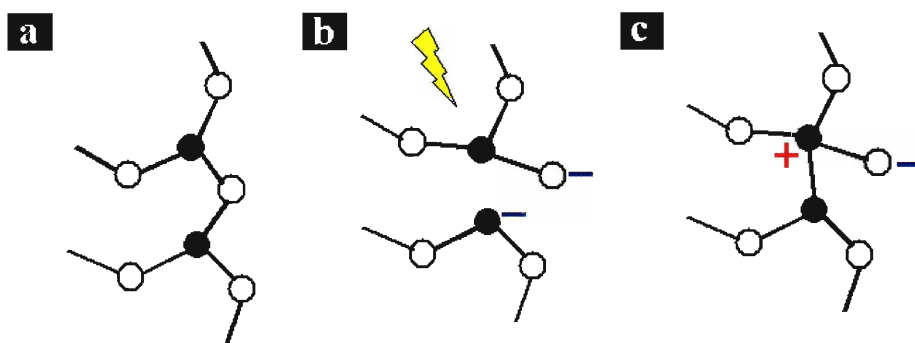


Figure 42: Formation of a VAP. **a** Structure of the annealed glass, **b** breakage of an As-Se heteropolar bond, **c** formation of an As-As homopolar bond and of a stable intimate VAP.

Note that the bonding rearrangements necessary for the creation of an $As_4^+Se_1^-$ VAP entail the formation of an additional As-As bond. The creation of such VAPs requires a relatively small energy so that the intrinsic density of VAPs and As-As homopolar bonds at room temperature is relatively large in most chalcogenide glasses. In materials with large dielectric constant ϵ and high glass transition temperature T_g , the D^+ and D^- centers are mostly randomly distributed while in materials with relatively small ϵ and low T_g , the Coulomb attraction between the D^+ and D^- centers is responsible for a non-random

distribution with an appreciable density of intimate D^+D^- VAPs that can lead to some anisotropy of the glass. Based on this model, photodarkening can be explained as the formation of an excess concentration of VAPs under illumination with sub-band-gap light. Each created D^+D^- dipole is associated with an electric field E_{dip} that produces a local non-linear change of the refractive index Δn :

$$\Delta n \sim \chi^{(3)} E_{dip}^2 \quad (96)$$

$$\text{where } \chi^{(3)} = \frac{4}{3} n_0^2 \epsilon_0 n_2 \quad (97)$$

n_2 is the third order non-linear coefficient of the glass and n_0 the value of its refractive index in the annealed state. The large values of n_2 in chalcogenide glasses ($n_2^{\text{As}_2\text{Se}_3} = 2.6 \cdot 10^{-17} \text{ m}^2/\text{W}$, $n_2^{\text{As}_2\text{S}_3} = 4.5 \cdot 10^{-18} \text{ m}^2/\text{W}$)^{73,74} is the main reason why such a small concentration of dipoles leads to such a pronounced macroscopic Δn . Since these extra VAPs are stable, a fraction of them remains after the illumination is turned off, corresponding to the metastable photodarkened state.

This model is supported by several experimental observations:

- Electron spin resonance (ESR) measurements have shown a large concentration of paramagnetic defect centers in chalcogenide glasses.⁷⁵
- The number of As-As homopolar bonds increases under illumination.⁷⁶
- Chalcogenides glasses that exhibit large photodarkening tend to have large non-linear coefficient.³³

V.3.3 Kinetics of the photodarkening effect

Let's now consider the temporal behavior of the photodarkening effect. Assuming that before illumination there exist N_{GS} sites in the ground state, the number of photodarkened sites $N(t)$ satisfies the following rate equation:

$$\frac{dN(t)}{dt} = k_p (N_{GS} - N(t)) - k_b N(t) \quad (98)$$

where k_p is the photodarkening rate and k_b the bleaching rate. To take into account time-dispersive effects, these rates are expressed as $k_p = At^{\beta-1}$ and $k_b = Bt^{\beta-1}$, where A and B are constants that depend on temperature and illumination intensity, and β is a dispersion

parameter ($0 < \beta < 1$) assumed for simplicity to be the same for both rates. The solution to this equation is a *stretched exponential function* that has the following form:

$$N(t) = N_S \left[1 - \exp \left(- \left(\frac{t}{\tau} \right)^\beta \right) \right] \quad (99)$$

where N_S is the number of photodarkened sites at saturation and $\tau = [\beta / (A + B)]^{1/\beta}$ is a time constant characteristic of the material. The effective medium approximation (EMA) can then be used to calculate the corresponding time evolution of the attenuation coefficient of the glass consisting of a mixture of photodarkened (N) and unphotodarkened ($N_{GS} - N$) sites, which yields:

$$- \Delta\alpha(t) = (\Delta\alpha_{sm} + \Delta\alpha_{tr}) \exp \left[- \left(\frac{t}{\tau_{rise}} \right)^\beta \right] \quad (100) \text{ after illumination is turned on at } t=0;$$

$$- \Delta\alpha(t) = \Delta\alpha_{sm} - \Delta\alpha_{tr} \exp \left[- \left(\frac{t}{\tau_{decay}} \right)^\beta \right] \quad (101) \text{ after illumination is turned off at } t=0;$$

where τ_{rise} is the characteristic rise time of the total photodarkening effect, τ_{decay} is the characteristic decay time of the transient photodarkening, $\Delta\alpha_{sm}$ is the amplitude of the saturated metastable photodarkening and $\Delta\alpha_{tr}$ is the amplitude of the transient photodarkening [see Fig.45a for actual data].

A recent study of the dynamic photo-response of As_2Se_3 thin films under illumination with an Ar^+ laser has confirmed that the total change in absorption $\Delta\alpha$ is a combination of a transient and a metastable part.^{47,77} It showed that the metastable photodarkening accumulated with each successive short time illumination until reaching saturation while further illumination only induced transient photodarkening. The transient effect was found to be as high as 60% of the total effect induced during illumination at room temperature, with a characteristic decay time of ~ 5 s.

V.3.4 Photo-induced refractive index change in As_2Se_3 and As_2S_3 thin films

As discussed in the previous section, photodarkening (heretofore abbreviated as PD) provides a unique mechanism to optically induce a large refractive index change in

chalcogenide glasses. Even though a lot of studies have been carried out on both As_2Se_3 and As_2S_3 , our fibers could represent a very sensitive system for measuring small photo-induced phenomena. Indeed, while the metastable PD has been extensively studied in amorphous chalcogenide thin films using transmission measurements analyzed with the Swanepoel's envelope method⁷⁸ and ellipsometry measurements,^{51,79} little is known about the wavelength and intensity dependence of the amplitude and response time of the transient PD and different models give different predictions. The available experimental data for the transient PD is limited to the transient change in k ,⁸⁰ which is insufficient to accurately predict and optimize the optical tuning efficiency in our fibers at 1.5 μm . Here, we characterize both the metastable and transient PD in As_2S_3 and As_2Se_3 thin films using two approaches. In the first approach we studied the amplitude of the illumination-induced metastable and transient PD through in-situ spectroscopic ellipsometry measurements. The kinetics of the transient PD effect was then studied using a second approach where in-situ transmission measurements were performed with a probe beam at 1.5 μm .

The As_2Se_3 and As_2S_3 thin films were deposited by thermal evaporation under vacuum (2×10^{-5} Torr) and annealed for 2 h under vacuum at 180°C before measurement. The increase in absorption associated with the PD limits the sample thickness for which a uniform and complete metastable PD can be obtained to only a few hundred nanometers,⁶⁴ making thermal evaporation a frequent sample preparation method. The thin films used in the ellipsometry measurements were deposited on a single-side polished silicon substrate while those used in the transmission measurements were deposited on (VWR) glass substrates.

We first studied the wavelength dependence and reproducibility of the metastable PD in a 500-nm thick As_2Se_3 thin film. The sample was subjected to three consecutive cycles consisting of illumination, ellipsometry measurement and annealing [Fig.43a], using two different illumination wavelengths: the 633-nm line from a (NEC GL G5261) HeNe laser and the 514-nm line from a (Coherent Innova 90 plus) Ar^+ laser.

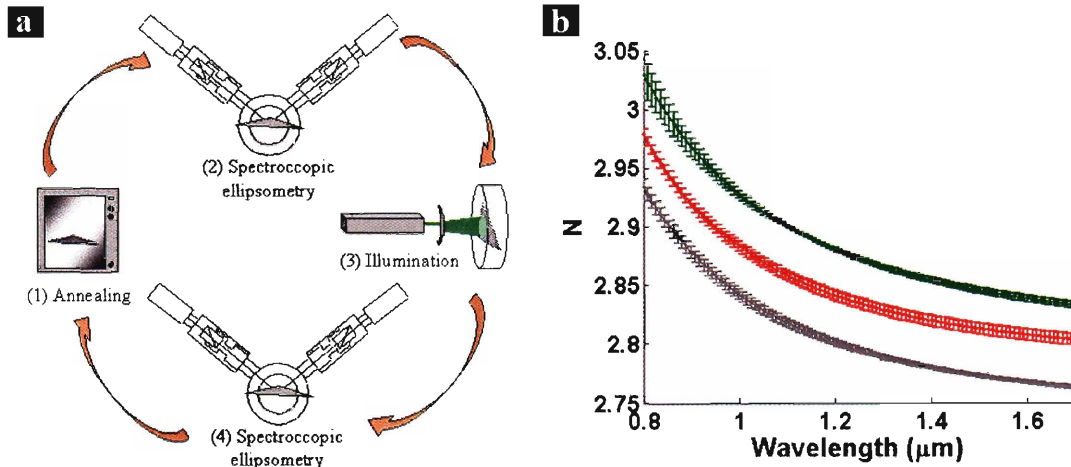


Figure 43: **a** Schematic of the measurement procedure, **b** wavelength dependence and reproducibility of the metastable PD in As_2Se_3 . Grey = annealed state, red = metastable PD induced by 633 nm illumination, green = metastable PD induced by 514 nm illumination.

Illuminations were performed for 2 hours at room temperature in nitrogen atmosphere to prevent photo-oxidation. The illumination power was kept constant for both wavelengths around 100 mW/cm^2 . Ellipsometry measurements were performed using a (Sopra GES-5) broadband spectroscopic ellipsometer. We used focusing lenses to reduce the size of its optical beam to $\sim 200 \mu\text{m} \times 500 \mu\text{m}$ so that no significant thickness or index variations were expected in the measured area. The average n value for the annealed As_2Se_3 thin film was equal to 2.77 at 1.5 μm [Fig.43b]. At this wavelength, we measured a metastable change in n equal to 0.07 (2.6%) and 0.04 (1.4%) under 514 nm and 633 nm illuminations, respectively, which compares well with published data (see section V.3.1). Note that most of the available evidence suggests that the fundamental characteristics of the metastable PD are not affected by variations in the glass structure originating from the sample preparation technique⁴⁶ and that repeated optical darkening and thermal bleaching cycles can be performed with a high degree of reproducibility without leading to noticeable degradation or fatigue.⁵²

We then characterized the intensity dependence of the transient photodarkening effect in 100-nm thick As_2S_3 and As_2Se_3 films under 514-nm illumination by in-situ ellipsometry measurements [Fig.44a].

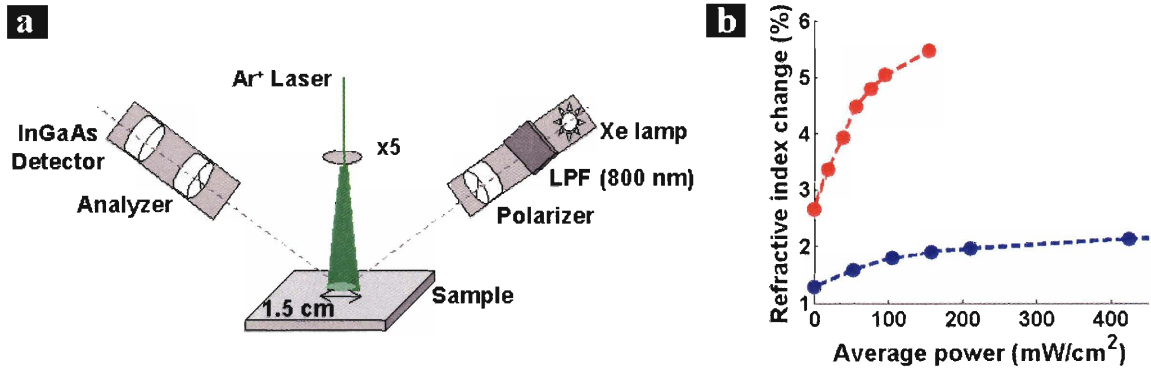


Figure 44: **a** Experimental setup for in-situ ellipsometry measurements. The low pass filter (LPF) cuts all wavelengths below 800 nm. **b** Refractive index change relative to the annealed state under illumination at 514 nm as a function of the average PD power in the layer for As_2S_3 (blue) and As_2Se_3 (red).

The Ar^+ laser beam, heretofore referred to as the *photodarkening beam*, was injected into the ellipsometer after being magnified in order to overlap with the optical beam produced by the ellipsometer and its power was increased between successive measurements. We calculated the axial profile of the PD field in the thin film, using the Transfer Matrix Method (TMM), and determined the average optical intensity in the layer for the different values of incident power. The thin films were initially illuminated with the PD beam for 2h to saturate the metastable PD. The percentage change in the index of refraction at 1.5 μm for the two glasses is reported in Fig.44b as a function of the average intensity in the thin films. The saturated metastable PD (0 intercept) was found to be equal to 2.7% and 1.3% of the annealed refractive index for As_2Se_3 and As_2S_3 , respectively while any additional index change was attributed to transient PD. The transient PD increased linearly with increasing intensity before saturating at $\sim 3.7\%$ and $\sim 1\%$ for As_2Se_3 and As_2S_3 , respectively.

Ellipsometry measurements offer remarkable accuracy but are unfortunately too slow to provide any useful information about the kinetics of the transient PD, which is why we turned to in-situ transmission measurements. The experimental arrangement used to study the kinetics of the transient PD effect in the 100-nm thick As_2S_3 and As_2Se_3 films is depicted in Fig.45a.

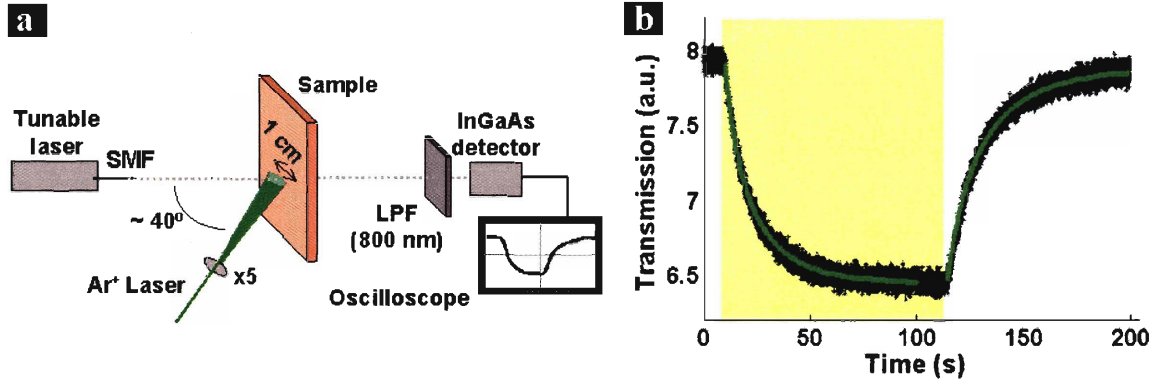


Figure 45: **a** Experimental set-up for in-situ transmission measurements, **b** power transmitted at 1.5 μm over time through a 100-nm thick As_2Se_3 film under and after illumination with the PD beam (dark green) and fit with a stretched exponential function (bright green). The illumination time is shown in yellow.

In this case the PD beam overlapped with the probe beam from a (Photonics Tunics plus) tunable laser emitting 10 mW at 1.5 μm delivered by a single-mode fiber. After saturation of the metastable PD, the transmitted probe beam was recorded in time during and after illumination with the PD beam. A typical example of the transmission is shown in Fig.45b. The intensity dependence of the kinetics of the transient PD was quantified by fitting these transmission profiles recorded for different illumination powers with a stretched exponential function:⁸⁰

$$T(t) = T_0 - \Delta T_{\text{max}} \exp\left(-\left(\frac{t}{\tau}\right)^\beta\right) \quad (102)$$

where T_0 is the initial transmission, ΔT_{max} is the maximum change in transmission, τ is the characteristic rise or decay time and β is a dispersion parameter ($0 < \beta < 1$). On average we obtained $\beta_{\text{As}_2\text{Se}_3} = 0.79$ and $\beta_{\text{As}_2\text{S}_3} = 0.96$. Fig.46 summarizes the intensity dependence of the fitting parameter τ for As_2S_3 and As_2Se_3 .

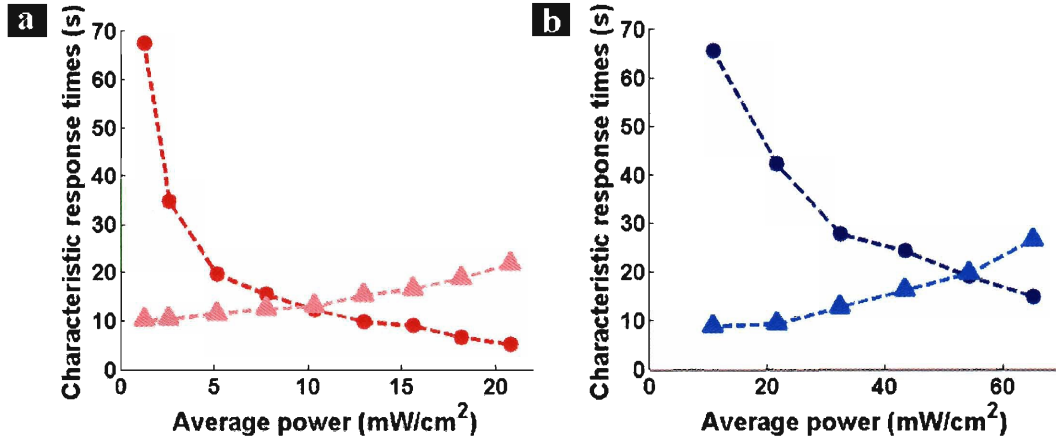


Figure 46: Characteristic rise time τ^{rise} (dots) and decay time τ^{decay} (triangles) associated with the transient PD in As_2Se_3 (a) and As_2S_3 (b) as a function of the average PD power in the layer.

We found that the characteristic rise time decreased with increasing intensity, as expected from section V.3.1, and varied as:

$$\tau_{As_2Se_3}^r = 95I^{-0.95} \text{ (s)} \quad (103)$$

$$\tau_{As_2S_3}^r = 630I^{-0.9} \text{ (s)} \quad (104)$$

where I is the average intensity in the layer (in mW/cm^2). The characteristic decay time after 2 min illumination increased with increasing intensity as:

$$\tau_{As_2Se_3}^d = 9.5e^{0.04I} \text{ (s)} \quad (105)$$

$$\tau_{As_2S_3}^d = 6.6e^{0.02I} \text{ (s)} \quad (106)$$

which, in the light of the slip and repulsion model, suggests that holes diffuse further away from the illumination region.

It clearly appears from these measurements that As_2Se_3 is the best candidate for an optical tuning application due to its larger transient refractive index change and its faster response time under low illumination powers.

V.3.5 Static and dynamic optical tuning

We now report on the fabrication and characterization of all-optical tunable Fabry-Perot fibers. The design of the reflecting Fabry-Perot structure enveloping the fiber had to satisfy two requirements to maximize the tuning efficiency:

- the cavity resonant mode should have a high Q-factor;

- the choice and distribution of the materials should be optimized to maximize the shift of the cavity resonant mode when illuminated with the PD beam.

The solution we implemented consisted in placing As_2Se_3 in the cavity layer because its high absorption coefficient at 514 nm ($k = 0.6047^{17,81}$) resulted in a larger and faster response, while As_2S_3 was used in the numerous surrounding mirror layers since its smaller absorption coefficient at 514 nm ($k = 0.0072^{17,81}$) enabled higher PD light intensity in the cavity layer. Fig.47 shows the cross-section of a 910- μm -diameter fiber composed of a hollow core PEI rod surrounded by 6(inner)+7(outer) bilayers of As_2S_3 and PEI, separated by an As_2Se_3 layer that formed the Fabry-Perot cavity, and protected by two extra polymer layers.

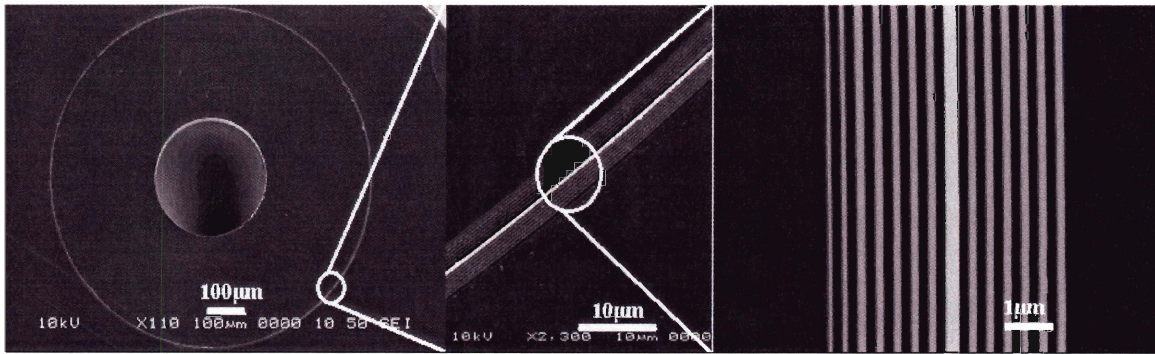


Figure 47: SEM micrographs of an all-optical tunable micro-cavity reflection fiber. The thick middle layer corresponds to the Fabry-Perot cavity made of As_2Se_3 . The other light grey mirror layers are made of As_2S_3 while the dark grey mirror layers are made of PEI.

The As_2S_3 layers were ~ 190 nm thick, the PEI layers were ~ 210 nm thick, and the defect layer was ~ 250 nm thick.

Reflectivity measurements were performed on this fiber using a (Bruker Optics Tensor 37) Fourier Transform Infrared Spectrometer coupled to a (Hyperion 2000 IR) microscope with a lens numerical aperture corresponding to $\pm 35^\circ$ of angular spread. Because of the optical cavity small field of view,⁶ the cavity resonant mode could not be discerned clearly [Fig.48a], and we hence performed narrow-band reflectivity (NBR) measurements as described in section V.1[Fig.48b].

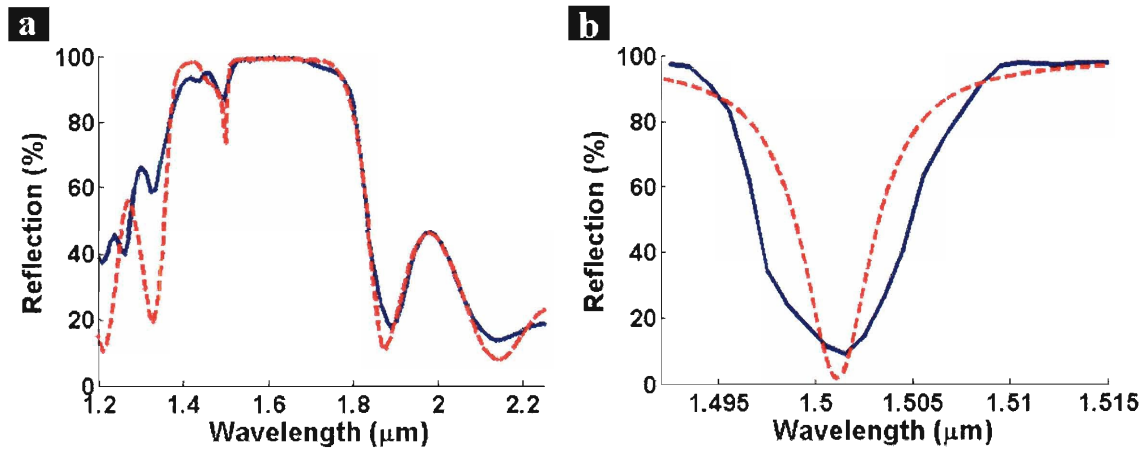


Figure 48: FTIR (a) and NBR (b) measurements. The solid blue curves correspond to experimental results while the dashed red curves are calculated reflectivity spectra averaged over the corresponding experimental range of incidence angles and polarizations.

Using the n and k values of As_2S_3 , As_2Se_3 and PEI measured by spectroscopic ellipsometry and the layer thicknesses determined by SEM imaging, the reflectivity spectra of these fibers were computed with the TMM and averaged over the experimental range of incidence angles and polarizations. While we obtained good agreement with the FTIR measurements [Fig.48a], the NBR measurements exhibited a cavity resonant mode broader and less deep than the calculated one, leading to a quality factor equal to 225, ~35% lower than the theoretical one [Fig.48b]. This indicates the presence of unaccounted material and radiation losses, most likely due to interface defects (roughness, point defects, non-stoichiometric glass composition...) and layer thickness fluctuations that affect the reflectivity of the mirror layers at the resonant wavelength.¹²

We measured the photo-response of these fibers by performing in-situ NBR measurements [Fig.49].

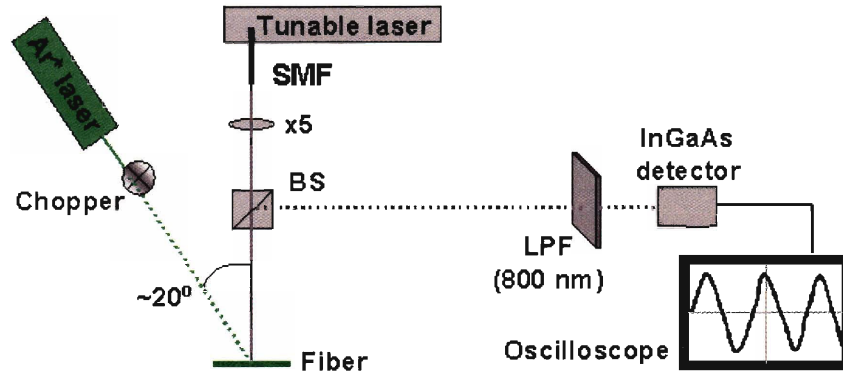


Figure 49: In-situ NBR measurement setup.

The angle of incidence of the PD beam was optimized by calculating the angle of minimum reflection and therefore of maximum penetration of the multilayer structure at 514 nm [Fig.50a].

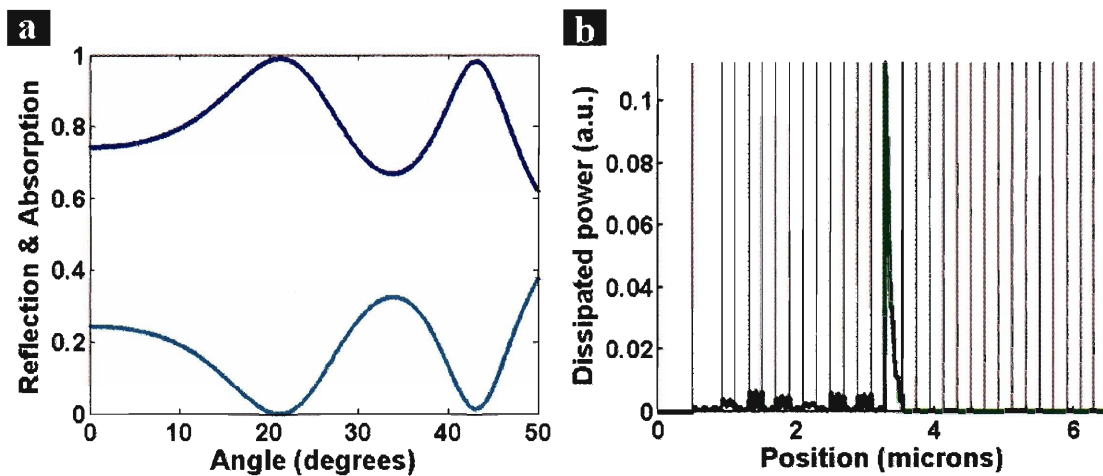


Figure 50: **a** Calculated reflection (light blue) and absorption (dark blue) at 514 nm as a function of incidence angle, **b** calculated power dissipated in the Fabry-Perot structure at 514 nm for an incidence angle of 20° .

This angle appears to be around 20° and also corresponds to the angle of maximum absorption. We confirmed that for this incidence angle is optimal by calculating the corresponding profile of the power dissipated in the structure at 514 nm with the TMM [Fig.50b]. We found that the PD beam is almost entirely absorbed in the cavity layer, thus maximizing its refractive index change and the spectral shift of its resonant mode.

The 910- μm diameter fiber was initially illuminated with the PD beam for 2h to ensure saturation of the metastable PD. The reflected power before and during subsequent illumination with the PD beam was then measured at each probe wavelength with illumination and dark times equal to 2 min and normalized by the power reflected off-resonance at 1550 nm. We measured a photo-induced shift of the cavity resonant mode of 2 nm under 574 mW/cm^2 illumination, corresponding to a maximum change in reflectivity of 58% at 1497.5 nm [Fig.51a].

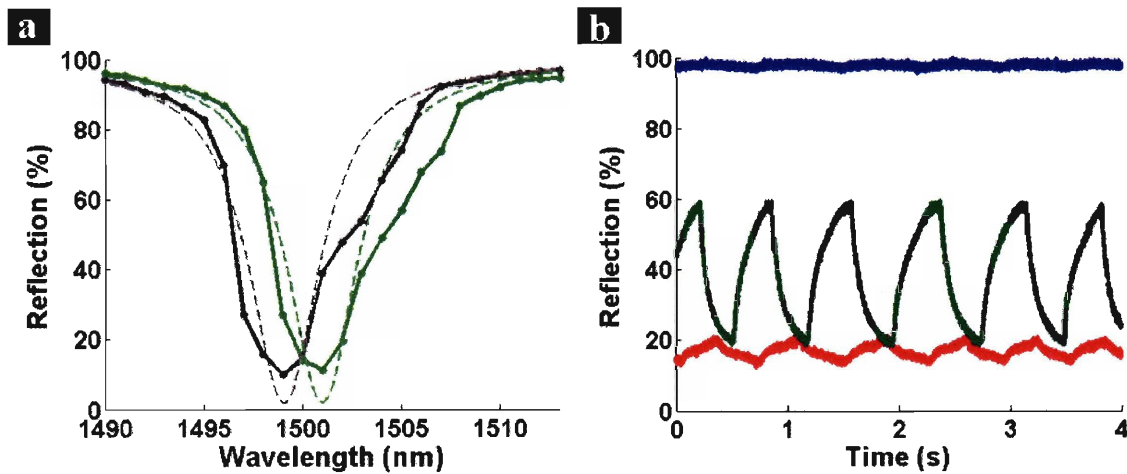


Figure 51: **a** In-situ NBR measurements of the cavity resonant mode. The solid grey and green lines show the experimental reflectivity measured in the dark and under illumination, respectively. The dashed curves show the corresponding reflectivity calculated with the TMM. **b** Fiber reflectivity measured over time under illuminated with a 574 mW/cm^2 modulated PD beam at three different probe wavelengths: 1550 nm (blue), 1599.2 nm (red) and 1497.5 nm (green).

We computed a theoretical shift of the cavity resonant mode under these illumination conditions using the following algorithm:

- the cavity layer was initially discretized into 100 sub-layers of homogeneous refractive index;
- at time t , the PD intensity profile $E^2(x,t)$ in the structure was calculated;
- the amplitude of the transient PD $TPD(E^2(x,t))$ was derived using its experimentally determined intensity dependence [Fig.44b];

- the refractive index change effective at time t was computed using the intensity dependence of the characteristic times of the transient PD given by Eq.103-106: $\Delta\tilde{N}(t)=TPD(E^2(x,t)).F(t,\tau(E^2(x,t)))$ where F denotes the fraction of transient PD actually reached at time t ;
- the values of the refractive indices of the As_2S_3 and As_2Se_3 layers were updated;
- the algorithm repeated itself by computing the new intensity profile at $t+\Delta t$.

This led to a theoretical shift of 2.2 +/- 0.3 nm. Possible sources of error included the uncertainty on the actual incident power due to the cylindrical geometry of the fiber and the uncertainty on the characteristics of the transient PD in the chalcogenide fiber layers compared to thin films. Because of the poor thermal conductivity of the polymer layers, the glass layers were subjected to a moderate heating under illumination <35 °C at the fiber surface (measured with a (FLIR) infrared camera) and <5 °C in the cavity layer (estimated). The corresponding thermal expansion was well below 0.01% for all layers.

To characterize the dynamic behavior of the optical tuning, we modulated the PD beam with a chopper and measured the induced modulation of the fiber reflectivity by connecting the InGaAs detector to a (Tektronic TDS 3032B) oscilloscope [Fig.49]. The wavelength dependence of the amplitude of the fiber reflectivity modulation [Fig.51b] was a clear indication that it was induced by a shift in the spectral position of the cavity resonant mode. For a PD beam intensity of 574 mW/cm² modulated at 1.5 Hz, the maximum change in the fiber reflectivity was equal to 41% at the cavity edge (1497.5 nm). Fig.52 shows the temporal response of the fiber reflectivity at two other modulation frequencies (25 and 150 Hz) for the probe wavelength that yielded the largest modulation at 1.5 Hz.

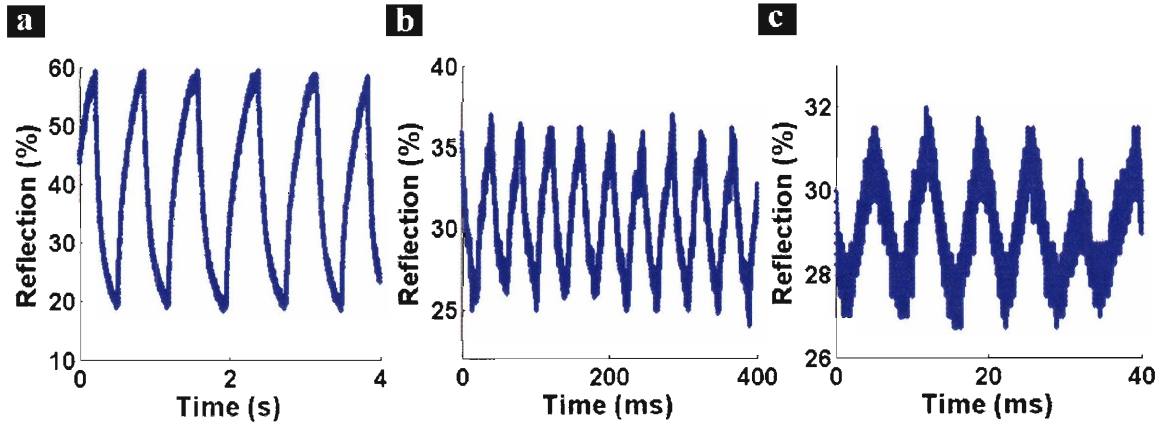


Figure 52: Modulation of the Fabry-Perot fiber reflectivity at 1497.5 nm for a modulation frequency of the PD beam equal to 1.5 Hz (a), 25 Hz (b) and 150 Hz (c).

We now define a figure of merit for these fibers as the ratio of the reflected power at 1497.5 nm with and without PD illumination, also called the *On-Off ratio*. Such figure of merit is typically used to characterize optical switches because it is a measure of their intrinsic signal to noise ratio. Fig.53 reports the On-Off ratios measured under 574 and 861 mW/cm² illumination for modulation frequencies up to 400 Hz.

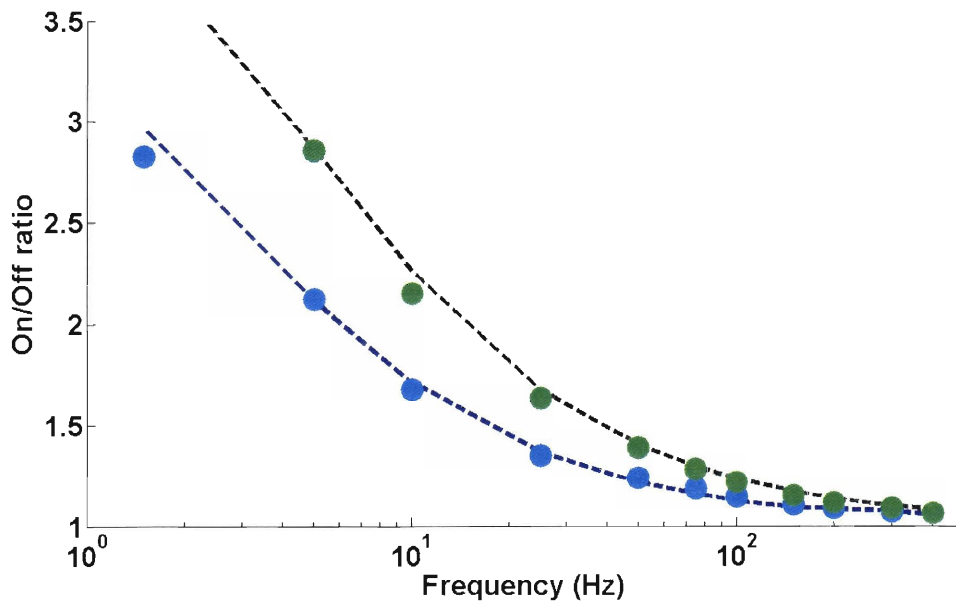


Figure 53: On-Off ratio measured at 1497.5 nm under 574 mW/cm² (blue) and 861 mW/cm² (green) illumination as a function of the PD modulation frequency. The dots are experimental values while the dashed lines were determined numerically.

Increasing the PD-beam intensity to 861 mW/cm^2 increased significantly the On-Off ratios due to a faster and larger index change in the cavity layer while further increase did not result in any improvement because of an increase in the decay times of the TP and in the absorption coefficient of the chalcogenide glasses at 514 nm. We used the TMM and the algorithm described previously to compute the expected On-Off ratios under similar experimental conditions and obtained very good agreement with the measurements [Fig.53].

The amplitude of the dynamic optical tuning was limited by the fundamental response time of the materials while its efficiency was limited by the Q factor of the Fabry-Perot cavity. In addition, the On-Off ratios were also penalized by the relatively high reflectivity at the resonant wavelength ($\sim 15\%$), which results from the difference between the reflection coefficients of the mirrors surrounding the cavity layer due to the fundamental dissymmetry of the structure. These results can be improved by increasing and optimizing the number of bilayers surrounding the cavity layer. In addition, illumination with short high peak power light pulses could lead to significantly faster response times since the speed of the transient photodarkening is ultimately determined by the number of absorbed photons. Recent studies suggest that sub-microsecond rise times are achievable.^{52,82} Finally, As_2Se_3 is also well-known for its high non-linearities (~ 400 times higher than in silica) making it an excellent candidate to demonstrate bistability and ultra-fast all-optical switching.

VI Hollow core photonic band-gap transmission fibers

The transmission of electro-magnetic waves in hollow waveguides dates back to the early 1970's with Bell-labs' WT4 long-haul communication system¹ designed to transmit millimeter waves in a hollow metallic tube. Although the advent of high-purity silica fibers set the basis for modern optical communications, the general approach of confining light in a hollow-core waveguide having highly reflective walls had been continuously explored for a broad range of wavelengths and intensities where the use of solid-core fibers is not feasible.^{83,84} Conventional optical fibers rely on guiding light

through total internal reflection in solid materials, a process that has fundamental limitations stemming from light absorption by electrons and phonons, material dispersion, Rayleigh scattering, and various non-linear effects. These limitations have motivated the study of light propagation in hollow fibers with many applications in high-power laser guidance for medical procedures,^{84,85} atom guiding,⁸⁶ high-harmonic generation,⁸⁷ among others.

Hollow-fiber technology is not without precedent, and hollow metallic or metallo-dielectric waveguides have been studied extensively and have found use in several practical applications, including the transmission of high-power CO₂ laser light.^{88,89} Nevertheless, finite metal conductivity in the visible and NIR results in high transmission losses, and the use of metallic linings limits both the fabrication length and mechanical flexibility of these fibers.

Exploration of Bragg reflection as a mechanism for light guidance in a hollow core was initiated in 1978 by Yeh and Yariv⁹⁰ who theoretically investigated the transmission of non-index-guided modes through a hollow multilayer cylindrical structure by Bragg reflection from the cladding. Nevertheless, limitations on the refractive index contrast inherent in doped-silica technology led to pessimistic assessments of the potential of such structures. Recent research concerning photonic band-gaps exhibited by higher dimensionality photonic crystal structures has excited interest in fabricating optical fibers that guide light through the effect of a complete photonic band-gap enforced by a two dimensional periodic cladding structure fabricated of silica glass containing air holes.^{1,91}

Our hollow core transmission photonic band-gap fibers rely on the omnidirectional reflectivity of the Bragg structure that lines their core as a confinement mechanism. Omnidirectional reflectivity is provided by the large photonic band-gaps established by multiple alternating layers made of a high refractive index chalcogenide glass and a low refractive index polymer (section II.1).^{4,85,92} The same polymer can be used as a cladding material, resulting in fibers composed of more than 98% polymer by volume (not including the hollow core) that combine high optical performance with polymeric processability and mechanical flexibility. A distinctive feature of this light-

guidance mechanism is that it is ‘wavelength scalable’, i.e. the final scale of the structure determines the wavelength of light that is transmitted along the fiber [Fig.1a]. This allows us to produce hollow-core transmission fibers with a fundamental photonic band-gap at 10.6 μm for high power CO₂ lasers used in laser surgery and materials processing applications, at 3 μm for the transmission of high-energy Er:YAG laser radiation, at 1.5 μm for use in telecommunications applications, at 750 nm for biomedical applications, in the visible for lasing and sensing applications (e.g. TNT sensing) down to 350 nm for high power UV light delivery.

These novel fibers provide performances already comparable or in excess of the best waveguides currently available at 10.6 μm . Although powerful and efficient CO₂ lasers are available, waveguides operating at this wavelength have remained limited in length or loss levels.^{84,88,89,93} Our approach yields tens of meters of flexible hollow photonic band-gap fibers for transmission of CO₂ laser light, with waveguiding losses lower than 1 dB/m and transmitted power densities exceeding 1.3 KW/cm² (25 W in a 500 mm hollow-core diameter). In addition, the flexibility of the fiber allows for surgeons to use it to gain access to otherwise inaccessible areas such as tumors in lung cancer patients [Fig.54].

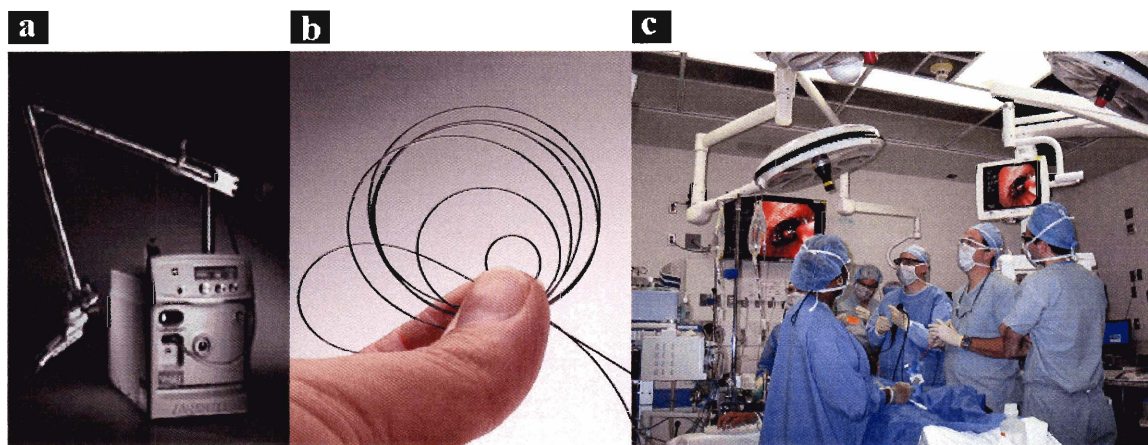


Figure 54: **a** Current technology used for CO₂ laser light delivery: free space optics, **b** future technology: flexible hollow-core photonic band-gap fibers, **c** use of our fibers for the very first non-invasive lung-cancer surgery performed by Dr. R. Bueno at the Brigham and Women’s Hospital in Boston on October 28, 2005. (Courtesy of the Brigham and Women’s Hospital)

Several other medical procedures and material processing applications could benefit from the unique features of these fibers.

VI.1 Guided modes in hollow core transmission photonic band-gap fibers

The structure of our transmission fibers consists of a hollow core surrounded by alternating high and low refractive index layers that form an omnidirectional Bragg reflector and a thick polymer cladding [Fig.55].

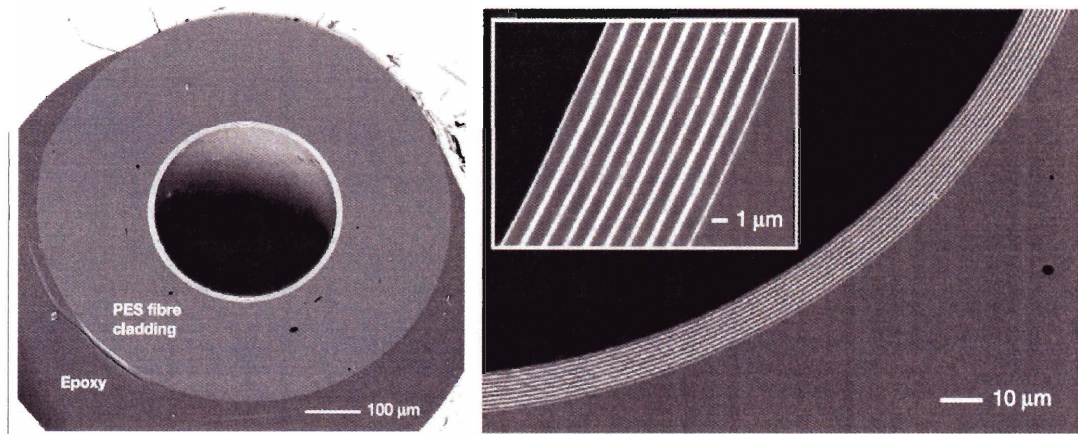


Figure 55: SEM imaging of the cross-section of a fiber made of As_2Se_3 and PES with fundamental band-gap around $3.55 \mu\text{m}$ taken at different magnifications. The first chalcogenide layer is systematically chosen to be half-thick to eliminate surface states that would induce high propagation losses. (Courtesy of S.D. Hart and B. Temelkuran)

Because of our fabrication technique (section IV.1), the mirror layers form a spiral around the core and a seam is present at the surface of the multilayer structure as shown in Fig.27b corresponding to the very beginning of the rolling process. For simplicity, we will assume in all our calculations that the structure consists instead of concentric layers with a perfectly square periodic refractive-index profile and that the real structure could eventually be studied by perturbation theory.

VI.1.1 Solutions to the wave equation in cylindrical coordinates

In order to understand and optimize the characteristics of light propagation in our fibers, we need to solve Maxwell's equations in cylindrical coordinates. The longitudinal

electro-magnetic field (E_z, H_z) in each isotropic and homogeneous layer of refractive index n satisfies the following wave equation: ⁹⁰

$$\left[\nabla^2 - \frac{\partial^2}{\partial z^2} + \left(\frac{\omega^2 n^2}{c^2} - \beta^2 \right) \right] \begin{bmatrix} E_z \\ H_z \end{bmatrix} = 0 \quad (107)$$

and is characterized by three conserved quantum numbers: its frequency ω , the component of its wave-vector parallel to the layers, also called axial wave-vector, β and its angular-momentum m . As a result, it consists of a superposition of Hankel functions and falls into one of the two following categories:

$$E_z(r, \theta, z) = [A_q H_m^I(k_q r) + B_q H_m^{II}(k_q r)] \cos(m\theta) e^{i(\beta z - \omega t)} \quad (108)$$

$$H_z(r, \theta, z) = [C_q H_m^I(k_q r) + D_q H_m^{II}(k_q r)] \sin(m\theta) e^{i(\beta z - \omega t)} \quad (109)$$

or

$$E_z(r, \theta, z) = [A_q H_m^I(k_q r) + B_q H_m^{II}(k_q r)] \sin(m\theta) e^{i(\beta z - \omega t)} \quad (110)$$

$$H_z(r, \theta, z) = [C_q H_m^I(k_q r) + D_q H_m^{II}(k_q r)] \cos(m\theta) e^{i(\beta z - \omega t)} \quad (111)$$

where H_m^I and H_m^{II} are Hankel functions of type I and II that represent the outgoing and incoming waves, respectively, $k_q^2 = \omega^2 n_q^2 / c^2 - \beta^2$ is the transverse component of the wave-vector and A_q, B_q, C_q and D_q four unknown coefficients associated with layer q . The boundary conditions at each interface require the continuity of the transverse components of the electro-magnetic field (i.e. E_r, H_r, E_θ and H_θ), which can be expressed in terms of E_z and H_z as follow:

$$E_r = \frac{i\beta}{k_q^2} \left(\frac{\partial}{\partial r} E_z + \frac{\omega}{\beta \epsilon_0 c^2} \frac{\partial}{r \partial \theta} H_z \right) \quad (112)$$

$$E_\theta = \frac{i\beta}{k_q^2} \left(\frac{\partial}{r \partial \theta} E_z - \frac{\omega}{\beta \epsilon_0 c^2} \frac{\partial}{\partial r} H_z \right) \quad (113)$$

$$H_r = \frac{i\beta}{k_q^2} \left(\frac{\partial}{\partial r} H_z - \frac{\omega \epsilon_0 n_q^2}{\beta} \frac{\partial}{r \partial \theta} E_z \right) \quad (114)$$

$$H_\theta = \frac{i\beta}{k_q^2} \left(\frac{\partial}{r \partial \theta} H_z + \frac{\omega \epsilon_0 n_q^2}{\beta} \frac{\partial}{\partial r} E_z \right) \quad (115)$$

As in the planar case, this system of equations can be written in a matrix formalism resulting in 4x4 transfer matrices that relate the unknown coefficients in one layer to the ones in its adjacent layers.⁹⁰ In addition, we assume that there is no incoming wave in the outermost cladding (i.e. $B_c=0$ and $D_c=0$). This leads to a unique solution for which the coefficients in layer q are given by:

$$\begin{bmatrix} A_q \\ B_q \\ C_q \\ D_q \end{bmatrix} = [P^q] \cdot [T^{q/q+1}] \cdot [P^{q+1}] \dots [T^{N-1/N}] \cdot [P^N] \cdot [T^{N/Cladding}] \cdot \begin{bmatrix} 1 \\ 0 \\ 1 \\ 0 \end{bmatrix} \quad (116)$$

where the propagation matrices P and transfer matrices T as introduced in section II.1.2 are now 4x4 matrices.

VI.1.2 Identifying the guided modes: the leaky-mode technique

Light does not propagate randomly in the fiber core and any solution to the wave equation does not necessarily correspond to a guided mode. Indeed, due to the finite dimension of the fiber core, it is expected that only a discrete set of modes will be confined by the structure while any other solution will radiate away from the core. These guided modes can be found using the *leaky-mode technique*, which consists in solving for the minima of the radial component of the time-averaged Poynting flux integrated over the outer fiber circumference.⁹⁰

$$\min \left(\int_S S_r dS \right)_m = \min \left(\int_S \frac{1}{2} \text{Re}[E_\theta H_z^*] dS \right)_m \quad (117)$$

This method is used to calculate the dispersion relation $\omega(\beta)$ of the lowest-order confined modes for each angular momentum m . The total number of guided modes supported by the fiber depends on its core radius R and scales as $\sim R^2$, corresponding to a modal separation $\Delta\beta \sim 1/R^2$.

The guided modes are classified according to their polarization state. The polarization that has its electric field in the plane transverse to the direction of propagation, i.e. $E_z=0$, is referred to as the *TE* polarization and the polarization that has its magnetic field in the plane transverse to the direction of propagation, i.e. $H_z=0$, as the

TM polarization. Modes with zero angular momentum ($m=0$) are purely *TE* or *TM* polarized as can be seen from Eq.108-111 and noted TE_{0i} and TM_{0i} , where i is the order of the mode. By convention, the order of a mode increases as it is located further away from the light-line $\omega=\beta c$. Modes with non-zero angular momentum ($m\neq 0$) are hybrid modes noted HE_{mi} or EH_{mi} if the *TE* or *TM* component of their polarization, respectively, is dominant.^{7,94} The intensity and polarization profiles of some fundamental guided modes are shown in Fig.56.

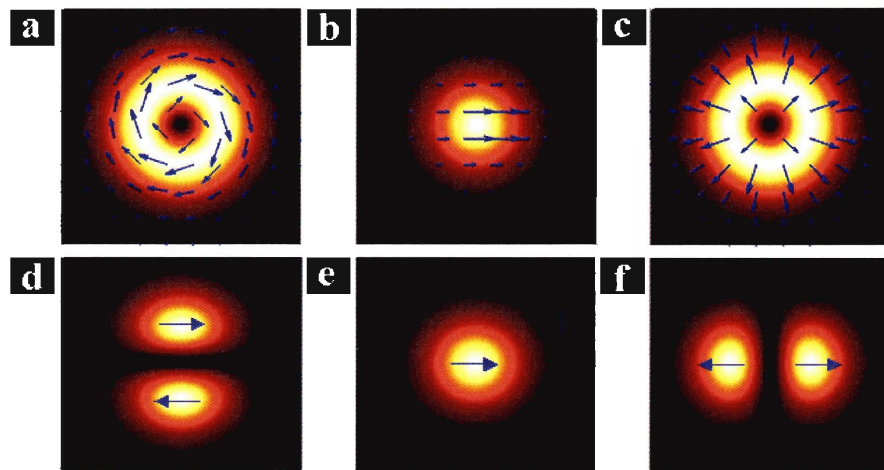


Figure 56: Intensity and polarization profiles of the TE_{01} mode (a), HE_{11} mode (b), and TM_{01} mode (c). Note that it is impossible to distinguish the TE_{01} mode from the TM_{01} mode from their intensity profile only; d, e, f same after a horizontal linear polarizer: the TE_{01} and TM_{01} mode can now be distinguished.

The HE_{11} mode [Fig.56b] is the only mode that has a perfect overlap with the linearly polarized Gaussian output of a laser making it the most likely mode to be excited in practice. The lower-loss TE_{01} mode could be excited fairly efficiently if the incident beam had the polarization profile shown in Fig.56d, which can be constructed using a Spatial Light Modulator (SLM).

VI.1.3 Modal characteristics

The combined information of the photonic band diagram associated with the planar equivalent of the omnidirectional Bragg reflector that lines the fibers' core and the dispersion relations of the guided modes previously identified allows us to predict the

characteristics of light propagation in our fibers. Modes propagating in a hollow core fiber travel through air along the axis of the fiber and must be reflected by the multilayer mirror. They must therefore correspond to states that are just above the light-line and within the photonic band-gaps, where high transmission is expected. This is demonstrated in Fig.57a.

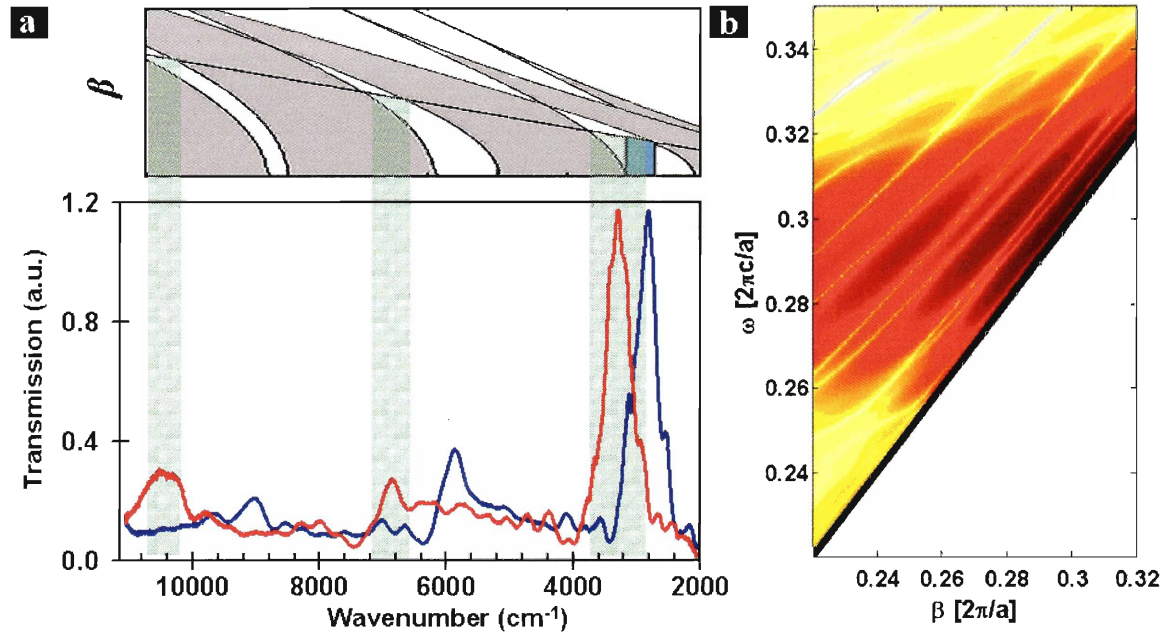


Figure 57: **a** Photonic band diagram and resulting transmission spectrum for a 30-cm long fiber (in red). The photonic band diagram is calculated for the planar equivalent of the omnidirectional Bragg reflector that lines the fiber's core. The TE and TM polarizations are overlapped and the omnidirectional reflectivity regime in the fundamental band-gap is highlighted in blue. The blue transmission spectrum shows how the transmission characteristics of these fibers can be shifted by changing their outer diameter. **b** Detail of the fundamental photonic band-gap (in red) near the light-line (black line) showing the dispersion relation $\omega(\beta)$ of the first few HE_{1i} and EH_{1i} modes, $i \geq 1$ (yellow lines). The calculation was done for a core size of 10λ for clarity. The parameter a corresponds to the bilayer thickness (i.e. $a=d_1+d_2$).

Fig.57b shows the fundamental photonic band-gap and the dispersion relation $\omega(\beta)$ of the confined HE_{1i} and EH_{1i} modes closest to the light-line, which are most likely to participate in the transport of light. It can be seen that away from the band-gap edges, the group velocity $d\omega/d\beta$ of all the modes is slightly lower than c and that higher-order modes have a lower group velocity. Though strictly inaccurate, this can be understood

intuitively from a ray-tracing analogy where modes propagate in the fiber core by bouncing off the omnidirectional Bragg reflector that lines it: at fixed m and ω , higher-order modes have lower β values corresponding to a smaller incidence angle on the multilayer structure. This results in a longer optical path or equivalently a lower group velocity. As a corollary, the only mode that can propagate in the fiber core with a group velocity of c is a non-confined plane-wave.

It can also be understood from the ray-tracing analogy why higher-order modes have higher propagation losses. Indeed, each time a mode bounces off the omnidirectional Bragg reflector, its electro-magnetic field decays exponentially in the mirror layers [Fig.3b] and is attenuated due to material absorption and radiation leakage. Radiation leakage results from the finite number of mirror layers that allows for the field power to tunnel through the omnidirectional Bragg reflector. It can be systematically reduced by increasing the number of bilayers and vanishes for an infinite multilayer structure [Fig.58a].

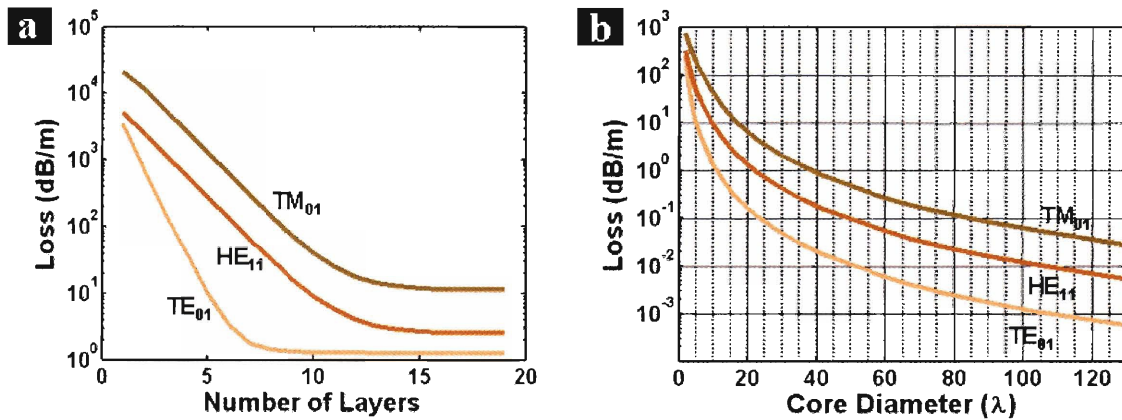


Figure 58: **a** Propagation losses as a function of the number of mirror layers for a core size of 10λ . Losses of the TE_{01} mode are reduced by a factor 5 for each additional bilayer while losses of the HE_{11} and TM_{01} modes are only reduced by a factor 2. Radiation losses fall below material losses for 15 layers or more. **b** Propagation losses as a function of core diameter for a structure consisting of 20 layers. Losses of the TE_{01} mode vary as $1/R^3$ while losses of the TM_{01} mode vary as $\sim 1/R^2$. For both (a) and (b), the structure is made of As_2Se_3 and PES and is designed to operate at $1.55 \mu\text{m}$. (Courtesy of O. Shapira)

The fraction of field power that penetrates the mirror layers and determines the propagation losses of a given mode also depends on its polarization state due to different

boundary conditions for the TE and TM polarizations. Clearly, the TM band-gap offers less confinement than the TE band-gap due to the existence of the Brewster angle below the light-line [Fig.4]. As an example, the total field power that penetrates the mirror layers for the TE_{0l} mode scales as $1/R^3$ while it scales as $1/R^2$ for the TM_{0l} mode, where R is the fiber core radius [Fig.58b].⁷ Fig.59 summarizes the strong loss discrimination that exists between all the guided modes.

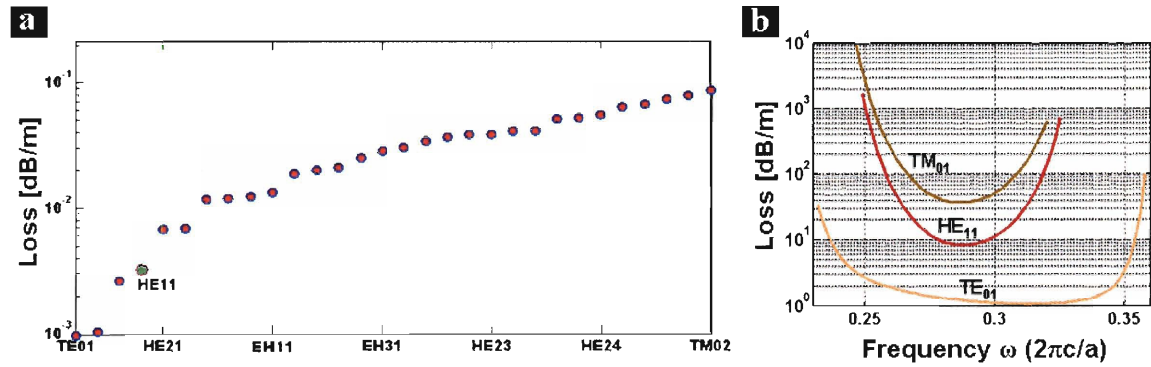


Figure 59: **a** Propagation losses calculation for the 30 lowest-energy modes with an angular momentum less than 4 in a hollow core photonic band-gap fiber made of As_2Se_3 and PEI and operating at $1.55 \mu m$. The omnidirectional Bragg reflector contains 26 bilayers and the fiber core diameter is equal to 100λ . The HE_{11} mode is highlighted in green. **b** Propagation losses versus frequency for a structure designed to operate at $1.55 \mu m$ and consisting of 10 bilayers of As_2Se_3 and PES and a 10λ core size. (Courtesy of O. Shapira)

This has several important practical consequences. First, while single-mode fibers are difficult to fabricate with our current fabrication technique due to the required small core diameter, it is nevertheless possible to operate multi-mode fibers in a nearly single-mode regime since the TM_{0i} modes and high-order HE_{0i} and EH_{0i} modes disappear over relatively short fiber lengths, an effect known as *mode-filtering*.⁹⁵ On the other hand, while the guided modes are orthogonal to each others in the unperturbed system, small perturbations and bends can couple two modes together if their angular momentum differ by ± 1 . As a consequence, a fraction of the electro-magnetic energy transported dominantly by the lowest-loss mode initially excited (typically the HE_{11} mode) can be transferred to lossier modes resulting in an increase in overall propagation losses. This

effect is likely to be more pronounced in large core fibers where the modal separation $\Delta\beta$ is small.

VI.2 Transmission measurements

VI.2.1 Spectral characterization

Broadband transmission measurements are performed using our (Bruker Optics) FTIR [Fig.28]. Light is coupled to the fiber with a focusing lens while the fiber output is butt-coupled to an external detector. The fiber's ends are cut very carefully with a (Leica 818) microtome blade to ensure that the core at the input and output is not obstructed by collapsed layers. In addition, they must be gold coated to avoid significant light coupling to the polymer cladding. Indeed, both PES and PEI exhibit strong transmission peaks in the following transparency windows: 1-1.1 μm , 1.2-1.3 μm and 1.5-1.6 μm for PES and 1.22-1.32 μm and 1.52-1.57 μm for PEI. Three external detectors are available: a Si detector, an InGaAs detector and a MCT detector, allowing for transmission measurements anywhere from 25 microns to 650 nm. Transmission measurements down to 300 nm are obtained using a UV or white light source (e.g. a mercury lamp) and a (e.g. Ocean Optics HR2000GG-UV-NIR) spectrometer. Fig.60 illustrates the use of these different techniques and demonstrates the wavelength scalability of the omnidirectional Bragg reflector that lines the core of our fibers.

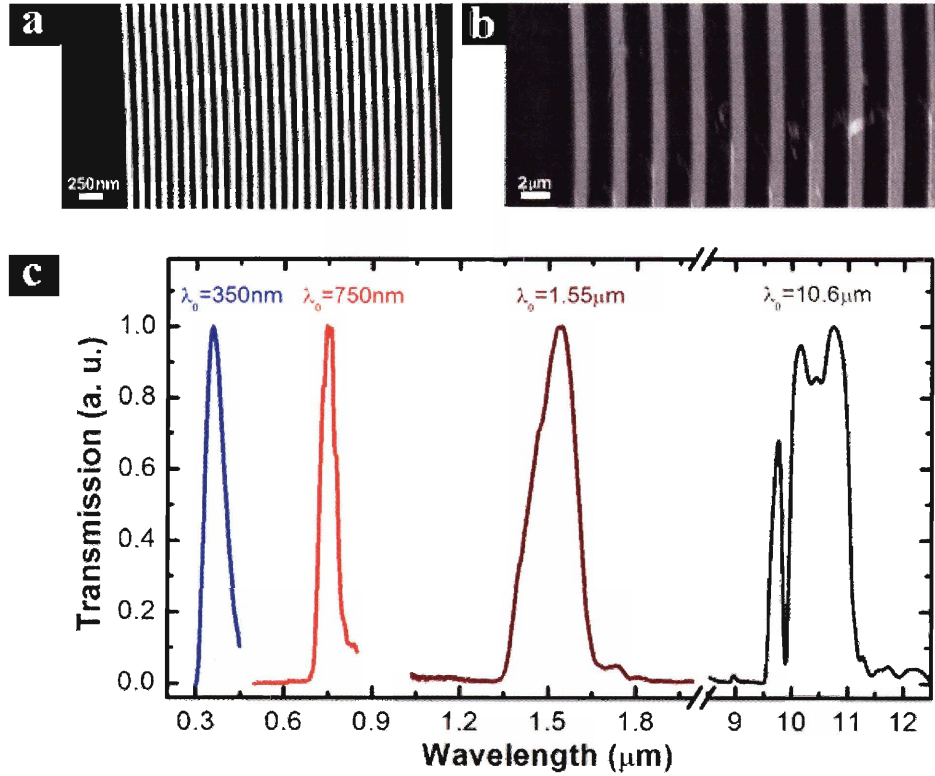


Figure 60: SEM micrographs of Bragg layers in fiber transmitting at 350 nm (a) and at 10.6 μm (b). c Measured transmission spectra of fibers drawn to different layer thicknesses. λ_0 denotes the center wavelength of each transmission peak. The shape of the transmission peak at 10.6 μm is distorted by absorption lines from PES.

We have fabricated transmission fibers operating in the UV, visible, near-IR⁹², and mid-IR⁸⁵ using the same fabrication technique and the same materials despite their strong chromatic dispersion (section III.4). Scanning electron microscope imaging of the mirror layers reveals that the final layer thicknesses strongly correlate to the measured transmission peaks. The structure shown in [Fig.60a] consists of alternating layers of As_2S_3 and PEI with feature sizes below 30 nm, resulting in a transmission peak at 350 nm. Increasing the dimensions of the alternating layers of As_2Se_3 and PES to $\sim 1 \mu\text{m}$ [Fig.60b], leads to a shift of the transmission peak to 10.6 μm .

VI.2.2 Modal characterization

A more detailed characterization of the modes actually transmitted through the fibers requires to perform narrow-band transmission measurements using single-

wavelength or tunable lasers. The small range of wavelengths and the fundamental properties of laser beams make it possible to couple light into the fiber core with high efficiency. This is achieved by using a lens that focuses the collimated incident laser beam to a diameter equal to $\sim 70\%$ of the fiber core diameter (D_{core}):

$$D_{core} = \frac{100}{70} \left(\frac{4\lambda}{\pi} \right) \left(\frac{F}{D_{incident}} \right) \quad (118)$$

where F is the focal length, λ is the laser wavelength and $D_{incident}$ is the diameter of the laser beam before the lens.

The modal output of the fibers can be imaged using a focusing lens and a Charge Coupled Device (CCD) infra-red camera. As a general rule, we found that 0.5-m long fibers with core diameter smaller than 50λ were nearly single-mode while fibers with core diameter larger than 60λ appeared clearly multi-mode, as shown in Fig.61.

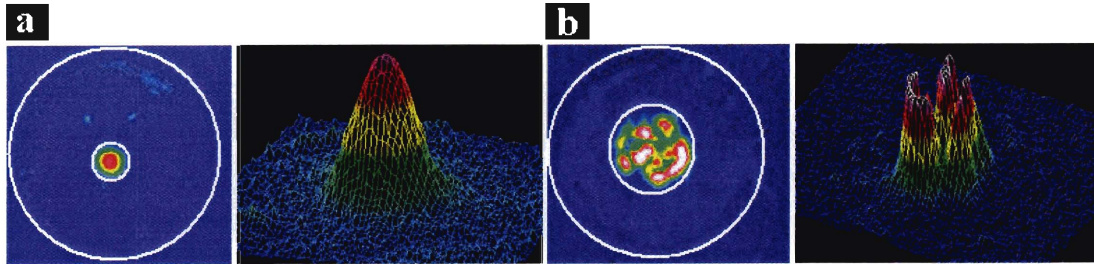


Figure 61: IR images and beam profiles of the output of 0.5-m fibers transmitting around $1.55 \mu\text{m}$ with core-diameters equal to $80 \mu\text{m}$ (a) and $170 \mu\text{m}$ (b). The fibers' inner and outer circumferences are highlighted in white.

Because of its strong overlap with linearly-polarized Gaussian laser beams, the HE_{11} mode is typically predominant in nearly single-mode regimes for frequencies well within the band-gap [Fig.61a]. A small contribution of the TE_{01} mode can usually be detected by placing a linear polarizer in the beam path and rotating it until complete extinction of the HE_{11} mode. This contribution becomes dominant at the band-gap edges where the propagation losses of the HE_{11} mode increase dramatically while they remain constant for the TE_{01} mode due to its stronger confinement [Fig.59b]. Coupling to the TE_{01} mode can occur at the fiber's input if the laser beam is not perfectly centered with the fiber core or be induced by bends and other perturbations along the length of the fiber.

VI.2.3 Propagation losses characterization

Propagation losses are measured by *cutback measurements*, which consist in measuring at a fixed wavelength the output power of the fiber as a function of its length. The fiber, initially more than 2-m long, is held straight and shortened progressively until it is no less than 1-m long to ensure that it is operating in a nearly single-mode regime at each step of the measurement. Since all the guided modes decay exponentially while propagating in the fiber, the logarithm of the output power versus the fiber's length draws a straight line [Fig.62] whose slope corresponds to a weighted average of the propagation losses in dB/m of all the excited modes (Eq.37).

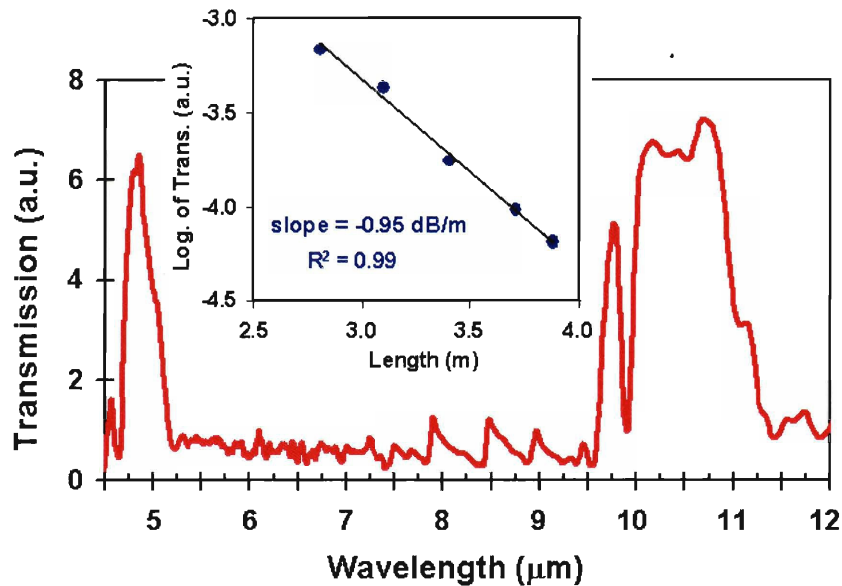


Figure 62: Typical transmission spectrum of hollow core fibers designed to transmit CO₂ laser light. The fundamental photonic band-gap is centered around 10.6 μm, and the second-order band-gap around 5 μm. Insert, cutback measurement performed at 10.6 μm showing propagation losses below 1 dB/m in a 700-μm core diameter fiber. (Courtesy of S.D. Hart and B. Temelkuran)

Propagation losses can also be approximated with a non-destructive method that consists in measuring the radiated power as a function of position along the fiber, which is done by scanning the outside of the fiber with an integration sphere and the appropriate detector. At 10.6 μm, cutback measurements were performed using a (Coherent-DEOS GEM-25) 25-W CO₂ laser and a (Newport 818T-10) high-power detector. At 1.55 μm,

they were performed with a (Photonics Tunicus plus or Ando AQ4321D) tunable laser and a (Newport 818IG) InGaAs detector

One interesting figure of merit for these fibers is the comparison of their optical transmission losses to the intrinsic losses of the materials composing them. Reported optical losses at 10.6 μm for commercially available As_2Se_3 are typically greater than 10 dB/m, while losses for PES exceed 100,000 dB/m. Transmission losses at 10.6 μm in photonic band-gap fibers fabricated out of these two materials however are lower than 1 dB/m [Fig.62], demonstrating that waveguide losses orders of magnitude lower than the intrinsic fiber material losses can be achieved. We have further demonstrated that power densities sufficient to burn holes in a film of PES, the fiber majority component, and beyond can be transmitted through these fibers.⁸⁵ This is made possible by the very short penetration depths of electro-magnetic waves in the high refractive-index contrast photonic crystal structure, thus enabling low attenuation through structural design rather than high-transparency material selection and allowing these same materials to be used at wavelengths that may have been thought improbable.

The propagation losses measured at 10.6 μm are fairly close to the theoretical propagation losses of the HE_{11} mode calculated for similar fibers indicating that they result primarily from material absorption in the mirror layers. However, we have measured propagation losses at 1.57 μm in a 165- μm core diameter fiber equal to 5.5 dB/m,⁹² which is orders of magnitude higher than the computed values for the first 30 lowest-loss modes [Fig.59]. More recent measurements have demonstrated losses around 2 dB/m in 50λ core-diameter fibers designed to operate around 1.55 μm , suggesting that these high losses are not fiber specific. Though it has not yet been proven, the discrepancy is attributed to scattering of the propagating core-modes that can induce perturbations of their axial wave-vector β . If $\Delta\beta$ is large enough, these core-modes are no more confined in the fiber core and become radiative modes. Different scattering sources could be involved such as roughness, point defects, non-stoichiometric glass composition and others at the multiple interfaces between the high refractive-index-contrast mirror layers. Such perturbations to the ideal structure are unfortunately difficult to account for in our TMM calculations.

Other perturbations can lead to an increase in propagation losses, such as shallow bending. Preliminary results show that bending losses do not reduce dramatically transmission in the fundamental photonic band-gap, while high-order band-gaps experience much higher bending losses.⁸⁵ This is expected because in our structures, the fundamental band-gap exhibits omnidirectional reflectivity while high-order gaps do not [Fig.57a]. These results are shown in Fig.63, where a 30-cm long fiber having a fundamental band-gap at 3.55 μm was looped into a small ‘knot’ consisting of multiple bends.

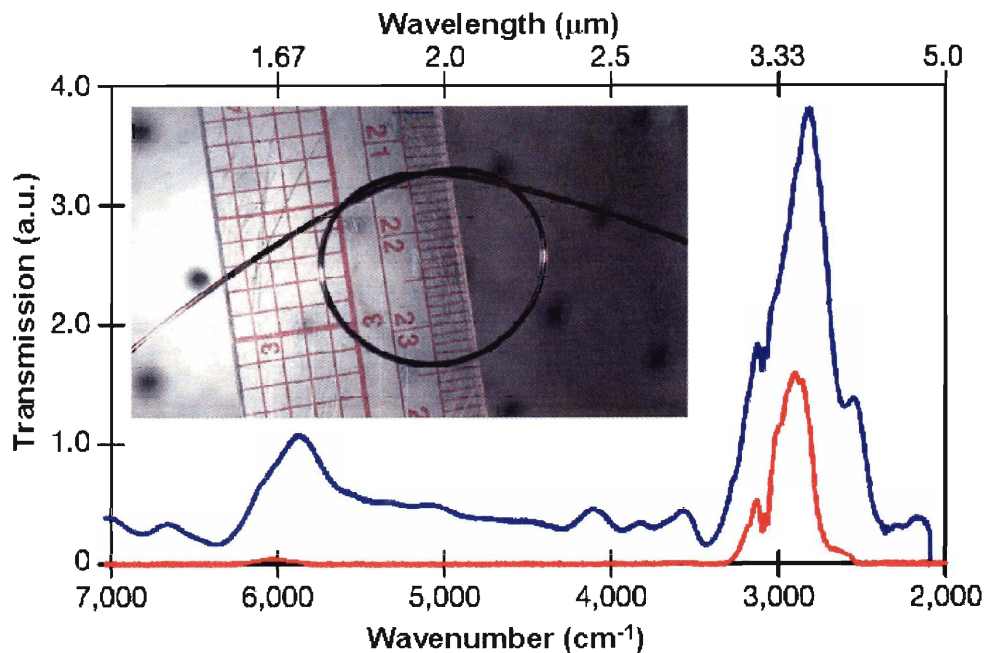


Figure 63: Transmission spectra for the straight (blue) and the ‘knotted’ (red) hollow-core fiber having a fundamental band-gap at 3.55 μm . The knot had a radius of ~ 2 cm (see insert). (Courtesy of S.D. Hart and B. Temelkuran)

Approximately 40% of the light in the fundamental band-gap was transmitted through this highly perturbed fiber when compared to the straight fiber, while transmission in the second-order gap at 1.7 μm was attenuated much more strongly.

VI.3 Mechanical tuning of transmission photonic band-gap fibers

Based on the results demonstrated in fibers designed for external reflection (section V.2), we have studied the mechanical tuning of a transmission fiber whose third order band-gap was around 767 nm. The corresponding fundamental band-gap was around 2.3 μm and the fiber core diameter was $\sim 220 \mu\text{m}$. We used a (Oriel) mercury lamp as a white light source and a (Ocean Optics HR2000GG-UV-NIR) spectrometer to measure transmission spectra as a function of the applied axial strain [Fig.64].

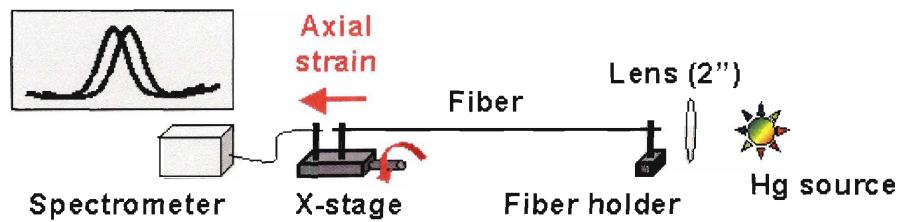


Figure 64: Setup for the mechanical tuning of transmission fibers.

The input end of the fiber was fixed and light was coupled to it using a focusing lens with a 2" focal length. The output end was butt-coupled to a multi-mode fiber connected to the spectrometer and both fibers were mounted on a x-stage. This enabled us to apply a strain in the axis of the fiber without perturbing the output coupling. The fiber ends were glued with epoxy to two plastic tubes that were tightly mounted in fiber holders to prevent them from slipping during the measurements. We measured a maximum reversible shift of 4 nm under an applied strain of 1.2% corresponding to a normalized shift $\Delta\lambda/\lambda$ equal to 0.52% [Fig.65].

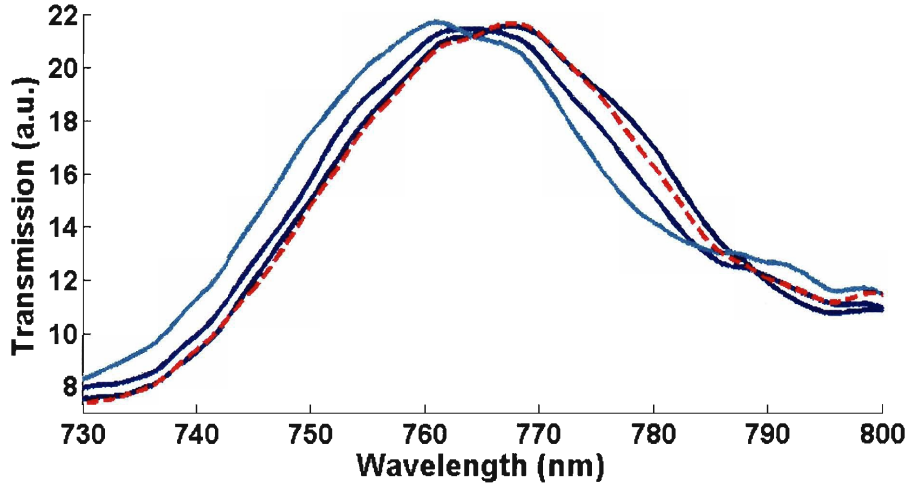


Figure 65: Shift of the transmission peak under increasing applied axial strain: $\varepsilon_{zz}=0\%$ (right, dark blue), $\varepsilon_{zz}=0.6\%$ (middle, blue) and $\varepsilon_{zz}=1.2\%$ (left, light blue). The red dashed curve corresponds to no applied strain ($\varepsilon_{zz}=0\%$) and was taken after the previous axial strains were applied to the fiber to demonstrate the reversibility of the induced shift.

Note that our opto-mechanical model (section V.2.1) predicts that all the layers in transmission fibers are under compressive radial stress during mechanical tuning, making delamination much less likely than in reflection fibers.

While large, the measured tuning range remains significantly smaller than the transmission bandwidth of these fibers (~ 20 nm). In addition, mechanical tuning requires to sacrifice flexibility, making it somewhat unpractical. Optical tuning on the other hand is ill-fitted because it is difficult to induce a uniform illumination over such extended fiber lengths, whether from the outside of the fiber or from the core by transmitting the photodarkening light in higher-order band-gaps. Fortunately, other tuning mechanisms may emerge in these fibers as we start drawing metallic electrodes in these composite fibers.

VI.4 Design of highly dispersive transmission fibers

Depending on the application pursued, group-velocity dispersion can be a limitation or a benefit. In telecommunication applications, it leads to a degradation of the optical signal at high bit rates or over long distances. For a given distance, the dispersion tolerance is proportional to the inverse of the square root of the bit rate. While it is possible to fabricate silica fibers with zero group-velocity dispersion,⁹⁶ some dispersion is nevertheless beneficial to suppress non-linear effects such as four-wave mixing. Therefore it must be compensated for, typically every 80 km or less, using dispersion compensating fibers with a large dispersion parameter of opposite sign.⁹⁷ On the other hand, chirped pulse amplification used to compress optical pulses beyond the non-linearity threshold of silica fibers requires high group-velocity dispersion and low nonlinearities, which is achieved using diffraction gratings (Treacy compressors), fiber Bragg gratings and more recently hollow core photonic band-gap fibers.^{98,99} High group-velocity dispersion has been reported in photonic band-gap optical fibers (e.g. 1150 ps/nm/km at 1560 nm)⁹⁸ but to this date only at the edge of their photonic band-gaps where propagation losses are high and little control over the dispersion of individual propagating modes can be achieved.

Here we demonstrate that by intentionally introducing micro-cavities in such fibers, one can achieve much higher normal and anomalous group-velocity dispersion within their photonic band-gaps as a result of interactions between the core-guided modes and the cavity resonant mode(s), thus combining controlled group-velocity dispersion with the advantages of fiber waveguiding. We show that there exist strong correlations between the amplitude and bandwidth of the group-velocity dispersion and the different fiber design parameters. In addition, because the dispersion is controlled in part by geometric parameters, mechanical tuning can be employed to dynamically fine-tune its value at a fixed wavelength and even switch its sign. While these fibers could be used for precise dispersion compensation in telecommunication applications and enable dynamic allocation of bit rates, they could also be used for all-fiber chirped pulse amplification and enable peak powers thought unreachable, beyond the damage threshold of most materials.

VI.4.1 Group-velocity dispersion in perfectly periodic photonic band-gap fibers

In perfectly periodic Bragg fibers, the group velocity of each guided mode varies across the band-gap, a property called *group-velocity dispersion*. Indeed, we saw in Fig.57b that the dispersion relations of the core-confined modes are nearly parallel to the light-line (i.e. $v_g \sim c$), except at the band-edges where a significant fraction of their electro-magnetic field leaks into the cladding resulting in a drop of their group velocity [Fig.66a].

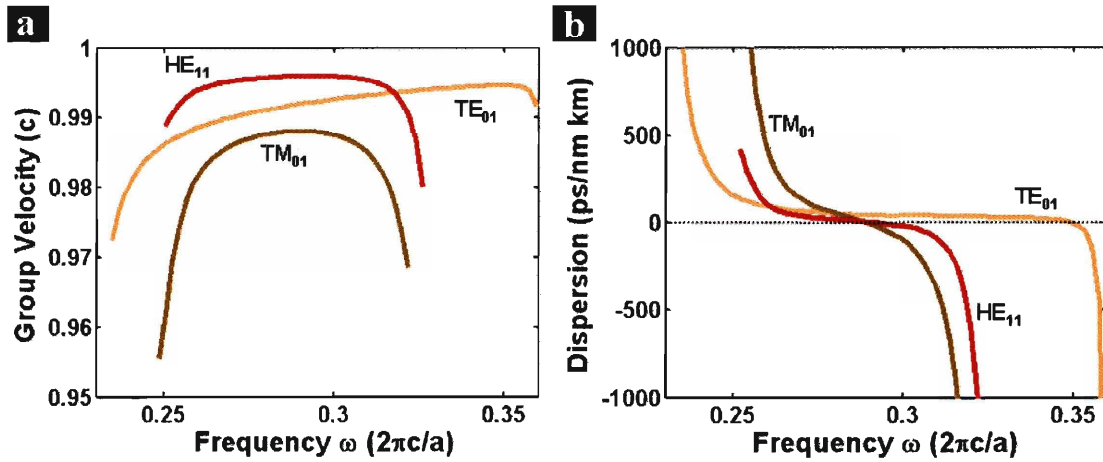


Figure 66: Group velocity (a) and dispersion parameter D (b) as a function of frequency across the band-gap for the TE_{01} , HE_{11} and TM_{01} fundamental core modes. (Courtesy of O. Shapira)

The corresponding group-velocity dispersion parameter D of a given mode [Fig.66b] is related to the curvature of its dispersion relation and is given by:

$$D(\lambda) = -\frac{2\pi c}{\lambda^2} \frac{\partial^2 \beta}{\partial \omega^2} = \frac{\partial}{\partial \lambda} \left(\frac{1}{v_g} \right) \quad (119)$$

where the inverse of the group velocity v_g is also called the *group delay*. This coefficient, reported in ps/nm/km, indicates the time spreading for a 1-nm wide optical pulse when propagating over a kilometer of fiber. Within the fundamental band-gap, D is predicted and has been measured to be between 5-10 ps/nm/km for the HE_{11} mode.^{7,100,101} For comparison, single-mode silica fibers have a dispersion coefficient at 1.55 microns of 17 ps/nm/km⁹⁷. While significant dispersion has been observed in photonic band-gap fibers

at the band-edges,⁹⁸ the lack of control over the exponentially decaying profile of the core modes in the periodic mirror structure and the associated high propagation losses make this mechanism unsuitable for high-performance applications.

VI.4.2 Group-velocity dispersion in transmission fibers containing micro-cavities

The periodic Bragg structure that lines the core of our fibers and is responsible for omnidirectional reflectivity offers a lot of flexibility in integrating micro-cavities that in turn can be used to precisely control the propagation losses, dispersion and non-linearities of the core-guided modes.¹⁰² The resonant modes of these micro-cavities correspond to frequencies within the band-gap that are confined in the corresponding cavity layers. In this study we limited ourselves to structures with a single cavity layer but multiple micro-cavities could be incorporated using the same fabrication technique. The number of cavity resonant modes and their frequencies depend on the optical thickness of the cavity layer: $\lambda/2$ cavities are single-mode while $p\lambda/2$ cavities with $p>1$ are multi-mode (see section II.2.3 for more details). The band structure now consists of a superposition of the core modes that propagate in air with a group velocity $\sim c$ and one or several cavity mode(s) that propagate in the cavity material of refractive index n with group velocity $\sim c/n$. It follows from coupled-mode theory that when a core mode and a cavity mode with same polarization (for $m=0$ modes) or same azimuthal symmetry ($\Delta m=0$, for $m\neq 0$ modes) interact, their dispersion relations form anti-crossings: the core mode transforms into the cavity mode and vice-versa with increasing frequency [Fig.67a,b].¹⁰²

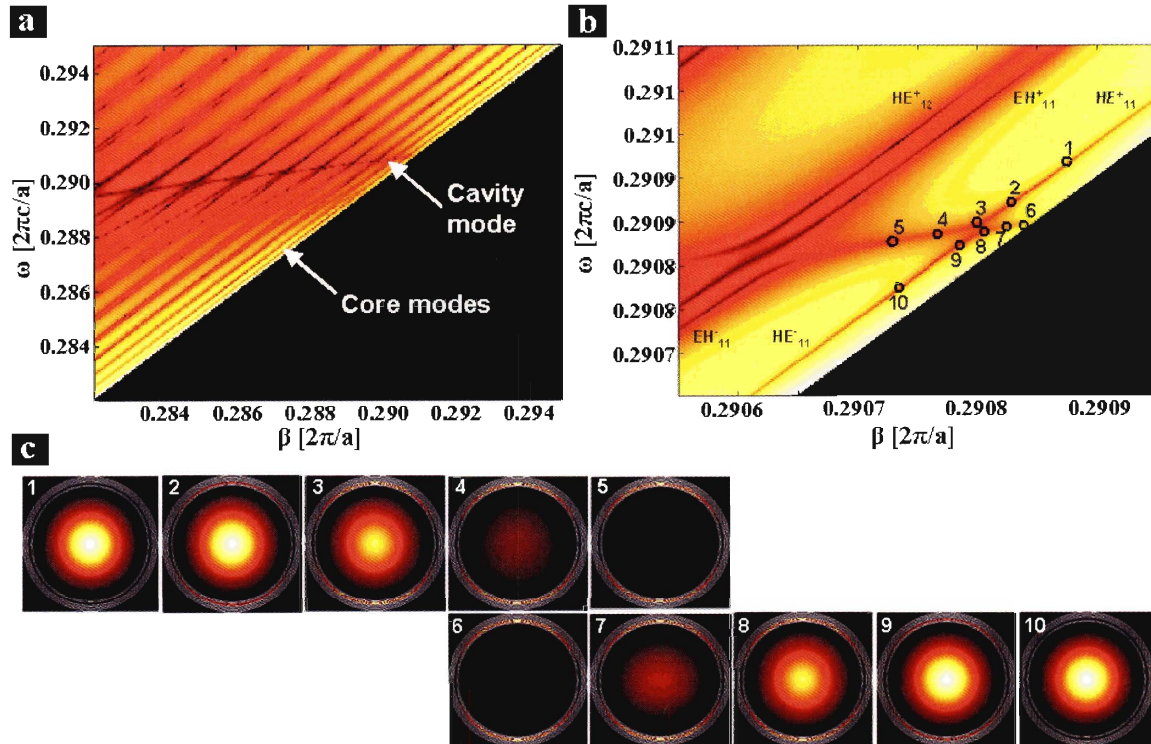


Figure 67: **a** Band-diagram of a transmission micro-cavity fiber consisting of 12 bilayers of As_2Se_3 and PES and a 10λ PES cavity located at the 7th layer from the core. The core size is equal to $70\ \mu\text{m}$. **b** Detail of the anti-crossing region resulting from the interaction between the HE_{11} core mode and the cavity resonant mode. $HE_{11}^{+(-)}$ refers to the dispersion relation of the core-mode at high (low) frequencies. **c** Coupling between the core and cavity modes and electric field profile across the anti-crossing region.

Fig.67c shows how the electric field profile of the HE_{11} mode evolves across the anti-crossing region as it couples to the cavity resonant mode. Note that these calculations were performed on a concentric multilayer structure with a perfectly square periodic refractive-index profile. The corresponding change in group velocity over the narrow interaction region lends itself to arbitrarily high dispersion values as seen in Fig 68.

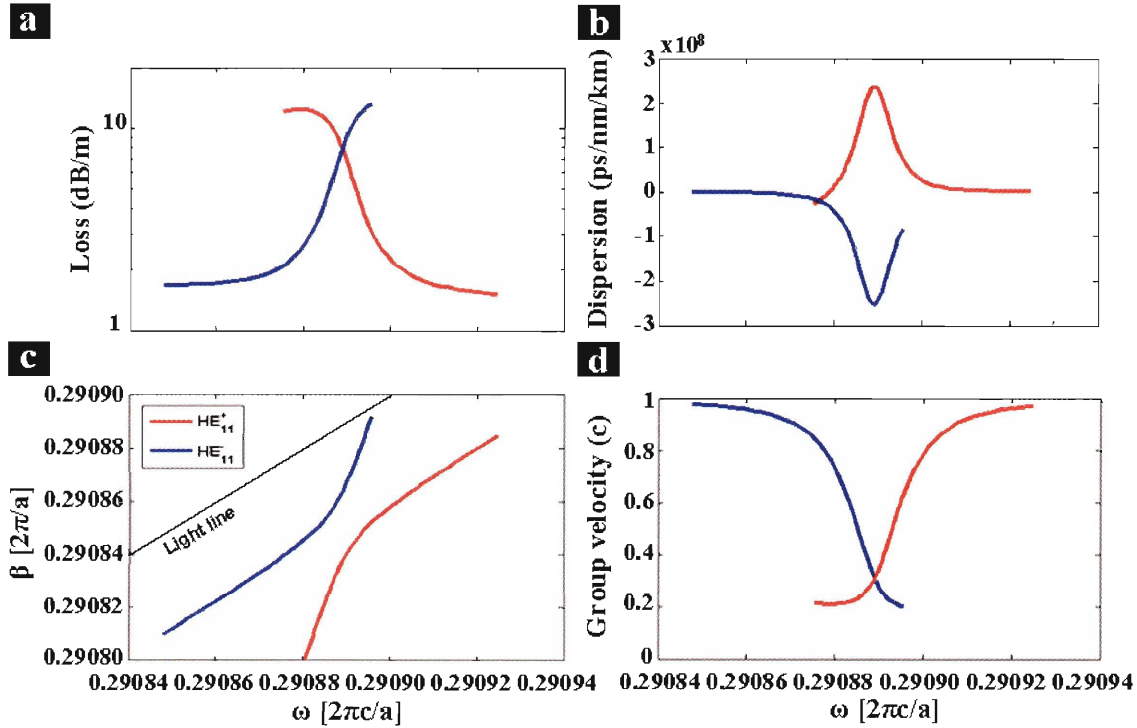


Figure 68: **a** Propagation losses, **b** group-velocity dispersion, **c** dispersion relation and **d** group velocity of the HE_{11} mode across the anti-crossing region. Dispersion parameters of $2 \cdot 10^8$ ps/nm/km and higher can theoretically be obtained via this mechanism.

The calculated dispersion spectrum [Fig 68b] exhibits anomalous dispersion ($D > 0$) and normal dispersion ($D < 0$) below and above the cavity resonance wavelength, respectively, with a zero-crossing at the cavity resonance wavelength. The expected increase in propagation losses near the resonance due to material absorption and radiation losses is less than 10 dB/m.

The table below summarizes the correlations between the amplitude and bandwidth of the group-velocity dispersion and four main design parameters: the location, thickness and refractive index of the cavity layer and the core size of the fiber.

Design parameters	Coupled-mode theory	
	Amplitude	Bandwidth
Cavity location	>0	<0
Cavity thickness	>0	<0
Cavity n	>0	<0
Fiber core size	>0	<0

The amplitude and the bandwidth of the group-velocity dispersion are always anti-correlated, which is a direct consequence of the definition of $D(\lambda)$ [Eq.119]. The amplitude of the dispersion increases as the coupling strength between the core mode and the cavity mode decreases due to a stronger curvature of the dispersion relation over a narrower spectral range. Since the coupling strength is proportional to the overlap between the electric field of the core and cavity modes, it follows that it decreases exponentially as the cavity layer is located deeper and further away from the core. It also decreases with the cavity layer thickness and the fiber core size [Fig.58b]. Finally, it can be seen from Eq.119 that D increases as the refractive index of the cavity material n increases due to a larger group-velocity mismatch with air. Note that even if the cavity material was air, its resonant mode would still be slower than any core guided modes due to its stronger confinement (see section VI.1.3).

VI.5 Dispersion measurements

We have fabricated several transmission fibers operating around $1.55\ \mu\text{m}$ with embedded micro-cavities. The fabrication process, described in section IV.1, allows us to place micro-cavities anywhere in the Bragg structure and to obtain very good layer uniformity and adhesion [Fig.69] as well as precise control over the operating wavelength of the fibers over hundreds of meter [Fig.60].

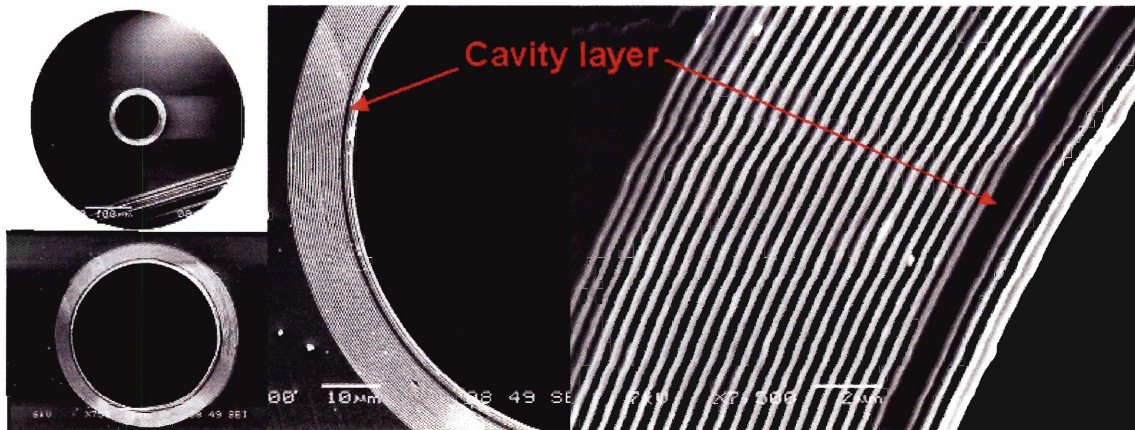


Figure 69: SEM imaging of the cross-section of a transmission Bragg fiber containing a micro-cavity. The $90\text{-}\mu\text{m}$ core fiber is made of As_2Se_3 and PES and contains a 2λ PES cavity located at the 10^{th} layer from the core. The fiber contains a total of 25 bilayers.

The total loss and relative group delay measurements were normalized with a reference measurement to eliminate any contribution from the silica fibers, the coupling elements and the SOA. This was confirmed by measuring the dispersion of 4 km of (Corning) LEAF fibers, which lead to an expected dispersion of 16 ps/nm. To align one of our hollow-core fibers for measurement, we first coupled the light of a (Ando AQ4321D) tunable laser (1.49-162 μm) delivered through a single-mode silica fiber with a pigtailed collimator to the fiber using a lens whose focal length was optimized for its core diameter (e.g. 1" focal length for a 80- μm core diameter). We optimized the input coupling by maximizing the transmitted power measured at the output of the 0.5-m-long fiber with a (Newport 818IG) InGaAs detector. At this point, we characterized the modal output of the fiber with an (Electrophysics 7290A) infrared camera and found that, away from resonances, it was nearly single-mode with a dominant contribution of the HE_{11} mode for core diameters below 100 μm [Fig.61a]. The fiber output was then coupled with a lens to another single-mode silica fiber with a pigtailed collimator. The total coupling losses were on the order of 15-20 dB, which was well compensated for by the SOA that amplified the signal by ~ 25 dB. Finally, the setup was connected to the ODA for measurements [Fig.70]. The modulation frequency f_m of the transmitted signal was optimized for each tested fiber to minimize smearing effects in the group delay measurements. Typically, we used $f_m = 300$ MHz, corresponding to a sideband separation below 5 pm, while the wavelength resolution was as low as 2 pm. The group-velocity dispersion spectrum $D(\lambda)$ was then obtained by fitting the measured relative group delay spectrum with one Lorentzian peak per resonance and a polynomial function and taking the derivative of the fitted expression with respect to wavelength (see Eq.119). Fig.71 shows two examples of such group delay measurements and dispersion calculations.

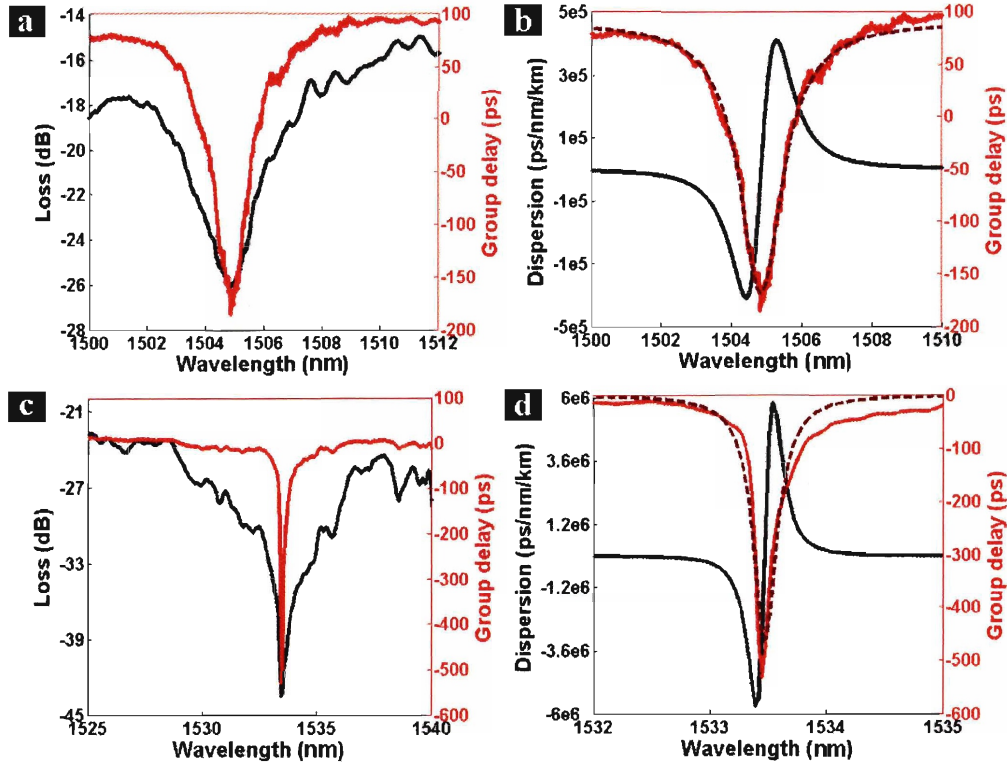


Figure 71: Loss and relative group delay measurements (a) for a 60- μm core fiber containing a $\lambda/2$ As_2S_3 cavity located at the 7th layer from the core and (c) for a 90- μm core fiber containing a $\lambda/2$ As_2S_3 cavity located at the 9th layer from the core. Both fibers contained 25 bilayers made of As_2S_3 and PEI. b and d show the fit of the corresponding group delay spectra with Lorentzian peaks and the resulting dispersion spectra.

These measurements demonstrate that very high dispersion (10^7 ps/nm/km and higher) is achievable near the cavity resonance wavelength. However, the measured dispersion spectra exhibit systematically anomalous dispersion ($D > 0$) and normal dispersion ($D < 0$) above and below the cavity resonance wavelength, respectively, which is the opposite of what we had predicted [Fig.68b]. This is quite surprisingly since it indicates an increase and not a decrease in the group velocity near the cavity resonance. In addition, the dispersion bandwidth, defined as the full width at half-maximum (FWHM) of the anomalous dispersion peak, is much narrower than expected. In order to accurately determine the propagation losses in the tested fibers at and off resonance, we performed cutback measurements. The losses at the maximum of dispersion were within 27 and 57 dB/m while the minimum propagation losses measured in the range of the tunable laser were within 2.5 and 20 dB/m, which is comparable to the losses measured in cavity free

transmission fibers at 1.5 μm . The 30 to 40 dB/m difference is significantly larger than the anticipated 10 dB/m, suggesting that additional loss mechanisms have not been accounted for in our previous calculations.

Before trying to explain the origin of the discrepancy between our initial predictions and our experimental results, let's first determine how the group-velocity dispersion measured in our fibers compares with the performance of other dispersion systems currently available. To do so, we define the ratio of the dispersion (ps/nm/km) to the propagating losses measured at the same wavelength (dB/km) or $D_{max}(\lambda')/L_{prop}(\lambda')$ (ps/nm/dB) as a figure of merit to account for the high losses associated with our dispersion mechanism. Treacy grating compressors,¹⁰⁴ which are widely used in chirped pulse amplification applications, offer figures of merit as high as 330 ps/nm/dB over a 5 nm bandwidth. In Fig.72a, we report the figure of merit of our fibers as a function of the dispersion bandwidth.

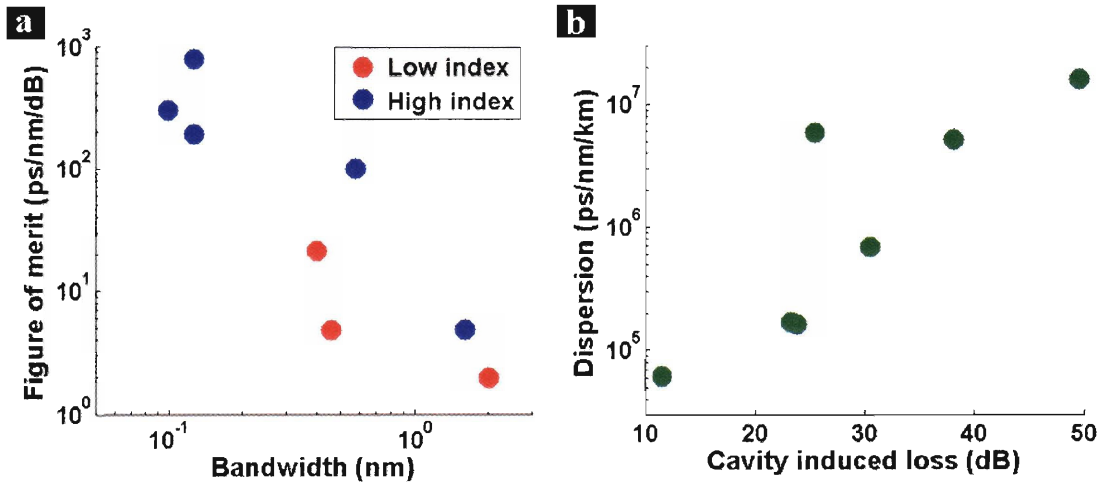


Figure 72: **a** Figure of merit as a function of bandwidth, **b** dispersion parameter D measured at the peak of anomalous dispersion as a function of the difference in propagation losses at and off resonance induced by the coupling to the cavity mode.

We measured a maximum figure of merit of 790 ps/nm/dB at 1533 nm, corresponding to $D = 2.36 \cdot 10^7$ ps/nm/km and $L = 30$ dB/m. This compares very favorably with typical diffraction grating compressors while providing all the benefits associated with a hollow-core fiber delivery system, in particular a low-form factor, high flexibility and the

possibility of achieving high peak power beyond the damage threshold of most materials.⁹⁹ The dispersion bandwidth measured in our fibers is typically sub-nanometer but can be increased at the cost of a decrease in the group-velocity dispersion [Fig.72a] as predicted by Eq.119.

To gain intuition into the potential mechanisms responsible for our seemingly surprising experimental results, we can study the correlations between the measured group-velocity dispersion and other performance or design parameters. Fig.72b shows that there exists a strong correlation between the group-velocity dispersion measured at the peak of anomalous dispersion (D) and the losses induced by the coupling to the cavity layer, which indicates that they could both be induced by a common mechanism. The increase in D with the cavity-layer location in the multilayer stack with respect to the fiber core [Fig.73a], i.e. with decreasing coupling strength, is expected from Eq.119 and confirms that it is indeed induced by a coupling between the core modes and the cavity layer.

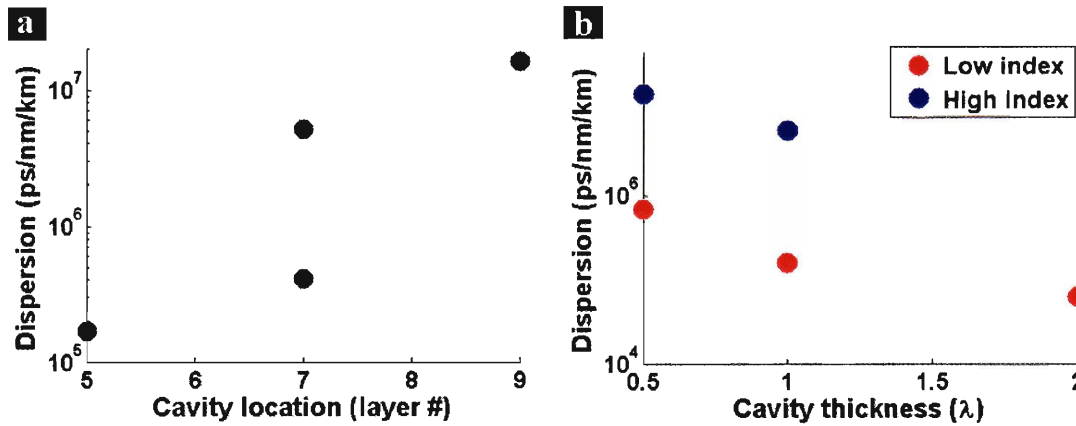


Figure 73: **a** Dispersion parameter D measured at the peak of anomalous dispersion as a function of the cavity layer location in the multilayer stack with respect to the fiber core, **b** D as a function of the cavity layer thickness.

More interestingly, we found that high-index cavities exhibit stronger dispersion than low-index cavities [Fig.72a, 73b]. Since we are measuring ‘fast light’ instead of ‘slow light’, the real part of the cavity material refractive index actually competes with this effect. In addition, the imaginary part of the cavity material refractive index is typically

lower for high-index cavities and should therefore lead to lower dispersion based on Fig.72b. There is however one more major difference between high-index and low-index resonant cavities, which is the electric field profile of their resonant modes. As seen in Fig.7, the amplitude of electric field at the interface between the cavity layer and the mirror layers vanishes in a low-index cavity while it reaches its maximum in a high-index cavity. This makes high-index cavities much more sensitive than low-index cavities to interface defects such as point defects, roughness, non-stoichiometric glass composition..., which can induce scattering of the resonant electromagnetic field and increase the radiation losses. If present, scattering is expected to be significant for the highly confined cavity resonant mode and to decrease as the cavity layer thickness increases. Furthermore, if this mechanisms is also responsible for the measured group-velocity dispersion as suggested by Fig.72b, fibers with thicker cavities would exhibit smaller D values, which is consistent with Fig.73b. While it does not prove anything, this analysis highlights two important conclusions: the measured dispersion is induced by a coupling between the core-modes and the cavity layer, and additional loss mechanisms in the cavity layer, still unidentified at this stage, could explain not only the increase in propagation losses near the cavity resonance but also the characteristics of the measured group-velocity dispersion spectra.

To study the effect of losses on the group-velocity dispersion in our fibers, we have recalculated the dispersion relation of the HE_{11} mode assuming an imaginary component of the cavity material refractive index ten times higher than the value used in Fig.67. The results are shown in Fig.74a.

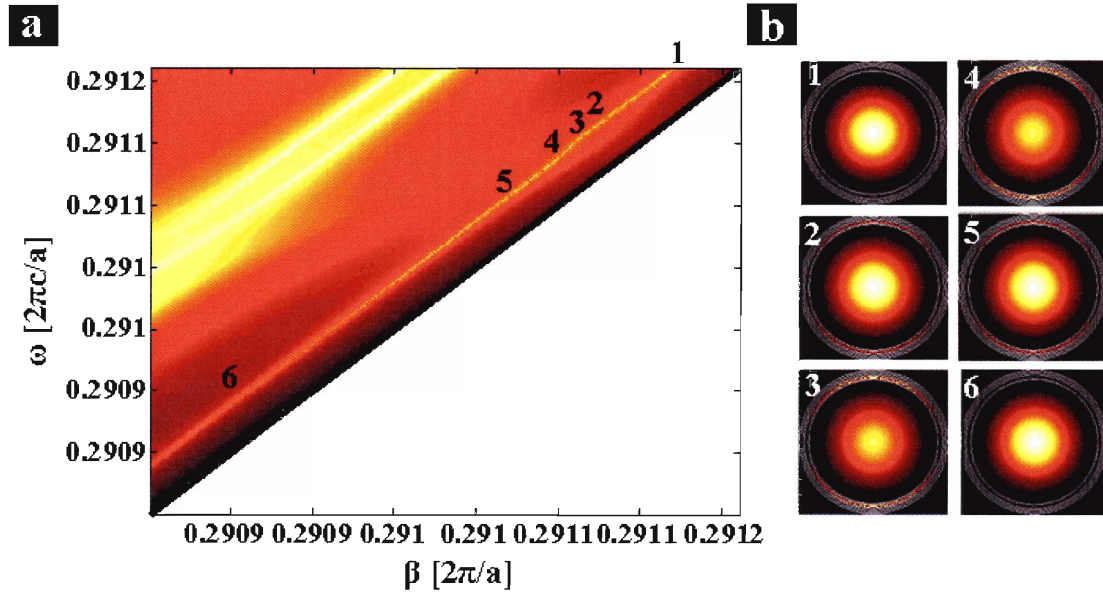


Figure 74: **a** Band diagram of a transmission micro-cavity fiber consisting of 12 bilayers of As_2Se_3 and PES and a 10λ PES cavity located at the 7th layer from the core. The core size is equal to $70\ \mu\text{m}$. The k value of the cavity material is set to 10^{-4} . **b** Electric field profile of the HE_{11} mode across the region of interaction with the cavity layer.

A very important finding is that the dispersion relation of the cavity mode has almost completely disappeared, indicating that the cavity mode can no longer be considered a confined propagating mode. As a result, no anti-crossing is observed since coupled-mode theory strictly applies to the coupling between two propagating modes and breaks down when the imaginary component of the axial wave-vector β of one of the modes becomes significant, comparable to its real component. It can be seen in Fig.74b that the HE_{11} mode is now mostly confined in the core of the fiber at all frequencies and that only a small fraction of its electric field couples to the cavity layer near resonance. This interaction induces a small perturbation of its dispersion relation, which leads to the change in group velocity shown in Fig.75a.

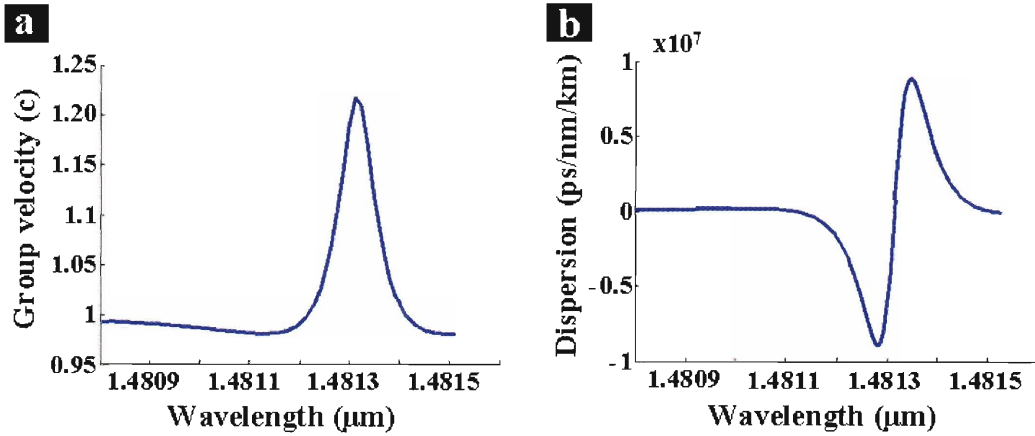


Figure 75: Group velocity (a) and group-velocity dispersion (b) for the HE_{11} mode across the interaction region.

The interaction of the HE_{11} mode with the cavity layer induces a significant increase of its group velocity to superluminal values. The resulting dispersion spectrum [Fig.75b] is consistent with our measurements performed on fibers with high figures of merit [Fig.72a]: this calculation predicts a maximum anomalous dispersion of $\sim 10^7$ ps/nm/km above the cavity resonant wavelength and a dispersion bandwidth of ~ 0.1 nm. To interpret these results, it is useful to define an effective refractive index for the fiber associated with the propagation of the HE_{11} mode. When the mode interacts with the cavity layer, the fraction of its electric field present in the cavity layer experiences high losses, which is equivalent to an increase in the k value of the effective refractive index of the fiber. It follows from Kramers-Kronig relations that this region of high absorption is also a region of high anomalous chromatic dispersion, i.e. $dn/d\lambda > 0$ [Fig.17], where superluminal velocities can be induced:

$$v_g = \frac{c}{n - \lambda \frac{dn}{d\lambda}} \quad (120)$$

This is merely the result of an approximation in the definition of the group velocity that is violated at a resonance when it no longer represents a physical velocity and is by no means a violation of Einstein's postulate.¹⁰⁵ The amplitude and bandwidth of the corresponding group-velocity dispersion depend obviously on the amount of loss induced by the cavity layer, which is consistent with the correlation observed in Fig.72b. Note

that while we only considered an increase in material losses for convenience, an increase in radiation losses would lead to a similar result since both mechanisms can be modeled as an absorption line from the point of view of the core modes.

Interestingly, a very similar dispersive effect is predicted at the band-gap edges where resonant tunneling through the multilayer structure provides a highly efficient coupling mechanism to non-confined radiative modes [Fig.76].

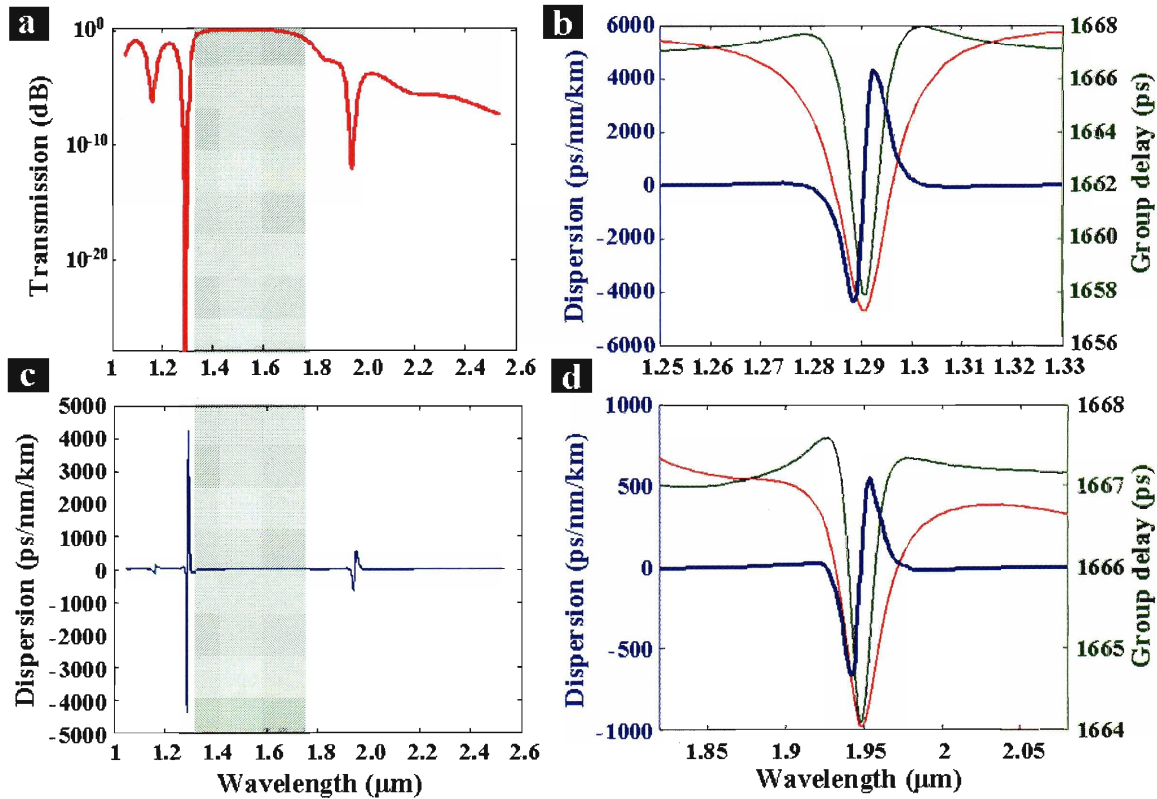


Figure 76: **a** Transmission and **c** group-velocity dispersion spectra for the HE_{11} mode in a 70- μm core fiber consisting of 6 bilayers of As_2Se_3 and PES and containing a 10λ PES cavity located at the 7th layer from the core. The photonic band-gap is highlighted in green. **b**, **d** Details of the transmission (red), group delay (green) and group-velocity dispersion (blue) spectra at the upper and lower band-edges, respectively.

These calculations show that superluminal group-velocities are also predicted for the HE_{11} mode at the high and low frequency band-gap edges resulting in a sign of the group-velocity dispersion identical to the one measured at the cavity resonance. The amplitude of the dispersion increases exponentially with the number of bilayers ($D \sim 100,000$

ps/nm/km at the high frequency edge for a 14 bilayer structure) and can reach very high values. Fig.77a offers a direct comparison between the group delay measured at the high-frequency band-edge and at the cavity resonance.

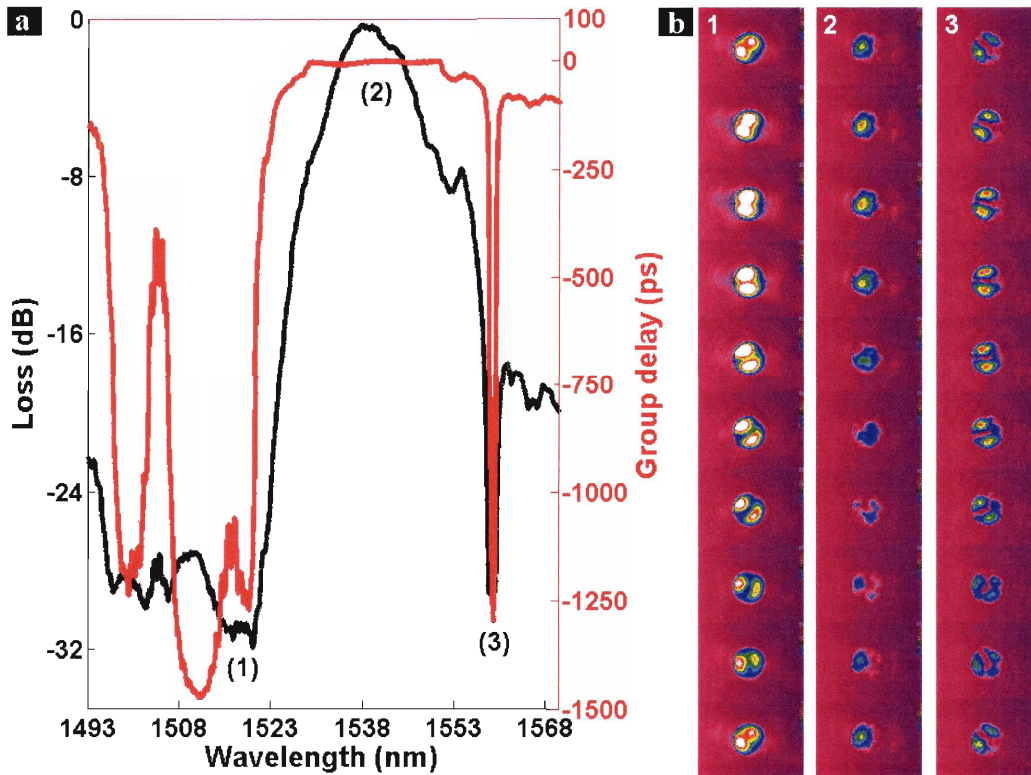


Figure 77: **a** Loss and group delay measurements at the high-frequency band-edge and at the cavity resonance, **b** mode profile at the band-edge (1), in the band-gap and off resonance (2) and at resonance (3) observed after a linear polarizer with an IR camera as a function of the polarizer angle (0° to 180° from top to bottom). (1) shows the TE_{01} mode, (2) exhibits a dominant HE_{11} mode and weak contribution of higher-order modes, (3) is characteristic of a high-order mode. The relative intensity between the modes is meaningless because the intensity of the source was adjusted not to saturate the camera.

The sign, amplitude and bandwidth of the measured group-velocity dispersion at the band-edge agree well with our calculations for the HE_{11} mode [Fig.76b] and result from an increase in the group velocity similar to the one observed at the cavity resonance, though induced by a different mechanism. However, the slope of the group delay near the cavity resonance is steeper than at the band-edge, which leads to stronger group-velocity dispersion, while the propagation losses are lower, resulting in a significantly higher figure of merit. Another important difference is that the micro-cavity provides a

mode-specific dispersion mechanism. Indeed, at the band-edge, most of the core modes couple to radiative modes and the TE_{01} mode is the only one that survives [Fig77b(1)] thanks to its larger effective band-gap [Fig.59b]. At the cavity resonance however, the HE_{11} mode alone couples strongly to the micro-cavity while other modes do not [Fig77b(3)].

We have shown that our experimental results can be well explained by unaccounted losses in the cavity layer but we have not yet identified their origin(s). This is a challenging problem because many different mechanisms may be involved. Nevertheless, there are a certain number of evidence that suggests that scattering is one additional source of losses in our fibers. First, as mentioned in section VI.2.3, the propagation losses measured in 1.5- μm fibers are similar to the ones measured in 10.6- μm fibers, indicating that a wavelength-sensitive loss mechanism other than material absorption is involved. SEM imaging of the first chalcogenide glass layer in these fibers [Fig.78] further reveals that it could be a scattering mechanism induced by interface defects, resulting in additional radiation losses.

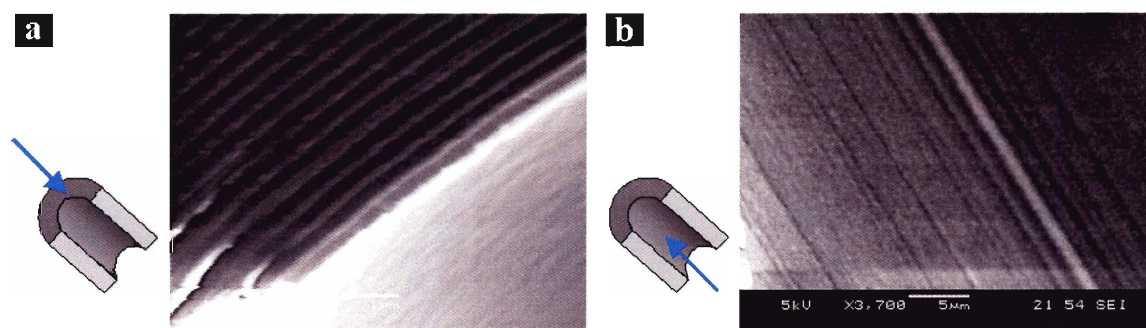


Figure 78: View of the first chalcogenide glass layer in a 1.5- μm transmission fiber in the axial direction (a) and in the radial direction (b). Surface defects include roughness, point defects including the inner seam and possibly non-stoichiometric composition of the chalcogenide glass. (Courtesy of J.-F. Viens)

Such a scattering mechanism would affect the strongly confined cavity mode even more dramatically. Direct measurements of the power radiated out of the fibers show indeed a sharp increase near the cavity resonance wavelength as shown in Fig.79a.

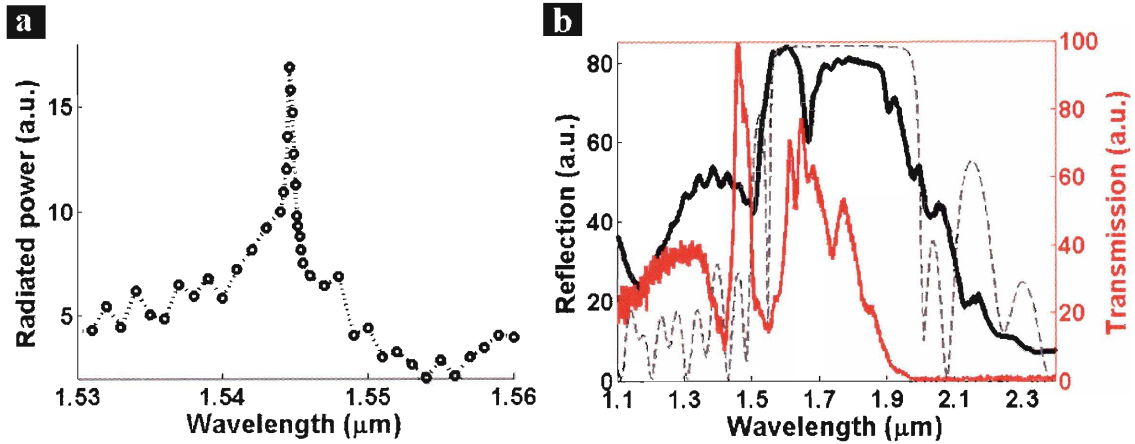


Figure 79: a Radiation loss spectrum, **b** FTIR transmission (red) and external reflection (black) measurements for a 90- μm core fiber made of As_2S_3 and PEI and containing a $\lambda/2$ As_2S_3 cavity located at the 5th layer from the core. The corresponding external reflection spectrum calculated at normal incidence is plotted with a dashed grey line.

The bandwidth of the radiated power peak is similar to the measured dispersion bandwidth, further suggesting that the two effects are correlated.

Scattering can theoretically be reduced by decreasing the refractive index contrast between the high and low refractive index layers, at the cost of a reduction in the width of the photonic band-gap. However, when comparing the respective positions of the transmission spectrum and the external reflection spectrum measured in fibers made of As_2S_3 and PEI [Fig.79b], it appears that the cavity resonant wavelength at grazing incidence is in the vicinity of the high-frequency band-edge near normal incidence. Therefore a narrower band-gap could instead result in higher radiation losses. As mentioned earlier, increasing the cavity layer thickness is another path towards decreasing the amount of scattering of the cavity resonant mode if it is purely induced by interface defects. We have fabricated fibers containing $10\text{-}\lambda$ low-index micro-cavities and observed a significant reduction in the dispersion amplitude but no switch in its sign. Larger cavities could easily be fabricated but material absorption would then become the dominant loss mechanism. Therefore reducing the losses in our fibers seems to require the design of structures that are more perturbation-tolerant¹⁰⁶ and improvements in the fabrication process in order to produce layers and interfaces of much higher optical quality.

VI.6 Mechanical tuning of highly dispersive hollow core fibers

As mentioned in the introduction, certain applications require very high or very low group-velocity dispersion and others require a very specific dispersion parameter. While it would be possible to make a fiber with a pre-specified dispersion parameter at a given wavelength, a much more practical solution is to explore the possibility of dynamically tuning the dispersion parameter. A group-velocity-dispersion tuning range of +/-450 ps/nm/km has been demonstrated in transmissive in-fiber Fabry-Perot etalons controlled thermally or with strain.¹⁰⁷ We have shown previously in fibers designed for external reflection that the thickness of the Bragg layers can be reduced using a mechanical tuning scheme (Section V.2)³⁹ or that the refractive index of embedded Fabry-Perot cavities can be modified using an all-optical tuning scheme (section V.3),⁴⁴ both strategies leading to a reversible shift of the cavity resonant mode. Mechanical tuning however is easier to implement in transmission fibers because it leads to a uniform shift along the length of the fiber (neglecting edge effects at the fiber's ends) as shown in section VI.3. In order to implement the mechanical tuning scheme with our highly dispersive photonic band-gap fibers, we fixed both ends of the tested fiber with epoxy and mounted the output end as well as the coupling elements on a x-stage that could be moved along the fiber axis [Fig.70]. In section V.2.3 we have shown that the maximum reversible normalized shift $\Delta\lambda/\lambda$ in our fibers was equal to -0.5% under 1.2% axial strain.³⁹ Here, we demonstrate a spectral shift by -5nm under 0.7% axial strain [Fig.80], resulting in a maximum change in dispersion from $+450,000$ ps/nm/km to $-450,000$ ps/nm/km anywhere between 1551 and 1554 nm.

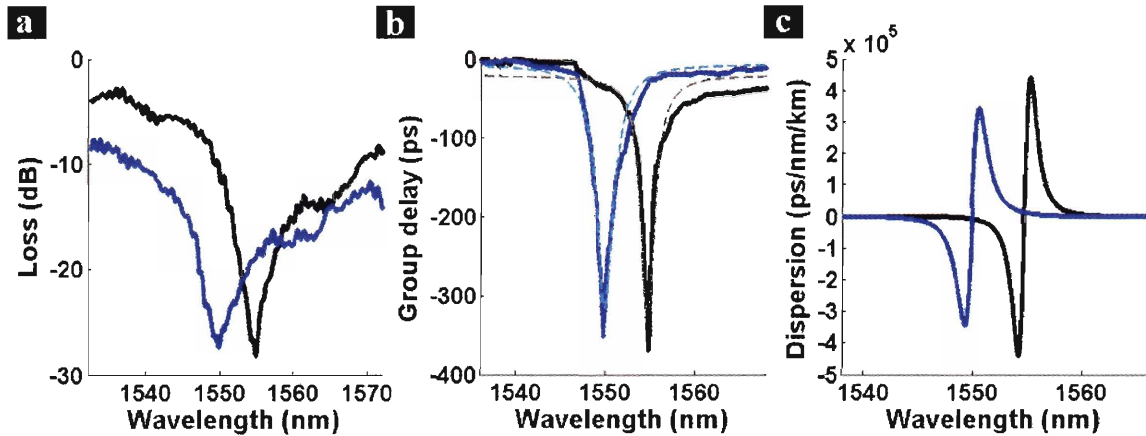


Figure 80: Shift of the loss spectrum (a), group delay spectrum (b) and dispersion spectrum (c) under 0.7% applied axial strain.

These fibers offer a unique solution for precise zero-dispersion transmission and dispersion compensation at multiple wavelengths, where not only the dispersion coefficient but also its derivative with respect to wavelength must be controlled. Furthermore, adaptive dispersion compensation combined with in-service monitoring of the group-velocity dispersion¹⁰⁸ could enable dynamic allocation of bit rates and a more efficient use of the current optical network. Mechanical tuning of our fibers in particular would offer response times on the order of or lower than a millisecond, well below what other tuning mechanisms, such as thermal effects in fiber Bragg gratings, can achieve.

VI.7 Future directions

Further studies need to be conducted to demonstrate group-velocity dispersion based on the coupling between core modes and cavity modes, which would be associated with much lower propagation losses and therefore much higher figures of merit. This clearly involves identifying and reducing the loss mechanisms in our fibers by improving the fabrication process. If successful, a step further would be to slow light down even more dramatically by inducing diffraction gratings in fibers containing As_2Se_3 microcavities based on the metastable photodarkening effect. Slow light is interesting in that it can be coupled with other slow particles, eventually electrons, opening the possibility for very important fundamental research.

The use of our fibers for chirped-pulse amplification is another exciting opportunity. Achieving very high peak power beyond the damage threshold of nearly any material opens the door for non-thermal material ablation and a variety of entirely new high precision applications. The development of short-pulse emission at wavelengths near 1 μm in particular is motivated by biological and medical applications. However, controlling non-linear effects in the fibers becomes critical and represents an additional challenge since chalcogenide glasses are characterized by relatively high non-linear coefficients (~ 400 times higher in As_2Se_3 and ~ 90 times higher in As_2S_3 than in silica).

Finally, other dispersion mechanisms could be studied in these fibers. In particular, all hybrid modes, such as the HE_{11} mode, are sensitive to polarization-mode dispersion (PMD). PMD and group-velocity dispersion (GVD) are typically strongly correlated but they can be decoupled by proper design of the fiber structure.¹⁰⁹ This offers an additional degree of freedom to further optimize the performance of our fibers.

VII Conclusion

It is safe to say that the range of materials and structures that are amenable to our approach will increase and that the repertoire of novel applications will expand. While we have explored the use of several polymers in our fibers, there remain many other families of functional polymers that are of interest to explore new tuning mechanisms and are expected to be compatible with our approach, such as conductive or piezoelectric polymers.

Although we have presented results related to the photodarkening properties of chalcogenide glasses, these glasses are further characterized by high optical non-linear coefficients. It has been found that As_2Se_3 , in particular, has two to three orders of magnitude higher Kerr non-linearity than silica glass. Since this glass is highly transparent in the mid-infrared, where silica glass is opaque, it is expected that non-linear optical studies, such as super-continuum generation and ultra-fast optical tuning, will flourish.

The interplay between material properties, structure integration, and fabric construction is just beginning and promises to be an exciting field for fundamental and applied research besides many applications.

1. Russell P. "Photonic crystal fibers" *Science* **299**, 358-62 (2003).
2. Knight J. C. "Photonic crystal fibres" *Nature* **424**, 847-851 (2003).
3. Fink Y., Ripin D. J., Fan S., Chen C., Joannopoulos J. D. and Thomas E. L. "Guiding optical light in air using an all-dielectric structure" *Journal of Lightwave Technology* **17**, 2039-41 (1999).
4. Joannopoulos J. D., Meade R. D. and Winn J. N. *Photonic Crystals - Molding the flow of Light* (Princeton University Press, Princeton, 1995).
5. Fink Y., Winn J. N., Fan S., Chen C., Michel J., Joannopoulos J. D. and Thomas E. L. "A Dielectric Omnidirectional Reflector" *Science* **282**, 1979-1682 (1998).
6. Yeh P. *Optical Waves in Layered Media* (ed. Goodman, J. W.) (John Wiley & Sons, New York, 1988).
7. Johnson S. G., Ibanescu M., Skorobogatiy M., Weisberg O., Engeness T. D., Soljacic M., Jacobs S. A., Joannopoulos J. D. and Fink Y. "Low-loss asymptotically single-mode propagation in large-core OmniGuide fibers" *Optics Express* **9**, 748-779 (2001).
8. Yeh P., Yariv A. and Hong C.-S. "Electromagnetic propagation in periodic stratified media. I. General theory" *Journal of the Optical Society of America* **67**, 423-38 (1977).
9. Born M. and Wolf E. *Principles of optics* (Pergamon, 1970).
10. Temelkuran B., Thomas E. L., Joannopoulos J. D. and Fink Y. "Low-loss infrared dielectric material system for broadband dual-range omnidirectional reflectivity" *Optics Letters* **26**, 1370-1372 (2001).
11. Jackson J. D. *Classical Electrodynamics* (John Wiley & Sons, New York, 1975).
12. Saleh B. E. A. and Teich M. C. *Fundamentals of photonics* (John Wiley & Sons, New York, 1991).
13. Bendickson J. M., Scalora M. and Dowling J. P. "Analytic expressions for the electromagnetic mode density in finite, one-dimensional, photonic band-gap structures" *Proceedings of the 1996 6th Quantum Electronics and Laser Science Conference (QELS)* **9**, 192 (1996).
14. Shapira O., Kuriki K., Orf N. D., Benoit G., Abouraddy A. F., Viens J.-F., Brewster M. M., Rodriguez A., Ibanescu M., Joannopoulos J. D. and Fink Y. "Polarisation Controlled Surface-Emitting Polymer Fibre Lasers" (2006).
15. Foteinopoulou S., Economou E. N. and Soukoulis C. M. "Refraction in media with a negative refractive index" *Physical Review Letters* **90**, 107402-1 (2003).
16. Chen X. L., He M., Du Y., Wang W. Y. and Zhang D. F. "Negative refraction: an intrinsic property of uniaxial crystals" *Physical Review B (Condensed Matter and Materials Physics)* **72**, 113111-1 (2005).
17. Benoit G. and Fink Y., MIT *Electronic database*: <http://mit-pbg.mit.edu/Pages/DataBase.html>
18. Harland G. Tompkins W. A. M. *Spectroscopic Ellipsometry and Reflectometry - A user's guide* (John Wiley & Sons, Inc., 1999).
19. Aspnes D. E. "Fourier transform detection system for rotating-analyzer ellipsometers" *Optics Communications* **8**, 222-5 (1973).
20. Kittel C. *Introduction to Solid State Physics* (ed. Sons, W.) (2005).

21. Ashcroft N. W. and Mermin N. D. *Solid State Physics* (Saunders college, Philadelphia, 1976).
22. Urbach F. "The Long-Wavelength Edge of Photographic Sensitivity and of the Electronic Absorption of Solids" *Phys. Rev.*, 1324 (1953).
23. Moazzami K., Phillips J., Lee D., Krishnamurthy S., Benoit G. and Fink Y. "Detailed Study of Above Bandgap Optical Absorption in HgCdTe" *Journal of Electronic Materials* **34**, 773-778 (2005).
24. Forouhi A. R. and Bloomer I. "Optical dispersion relations for amorphous semiconductors and amorphous dielectrics" *Physical Review B* **34**, 7018-26 (1986).
25. Sheik-Bahae M. *Nonlinear Optics Basics. Kramers-Kronig Relations in Nonlinear Optics*. (ed. Guenther, R. D.) (Academic Press, Amsterdam, 2005).
26. Adachi S. "Model dielectric constants of Si and Ge" *Physical Review B (Condensed Matter)* **38**, 12966-76 (1988).
27. Adachi S. "Model dielectric constants of GaP, GaAs, GaSb, InP, InAs, and InSb" *Physical Review B (Condensed Matter)* **35**, 7454-63 (1987).
28. Bruggeman D. A. G. "Physical constants of mixtures" *Physikalische Zeitschrift* **37**, 906-912 (1936).
29. Garnett J. C. M. "Colours in metal glasses and in metallic films" *Philosophical Transactions of the Royal Society of London* **203**, 385-420 (1904).
30. Garnett J. C. M. "Colours in metal glasses, in metallic films and in metallic solutions. II" *Philosophical Transactions of the Royal Society of London* **205**, 237-288 (1905).
31. Sheng P. "Theory for the dielectric function of granular composite media" *Physical Review Letters* **45**, 60-3 (1980).
32. Marquardt D. "An Algorithm for Least-Squares Estimation of Nonlinear Parameters" *SIAM J. Appl. Math.* **11**, 431-441 (1963).
33. Savage J. A. "Optical properties of chalcogenide glasses" *Journal of Non-Crystalline Solids* **47**, 101-116 (1982).
34. Kuptsov A. H. and Zhizhin G. N. *Handbook of fourier transform Raman and infrared spectra of polymers* (Elsevier, New York, 1998).
35. Nair P. K., Cardoso J., Daza O. G. and Nair M. T. S. "Polyethersulfone foils as stable transparent substrates for conductive copper sulfide thin film coatings" *Thin Solid Films* **401**, 243-250 (2001).
36. Borisova Z. U. *Glassy semiconductors* (Plenum Press, New York, 1981).
37. Mark J. E. *Polymer data handbook* (ed. Mark, J. E.) (Oxford University Press, New York, 1999).
38. Weber M. F., Stover C. A., Gilbert L. R., Nevitt T. J. and Ouderkirk A. J. "Giant birefringent optics in multilayer polymer mirrors" *Science* **287**, 2451-5 (2000).
39. Benoit G., Hart S. D., Temelkuran B., Joannopoulos J. D. and Fink Y. "Static and Dynamic Properties of Optical Microcavities in Photonic Bandgap Yarns" *Advanced Materials* **15**, 2053-2056 (2003).
40. Mitsuteru Kimura K. O., Toshihiko Miyamoto. "Tunable multilayer-film distributed-Bragg-reflector filter" *J. Appl. Phys.* **50**, 1222-1225 (1978).

41. H.G. Limberger A. I., R.P. Salathe, L.A. Everall, K.E. Chisholm, I. Bennion. in *Proc. 25th European Conf. Optic. Commun.* 156-159 (1999).
42. T. Inui T. K., M. Nakazawa. "Highly efficient tunable fiber Bragg grating filters using multilayer piezoelectric transducers" *Optics Communications* **190**, 1-4 (2001).
43. Shchurova T. N. and Savchenko N. D. "Correlation between mechanical parameters for amorphous chalcogenide films" *J. Optoelectron. Adv. Mater.* **3**, 491-498 (2001).
44. Benoit G., Kuriki K., Viens J.-F., Joannopoulos J. D. and Fink Y. "Dynamic all-optical tuning of transverse cavity modes in photonic bandgap fibers" *Optics Letters* **30**, 1620-1622 (2005).
45. Neufville J. P. D., Moss S. C. and Ovshinsky S. R. "Photostructural transformations in amorphous As_2Se_3 and As_2S_3 films" *Journal of Non-Crystalline Solids* **13**, 191-223 (1973).
46. Tanaka K. and Hamanaka H. "Photostructural change and related phenomena in chalcogenide glasses" *Solid State Physics* **15**, 423-8 (1980).
47. Ganjoo A. and Shimakawa K. "Transient and metastable photodarkening in amorphous chalcogenides" *J. Optoelectron. Adv. Mater.* **3**, 221-226 (2001).
48. Popescu M., Sava F., Lorinczi A., Iovu M. S., Shutov S., Hoyer W. and Bradaczek H. "The effect of ultraviolet radiation on the structure of non-crystalline chalcogenides" *J. Optoelectron. Adv. Mater.* **2**, 667-670 (2000).
49. Larmagnac J. P. and Grenet J. "Photo-Dependence of Sub T_g Relaxation in a-Se Thin Films" *Philosophical Magazine B* **45**, 627 (1982).
50. Kolomiets B. T. and Lyubin V. M. "Reversible Photoinduced Changes in the Properties of Chalcogenide Vitreous Semiconductors" *Mater Res Bull* **13**, 1343 (1978).
51. Popta A. C. v., deCorby R. G., Haugen C. J., Robinson T. and McMullin J. N. "Photoinduced refractive index change in As_2Se_3 by 633 nm illumination" *Optics Express* **10**, 639-644 (2002).
52. Pfeiffer G., Paesler M. A. and Agarwal S. C. "Reversible photodarkening of amorphous arsenic chalcogens" *Journal of Non-Crystalline Solids* **130**, 111-143 (1991).
53. Lyubin V. M. and Tikhomirov V. K. "Photodarkening and photoinduced anisotropy in chalcogenide vitreous semiconductor films" *Journal of Non-Crystalline Solids* **114**, 133-5 (1989).
54. Shimakawa K. and Elliott S. R. "Reversible photoinduced change of AC conduction in amorphous As_2S_3 films" *Physical Review B (Condensed Matter)* **38**, 12479-82 (1988).
55. Li J. and Drabold D. A. "Direct Calculation of Light-Induced Structural Change and diffusive Motion in Glassy As_2Se_3 " *Physical Review Letters* **85** (2000).
56. Pfeiffer G., Brabec C. J., Jefferys S. R. and Paesler M. A. "Structural models of glassy As_2S_3 : intermediate-range order and photostructural changes" *Physical Review B (Condensed Matter)* **39**, 12861-71 (1989).

57. Bishop S. G. and Shevchik N. J. "Densities of valence states of amorphous and crystalline As₂S₃, As₂Se₃, and As₂Te₃: X-ray photoemission and theory" *Physical Review B (Solid State)* **12**, 1567-78 (1975).
58. Vanderbilt D. and Joannopoulos J. D. "Theory of defect states in glassy As₂Se₃." *Physical Review B* **23** (1981).
59. Tanaka K. "Photodarkening in amorphous As₂S₃ and Se under hydrostatic pressure" *Physical Review B* **30**, 4549-4554 (1984).
60. Tanaka K. "Configurational and Structural Models for Photodarkening in Glassy Chalcogenides" *Japanese Journal of Applied Physics* **25**, 779-786 (1986).
61. Hautala J., Ohlsen W. D. and Taylor P. C. "Optically induced electron-spin resonance in As_xS_{1-x}" *Physical Review B (Condensed Matter)* **38**, 11048-60 (1988).
62. Averyanov V. L., Kolobov A. V., Kolomiets B. T. and Lyubin V. M. "A model of photostructural changes in chalcogenide vitreous semiconductors. II. Experimental results" *Journal of Non-Crystalline Solids* **45**, 343-53 (1981).
63. Petkov K. and Ewen P. J. S. "Photoinduced changes in the linear and non-linear optical properties of chalcogenide glasses" *Journal of Non-Crystalline Solids* **249**, 150-9 (1999).
64. Ducharme S., Hautala J. and Taylor P. C. "Photodarkening profiles and kinetics in chalcogenide glasses" *Physical Review B (Condensed Matter)* **41**, 12250-9 (1990).
65. Shimakawa K., Yoshida N., Ganjoo A. and Kuzukawa Y. "A model for the photostructural changes in amorphous chalcogenides" *Philosophical Magazine Letters* **77**, 153-158 (1998).
66. Tanaka K., Kyohya S. and Odajima A. "Anomaly of the thickness dependence of photodarkening in amorphous chalcogenide films" *Electronics And Optics* **111**, 195-199 (1984).
67. Iovu M. S., Shutov S. d. and Popescu M. "Relaxation of photodarkening in amorphous As-Se films doped with metals." *Journal of Non-Crystalline Solids* **299-302**, 924-928 (2002).
68. Hubbard J. "Electron correlations in narrow energy bands" *Proceedings of the Royal Society of London, Series A (Mathematical and Physical Sciences)* **276**, 238-257 (1963).
69. Anderson P. W. "Model for the electronic structure of amorphous semiconductors" *Physical Review Letters* **34**, 953-5 (1975).
70. Street R. A. and Mott N. F. "States in the gap in glassy semiconductors" *Physical Review Letters* **35**, 1293-6 (1975).
71. Kastner M., Adler D. and Fritzsche H. "Valence-Alternation Model for Localized Gap States in Lone-Pair Semiconductors" *Physical Review Letters* **37**, 1504-1507 (1976).
72. Elliott S. R. "A unified model for reversible photostructural effects in chalcogenide glasses" *Journal of Non-Crystalline Solids* **81**, 71-98 (1986).
73. Cardinal T., Richardson K. A., Shim H., Schulte A., Beatty R., Le Foulgoc K., Meneghini C., Viens J. F. and Villeneuve A. "Non-linear optical properties of

- chalcogenide glasses in the system As-S-Se" *Journal of Non-Crystalline Solids* **256-257**, 353-360 (1999).
74. Smektala F., Quemard C., Leneindre L., Lucas J., Barthelemy A. and De Angelis C. "Chalcogenide glasses with large non-linear refractive indices" *Journal of Non-Crystalline Solids* **239**, 139-42 (1998).
 75. Agarwal S. C. "Nature of localized states in amorphous semiconductors-a study by electron spin resonance" *Physical Review B (Solid State)* **7**, 685-91 (1973).
 76. Yang C. Y., Paesler M. A. and Sayers D. E. "Measurement of local structural configurations associated with reversible photostructural changes in arsenic trisulfide films" *Physical Review B (Condensed Matter)* **36**, 9160-7 (1987).
 77. Ganjoo A., Shimakawa K., Kitano K. and Davis E. A. "Transient photodarkening in amorphous chalcogenides" *Journal of Non-Crystalline Solids* **299**, 917 (2002).
 78. Swanepoel R. "Determination of the thickness and optical constants of amorphous silicon" *J. Phys. E* **16**, 1241-1222 (1983).
 79. Petkov K. "Compositional dependence of the photoinduced phenomena in thin chalcogenide films" *Journal of Optoelectronics and Advanced Materials* **4**, 611-629 (2002).
 80. Ganjoo A. and Shimakawa K. "Dynamics of photodarkening in amorphous chalcogenides" *Journal of Optoelectronics and Advanced Materials* **4**, 595-604 (2002).
 81. SciVision *Electronic Handbook of Optical Constants of Solids* (Academic Press 1999)
 82. Aoyagi Y., Segawa Y., Namba S., Suhara T., Nishihara H. and Gamo H. "Dynamic behavior of the photodarkening process in As₂S₃ chalcogenide glass" *Physica Status Solidi A* **67**, 669-76 (1981).
 83. Russell P. "Photonic crystal fibers" *Science* **299**, 358-362 (2003).
 84. Croitoru N., Inberg A., Oksman M., Ben-David M. and Shefer A. in *Specialty Fiber Optics for Biomedical and Industrial Applications* 30-5 (SPIE-Int. Soc. Opt. Eng, San Jose, CA, USA, 1997).
 85. Temelkuran B., Hart S. D., Benoit G., Joannopoulos J. D. and Fink Y. "Wavelength-scalable hollow optical fibres with large photonic bandgaps for CO₂ laser transmission" *Nature* **420**, 650-653 (2002).
 86. Fatemi F. K., Bashkansky M. and Moore S. "Side-illuminated hollow-core optical fiber for atom guiding" *Optics Express* **13**, 4890-4895 (2005).
 87. Pfeifer T., Kemmer R., Spitzenpfeil R., Walter D., Winterfeldt C., Gerber G. and Spielmann C. "Spatial control of high-harmonic generation in hollow fibers" *Optics Letters* **30**, 1497-1499 (2005).
 88. Bhardwaj P., Gregory O. J., Morrow C., Gu G. and Burbank K. "Performance of a dielectric-coated monolithic hollow metallic waveguide" *Materials Letters* **16**, 150-6 (1993).
 89. Nubling R. K. and Harrington J. A. "Hollow-waveguide delivery systems for high-power, industrial CO₂ lasers" *Applied Optics* **35**, 372-80 (1996).
 90. Yeh P., Yariv A. and Marom E. "Theory of Bragg fiber" *Journal of the Optical Society of America* **68**, 1196-1201 (1978).

91. Baggett J. C., Petrovich M. N., Hayes J. R., Finazzi V., Poletti F., Amezcua R., Broderick N. G. R., Richardson D. J., Monro T. M., Salter P. L., Proudley G. and O'Driscoll E. J. in *Nanophotonics for Communication: Materials and Devices II* 601709 (International Society for Optical Engineering, Bellingham WA, Boston, 2005).
92. Kuriki K., Shapira O., Hart S. D., Benoit G., Kuriki Y., Viens J. F., Bayindir M., Joannopoulos J. D. and Fink Y. "Hollow multilayer photonic bandgap fibers for NIR applications" *Optics Express* **12**, 1510-1517 (2004).
93. Dal J. and Harrington J. A. "High-peak-power, pulsed CO₂ laser light delivery by hollow glass waveguides" *Applied Optics* **36**, 5072-7 (1997).
94. Shapira O., Abouraddy A. F., Joannopoulos J. D. and Fink Y. in *2005 Conference on Lasers and Electro-Optics (CLEO), 22-27 May 2005* 1551-3 BN - 1 55752 795 4 (IEEE, Baltimore, MD, USA, 2005).
95. Ibanescu M., Johnson S. G., Soljacic M., Fink Y., Weisberg O., Engeness T. D., Jacobs S. A., Joannopoulos J. D. and Skorobogatiy M. "Analysis of mode structure in hollow dielectric waveguide fibers" *Physical Review E* **67**, 46608-1 (2003).
96. Cohen L. G., Lin C. and French W. G. "Tailoring zero chromatic dispersion into the 1.5-1.6 micron low-loss spectral region of single-mode fibres" *Electronics Letters* **25**, 29-30 (1989).
97. Zhu B., Nelson L. E., Stulz S., Gnauck A. H., Doerr C., Leuthold J., Gruner-Nielsen L., Pedersen M. O., Kim J. and Lingle Jr. R. L. "High Spectral Density Long-Haul 40-Gb/s Transmission Using CSRZ-DPSK Format" *Optical Fiber Communications Conference Journal of Lightwave Technology* **22**, 208-214 (2004).
98. de Matos C. J. S., Taylor J. R., Hansen T. P., Hansen K. P. and Broeng J. "All-fiber chirped pulse amplification using highly-dispersive air-core photonic bandgap fiber" *Optics Express* **11** (2003).
99. Lim H. and Wise F. W. "Control of dispersion in a femtosecond ytterbium laser by use of hollow-core photonic bandgap fiber" *Optics Express* **12** (2004).
100. Jasapara J., Her T. H., Bise R., Windeler R. and DiGiovanni D. J. "Group-velocity dispersion measurements in a photonic bandgap fiber" *Journal of the Optical Society of America B (Optical Physics)* **20**, 1611-15 (2003).
101. Ouyang G., Xu Y. and Yariv A. "Theoretical study on dispersion compensation in air-core Bragg fibers" *Optics Express* **10**, 899-908 (2002).
102. Engeness T. D., Ibanescu M., Johnson S. G., Weisberg O., Skorobogatiy M., Jacobs S. and Fink Y. "Dispersion tailoring and compensation by modal interactions in OmniGuide fibers" *Optics Express* **11**, 1175-1196 (2003).
103. Fernando J. L. "Two methods measure chromatic dispersion" *Test & Measurement World* **22**, 21-6 (2002).
104. Treacy E. B. "Optical Pulse Compression With Diffraction Gratings" *IEEE J. Quant. Electron.* **QE-5**, 454-8 (1969).
105. Smith R. L. "The velocities of light" *American Journal of Physics* **38**, 978-83 (1970).

106. Skorobogatiy M., Jacobs S. A., Johnson S. G., Meunier M. and Fink Y. in *Photonic Crystal Materials and Nanostructures, Apr 27-29 2004* 161-172 (International Society for Optical Engineering, Bellingham, WA 98227-0010, United States, Strasbourg, France, 2004).
107. Shu X. and Sugden K. "Transmissive in-fiber Fabry-Perot etalons as tunable dispersion compensators and dispersion-slope compensators" *Optics Letters* **28**, 1897-9 (2003).
108. Takushima Y. and Kikuchi K. "In-service monitor for group-velocity dispersion of optical fibre transmission systems" *Electronics Letters* **37**, 743-745 (2001).
109. Skorobogatiy M., Ibanescu M., Johnson S. G., Weisberg O., Engeness T. D., Soljagic M., Jacobs S. A. and Fink Y. "Analysis of general geometric scaling perturbations in a transmitting waveguide: Fundamental connection between polarization-mode dispersion and group-velocity dispersion" *Journal of the Optical Society of America B: Optical Physics* **19**, 2867-2875 (2002).